Particle Sorting and Automatic Particle Identification for Advanced Medical Diagnostics

PhD Thesis

Juan Carlos Rodriguez Luna

Declaration

I, Juan Carlos Rodriguez Luna, declare that this thesis, which is approximately 48000 words in length is the product of my original research. It has been composed by me and has not been previously submitted for examination which has led to the award of a degree.

Date:

Signature of candidate:

Acknowledgements

Abstract

The physical separation of micro-particles is very important in many research field as diverse as chemistry and medicine. The main goal of the current separation techniques is to extract micro-particles such as cells at a high processing rates and purity. Chromatography, for instance, is commonly applied for the detection and enrichment of pathogens, which is useful for the medical diagnostics of parasitic infections. Many separation techniques have been developed over the years, applying physical phenomena of different kinds and/or taking advantage of unique physical properties of the particles themselves. From all of these techniques, one that has remained popular over the years is Dielectrophoresys(DEP). One of the main reasons for its popularity is that it does not require markers of any kind; it takes advantage of differences in the particle's polarizability, size and shape. Another distinctive characteristic of dielectrophoresis is its selectivity due to its capacity to be controlled using frequency and voltage amplitude and its suitability for small microfluidic systems.

In very general terms the work I have done during my PhD studies was oriented towards the development of novel and robust technology for aiding in the micro-particle sorting and bio-particle recognition by using computer tools. The ideas and concepts I will be introducing throughout this document were allowed total freedom to evolve and change to better fulfill the main goals of the project and also to better adapt to the many technical challenges I had to face during my research. As well as developing a new dielectrophoresis method I have also tried to maximize the impact of this work by doing it in a truly accessible way for anyone, regardless if they are interested in basic research, a possible application or just looking to adapt this concepts and tools for a different purpose.

The central work in this PhD thesis focuses on two main topics:

- Computerized bio-particle tracking and identification using a machine-learning algorithm that incorporates a number of predictors, including colour histogram comparison.

- A portable dielectrophoresis(DEP) electronic device able to tailor the potential across a microfluidic channel for particle separation.

The first project is about computerized vision system designed to track and identify micro-particles of interest through the use of video microscopy, machine learning and

other video processing tools. This system uses a novel particle recognition algorithm to improve specificity and speed during the tracking and identification process. We show the detection and classification of different types of cells in a diluted blood sample using a machine-learning algorithm that makes use of a number of predictors, including shape and color histogram comparison. This software can be considered as a stand alone piece of work. Its open source nature makes it ideal for scientific purposes or as a starting point for a different application. In the context of this PhD thesis, however, it is an invaluable tool for validating and quantifying experimental results obtained from the micro-particle separator experiments presented in Chapter 4.

The central piece of work in this PhD thesis is introduced in Chapter 4. This project is about the development of a all-in-one continuous flow DEP based microparticle separator which uses a system of individually addressable electrodes to shape and control the particle's potential energy profile across the entirety of a microfluidic channel. These *tailored potential landscapes* are created by averaging the electric field generated by 64 individual electrodes, where the electronic device has complete control over each electrode's on/off state, frequency, AC voltage amplitude and pulse duration. All the characteristics of the *potential landscapes* are controlled wirelessly through a mobile phone application. These specially designed *potential landscapes* allow us to make lateral sorting and/or concentration of a binary mixture of particles at the same time they move through a microfluidic channel; all this without the need for buffer flows or additional external forces. One of the outstanding characteristics of this new sorting technique is that it relays exclusively on negative DEP. Most previous techniques require a combination of positive and negative DEP and possibly and external force of different nature to achieve particle sorting; all of which requires the use of a crossover frequency and hence a careful control of the conductivity of the suspending medium. Here by using only negative DEP we eschew the careful control over the conductivity of the suspending medium and the use of any other external force; all this contributes to make our device small and robust. In addition to this, our electronic device was designed to include all the supporting electronics it needs in a small and robust printed circuit board that can also be operated by batteries. We present simulation results to illustrate the physics behind this new technique along with experimental results demonstrating the separation of polystyrene beads.

Contents

List of Figures

Chapter 1

Literature Review

The ability to isolate and enrich a specific type of bio-particle from a heterogeneous biological sample is a very important requirement for biomedical applications such as rare cell detection and identification. As the lab-on-a-chip technology becomes more popular and accessible new designs and techniques are been developed and tested for applications in different areas of biology and medicine. The purpose of this chapter is to introduce some of the most popular and successful microparticle manipulation techniques applied in general purpose analysis platforms. Many of the techniques described in this chapter are well established in the field and have practical applications for the sorting and concentration of biological particles or other materials. The techniques we are about to introduce exploit different physical phenomena or unique properties of the particles themselves. These generated forces over the target microparticles could be very different in nature, ranging from acoustic to magnetic. In this chapter we will only give a brief introduction to the physics and applications of some of the most successful *label-free methods* as these are the most relevant to our work. More specifically, in this review we will focus only on: hydrodynamic manipulation [1–3], acoustic force [4–6], dielectrophoresis(DEP) [7–9], optoelectronic tweezers(OET) [10–12], optoelectrowetting(OEW) [13,14] and Optical Tweezers(OT) [15–17]. Our intent is to highlight their strengths and weaknesses in regard to the separation of biological or non-biological micro particles. We present this with the hope this brief review will give us a better understanding of the role dielectrophoresis plays in the microparticle manipulation field and provide us with a good idea of its advantages and limitations. Moreover we will be paying special attention to dielectrophoresis, which is the technique we used in our own microparticle sorter.

Two of the most reliable technologies for cell detection and separation are: Fluorescence-Activated Cell sorting (FACS) [18,19] and magnetic activated cell sorting (MACS) [20,21]. However, these techniques require the use of tags or labels for achieving particle detection and sorting. FACS uses fluorophore-conjugated antibodies to separate a population of cells in sub-populations based on fluorescent labeling. On the other hand, MACS technique uti-

lizes magnetic beads conjugated with antibodies to label cells of interest. Although both methods have high-throughput the system setup is costly and bulky, the operation relatively complex and requires reagents. Furthermore, these techniques rely on the existence of specific cell-surface antigens and high-affinity probes to these antigens. Moreover, the irreversible attachment of these proves to target cells could influence cell behaviour [22]. There is significant interest in developing techniques that are label free and take advantage of the intrinsic properties of particles of a given population, such as size, shape, density, electrical permitivity, etc. A truly useful technology must be user-friendly and compact; a system that is able to make spatial separation of multi-component mixtures in a clinicians office or at the point of care. In this chapter we are not presenting an exhaustive analysis of all the existing label-free methods for particle sorting, but rather we will try to create some context for the research we have performed in relation to continuous particle concentration and sorting.

1.1 Hydrodynamic manipulation

1.1.1 Device operation

Hydrodynamic manipulation in microfluidics refers to the use of fluid motion to control the movement of particles through *hydrodynamic forces*. These hydrodynamic forces are applied on particles through liquid motion against them or around them. This makes it possible to control the particles' displacements and trajectories.

Before we move on with the actual description of the technique, we will introduce a very important dimensionless number in microfluidics: the Reynolds number **Re**, which is commonly used to identify or differentiate between laminar and non-laminar flows. This number one of the most frequently mentioned dimensionless number in microfluidics; it represents the ratio of the inertial force to the viscous force and is expressed as a function of density ρ, velocity U, characteristic length L, and dynamic viscosity μ in the following way [23]:

$$Re = \frac{\rho_m U L}{\mu} \tag{1.1}$$

The Reynolds is a very useful quantity when it comes to comparing inertial and viscous effects. For example, the very low values for **Re** that are typical in microfluidics reveal that micro-scale flows are greatly dominated by viscous effects. To be more specific, the flow inside microchannels, an **Re** of less than 1000, corresponds to the *laminar regime*, while an **Re** of more than 1000 corresponds to the *turbulent regime* [24]. For a more specific example, take the case of water($\rho \approx 1000$ kg/m^3, $\mu \approx 0.001$ N s/m^2 at room tem-

perature) frowing at 1 μL/min through a microchannel of diameter 100 μm. In this case the Reynolds number is only 0.2, so the microchannel flow is clearly laminar.

Another very important quantity in microfluidics system under laminar flow is the *hydrodynamic drag force*: F_{drag}. This force is the force affecting the particles in virtue of the movement of fluid around them, see Fig.1.3a. This force is given by the Stokes drag force [25]:

$$F_{drag} = 6\pi\mu rV \tag{1.2}$$

where μ is the viscosity of the media, r is the radious of the particle and V is the velocity of the particle that is given by the velocity of the fluid (Fig. 1.3a).

Hydrodynamic manipulation covers a group of standard methods for particle manipulation and separation [1]. Passive technologies for the manipulation of particles are those which do not rely on external forces and depend exclusively on the channel geometry for the generation of hydrodynamic forces on particles. We will start our discussion of hydrodynamic manipulation and separation techniques by mentioning two passive methods of separation that have been receiving a lot of attention in recent years: Deterministic Lateral Displacement(DLD) and Inertial Focusing(IF). Deterministic lateral displacement uses laminar flow through a periodic array of micrometre-scale posts. This array of post divide the flow into several different streams; this happens at low Reynolds numbers hence there is little mixing between streams. If the suspended particle is smaller than the stream, then it will travel within it; however, if the particle is larger than the stream, it will be pushed laterally by the obstacles(posts) [26].

Figure 1.1: Separation of a mixture of fluorescent microspheres with diameters of 0.80(green) and 0.90(red) and 1.03μm (yellow). The fluorescence intensity profile shows three peaks corresponding to the three beads sizes. Source: Richard Huang et al [26].

The control over the size of particles to be sorted/separated is obtained from three variables: diameter of posts, the distance between posts, and the offset of the posts.

In Fig.1.1 we have the results obtained for the sorting of a mixture of fluorescent

polystyrene beads. The diameter of the used beads are 0.80(green), 0.90(red), and 1.03(yellow) μm in diameter. In the figure, we can also see the obtained fluorescence intensity profile, which was scanned 14 mm from the injection point; there are three distributions which correspond to 0.80, 0.90 and 1.03 μm, all centred at the mean of the peaks and with error bars with are attributed to the inhomogeneity of the beads populations. This separation technique does not use external forces and does not depends on diffusion.
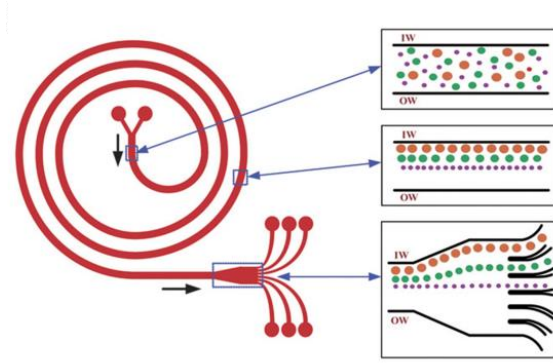
Figure 1.2: Spiral channel for the continuous separation of triplet polystyrene beads: 10, 15 and 20μm in diameter. Source: Kuntaegodanahalli et al [27].

Inertial microfluidics works for Renolds numbers between one and one hundred; a range for which the finite inertia of the fluid generates inertial effects which are the basis of inertial migration [27]. We can describe inertial migration as a phenomenon in which particles that are randomly dispersed at the entrance of a straight microchannel after travelling some distance migrate laterally to cross-sectional equilibrium positions. This inertial migration is considered to be originated by the interaction of two inertial effects: the shear gradient lift force, which directs the particles away from the channel centre and, a wall induced lift force, which repeals the particles away from the wall towards the centreline of the channel [28]. A straight rectangular channel is probably one of the most common geometries due to ease of operation and microfabrication limitations. However, there are some possible variations in structure. In Fig.1.2 we have a spiral channel for the separation of a mixture of particles. In this design, when a fluid flows through the curved channel a secondary flow is created as a result of velocity differences between the fluid in the central and near-wall regions of the channel. Due to the higher velocity of fluid elements near the channel centreline, they will have larger inertia and would flow outward around a curve due to centrifugal effect. As a result, a pressure gradient in the radial direction of the channel will be created. Moreover, due to the centrifugal pressure gradient, the slower fluid near the wall re-circulates inwards, which generates two symmetric circulating vortices [28]. Using a spiral channel, Kuntaegodanahalli et al demonstrated the continuous separation of a mixture of polystyrene beads(10, 15 and 20μm) with an efficiency of 90%, see Fig.1.2. Inertial focusing has proven to be able to offer a well-controlled inter-particle spacing, which is used to make continuous sorting of particles.

Figure 1.3 illustrates a few other common manipulation techniques. In Fig.1.3b we

have an instance of Sheath flow manipulation of particles through the use of two lateral liquid flows sandwiching the fluid containing the particles [2]. Another method for manipulating particles is the Sheathless particle focusing, see Fig. 1.3c. This process uses the hydrodynamic drag force to move the flowing particles towards their equilibrium positions according to the velocity profile of the liquid stream [2].

Another good example of relatively simple channel features that makes use of hidrodynamic forces is the H-shaped channel shown in Fig. 1.3(d), which can be used for separation, extration, or filtering. A fluid with mixed particle contents joins another carrier fluid at the inlet, and while traversing across the common channel the smaller particles diffuse faster into the second fluid [3]. The highly laminar nature of flow in microchannels prevents bulk mixing, so diffusion is the dominant mechanism of interaction between the two fluids as they move in parallel along the common channel. At the exit, the common stream splits, leaving two streams with smaller particles having been extracted from the original fluid.
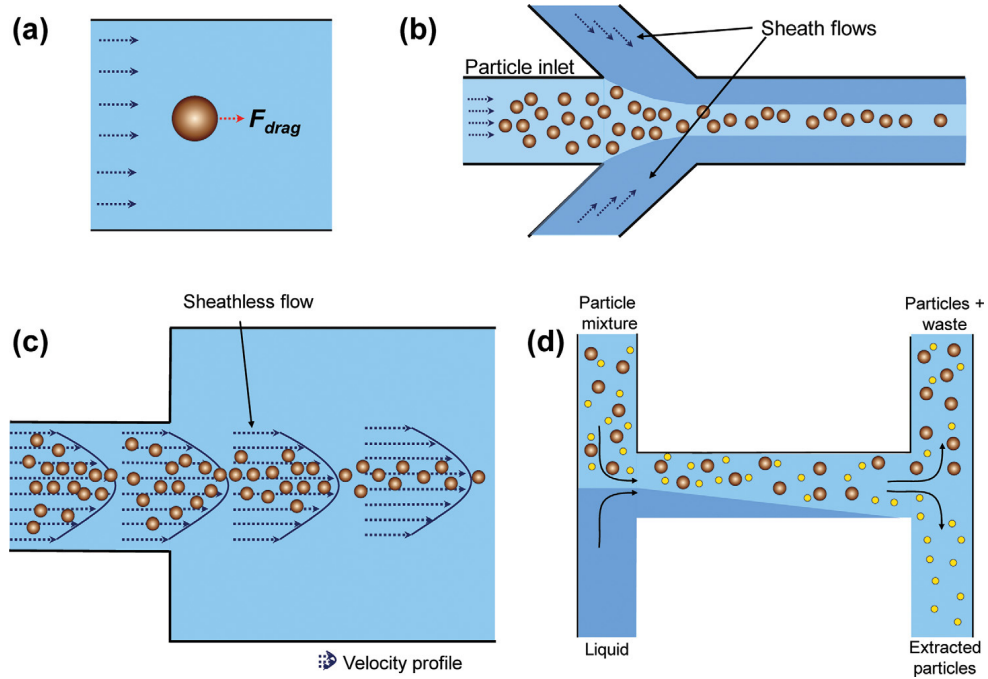
Figure 1.3: Hydrodynamic particle manipulation. (a) Drag force acting on a particle under microfluidic flow; (b) sheath flow focusing; (c) sheathless flow focusing; (d) H-shaped inlet and outlet microfluidic separation system. Source: Aminuddin A. Kayani et al [24].

The previous examples illustrate meaningful functionality from elegantly simple microchannel features. In case it is needed, however, almost limitless freedom can be obtained for channel design based on photolithography.

1.1.2 Advantages and potential drawbacks

Hydrodynamic manipulation	
Advantages	Potential drawbacks
• These methods are label free. • Increased accessibility due to lower micro-fabrication cost [29]. • Able to focus and order particles and cells continuously and without the use of external forces; which reduces complexity and makes it easy to integrate with optical imaging techniques.	• Meticulous design and simulation of microfluidic flow rates are needed because the hydrodynamic forces exerted on the particles is highly dependent of the channel topology. • In most of the applications bulky and complex systems are needed to carefully control the fluid flow rate. • These techniques are not reconfigurable in the sense that it is not possible to reconfigure the device for new conditions without actually having to redesign and replace it.

Table 1.1: Advantages and potential drawbacks of hydrodynamic manipulation techniques.

1.2 Acoustic manipulation

1.2.1 Device operation

In this section we will introduce a label free micro-particle separation technique that utilizes acoustic waves to induce an acoustic force on micro particles, which cause them to move [30]. The acoustic waves are commonly generated by interdigitated electrodes on a substrate or a ultrasonic transducer [4]. When we apply standing wave acoustic force on a suspended particle it will experience an acoustic force given by [5]:

$$F_r = -\left(\frac{\pi P_o^2 V_p \beta}{2\lambda}\right) \cdot \phi(\beta, \rho) \cdot \sin\left(\frac{2\pi x}{\lambda}\right) \tag{1.3}$$

$$\phi(\beta, \rho) = \frac{5\rho_p - 2\rho_m}{2\rho_p + \rho_m} - \frac{\beta_p}{\beta_m} \tag{1.4}$$

where P_o is the pressure amplitude of the acoustic wave, V_p is the particle volume, β and ρ are the particle or liquid compressibilities and densities, respectively, λ is the wavelength of the acoustic wave, ϕ is the so called acoustic contrast factor, and x is the distance to the nearest pressure node. Subscripts p and m denote particle and suspending medium, respectively.

The generated acoustic force particles experience is dependent of the amplitude and frequency of the applied acoustic waves, the elasticity and size of the particle itself as well as the liquid the particle is suspended in.

When a particle is exposed to a acoustic standing wave there is two possible outcomes: the particle being pushed towards the pressure node or towards the pressure anti-nodes, see Fig.1.4. The pressure node is the location where the pressure is constant and does not change. On the other hand, the location where the acoustic waves form a maximum or minimum is the pressure anti-node, [24]. The ϕ-factor afects directly the direction of particle motion (Eq.1.3). If $\phi > 0$, the particle will migrate toward the pressure nodes and if $\phi < 0$, the particle will migrate toward the pressure anti-nodes, see Fig.1.4.

In Fig.1.5 we have an example of the use of surface acoustic waves(SAW) for particle concentration. Haiyan Li et al [6] used non-symmetric SAW to generate acoustic streaming on a droplet containing the target particles. The acoustic streaming induced in the droplet by the asymmetric surface acoustic waves lift the particles from the substrate to follow the flow circulation. Shear-induced migration gives rise to an inward radial force which concentrates the particles at the center of the droplet, see Fig.1.5. The devices uses a LiNbO$_3$ as a substrate and a set of 25 interdigitated transducer(IDT) electrodes with 12 mm aperture and a wavelength of λ=440μm. The applied AC signal was a sinusoidal wave
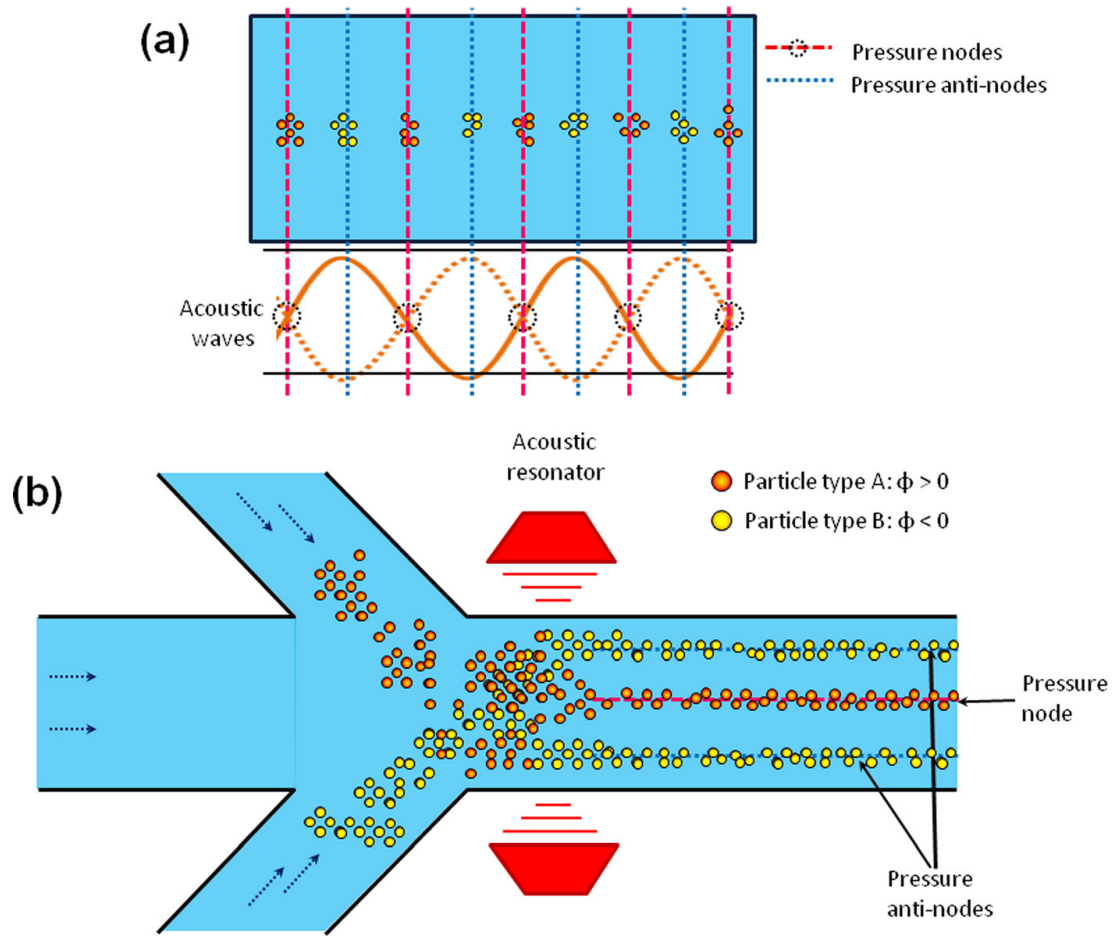
Figure 1.4: Acoustophoretic manipulation of suspended particles.(a) Acoustophoretic manipulation of particles when subject to acoustic waves. (b)Scheme of acoustophoretic sorting of a mixture of paritlcles with different density and compressibility properties. Source: Aminuddin A. Kayani et al [24].

at a resonance frequency f_0 of 8.611MHz. Polystyrene beads and yeast cells were used to test the device [6]. In Fig.1.5 we have some results for particle concentration.
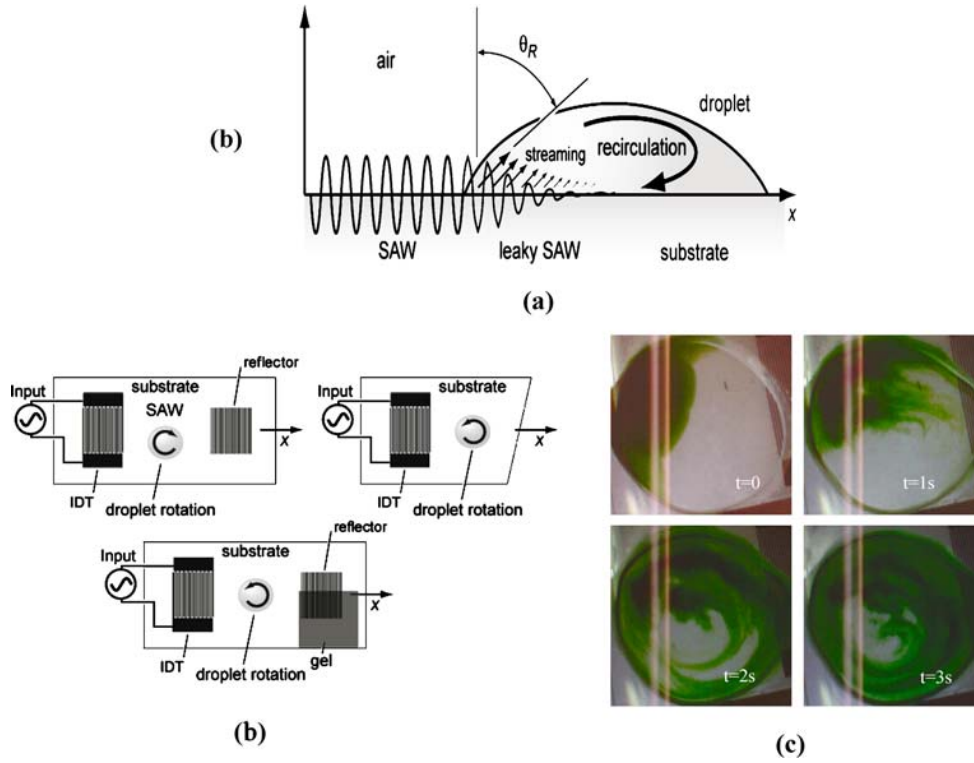
Figure 1.5: Acoustic streaming in a small fluid volume. a) Diagram of the acoustic streaming acting on a droplet containing the target particles. b) Diagram of different IDT arrangements used to generate asymmetric propagating SAW. c) Sequence of images showing the fluid recirculation generated by asymmetric surface acoustic waves. Source: Haiyan Li et al [6].

1.2.2   Advantages and potential drawbacks

Acoustic manipulation	
Advantages	Potential drawbacks
- This method is label free. - Relatively high throughput. Especially when compared with the most usual implementations of dielectrophoresis and optoelectronic tweezers, to mention two examples. - There is no need to control the conductivity of the suspending medium. This is a big advantage over other techniques e.g. dielectrophoresis(DEP). - This technique provides the ability to separate particles of similar sizes and densities. If one particle is more compressible than the liquid, while another is less compressible, the acoustic force displacing the two particles will be in the opposite direction, causing them to separate [24].	- Particle separation can only be conducted by virtue of their size, density, and compressibility differences [24]. Moreover, most bio-particles have similar density and compressibilities. - It can be difficult to control small nano scale particles using acoustic manipulation [24]. - Acording to Aminudding [24], it can be difficult to integrate acoustic transducers into microfluidic devices. - Force is relatively small on cells due to low acoustic contrast factor between water and cells compared to harder particles such as polystyrene beads.

Table 1.2: Advantages and potential drawbacks of acoustic manipulation.

1.3 Dielectrophoresis (DEP)

1.3.1 Device operation

Dielectrophoresis (DEP) is a label free micro-particle manipulation and separation technique that relies on an electric field induced force applied to a neutral particle in a non-uniform electric field. When subjected to an electric field, a neutral particle is polarized and charged dipoles are established within the particle [7]. The charged dipoles induce unequal electrical forces at the opposing ends of the particles and the net resulting force causes the particle to move. The magnitude of charge and orientation of the induced dipoles is dependent on the intensity and frequency of the electric field and the dielectric properties of the particle and suspending medium, respectively.
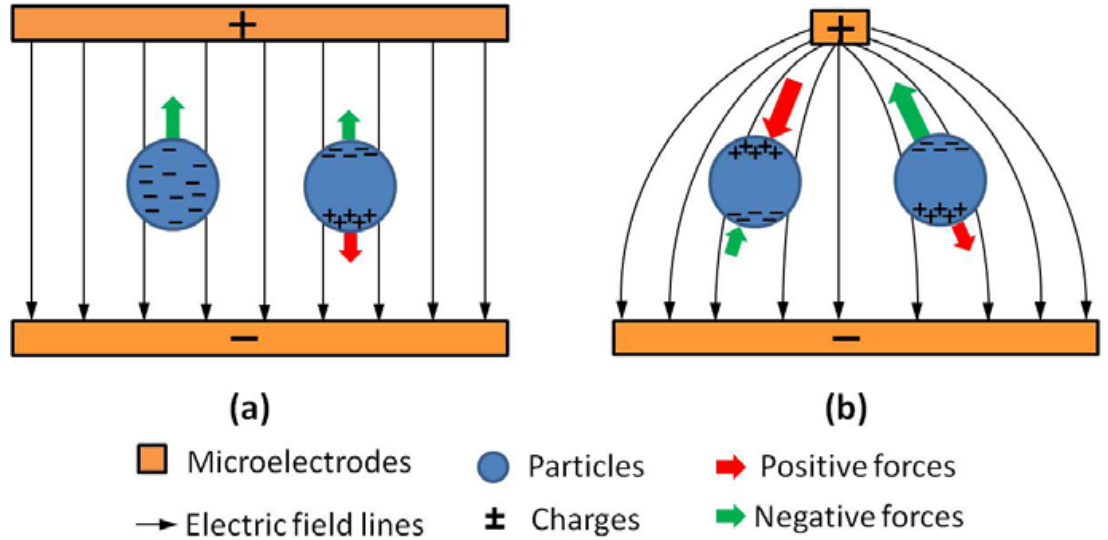
Figure 1.6: Dielectrophoresis(DEP): principle of operation. a) A charged and neutral particle in a uniform electric field. b) A neutral particle in a non-uniform electric field. Please note that although the chargers here are drawn within the particle the resulting dipole is really a result of charges within the particle and within the medium. Source: Ming Li et al [8].

The time averaged dielectrophoretic force on a spherical particle in a AC-field can be expresed as [31]

$$F_{DEP}(t) = 2\pi\epsilon_m r^3 Re[f_{CM}]\nabla E^2 \tag{1.5}$$

where E is the electrical field, ϵ_m is the absolute permitivity of the suspending medium and r is the particle radius. f_{CM} is known as the Clausius-Mossotti (CM) factor, which is given by

$$f_{CM} = \frac{\bar{\epsilon}_p - \bar{\epsilon}_m}{\bar{\epsilon}_p + 2\bar{\epsilon}_m} \qquad (1.6)$$

where $\bar{\epsilon}$ is the complex permitivity, defined as

$$\bar{\epsilon} = \epsilon - j\frac{\sigma}{\omega} \qquad (1.7)$$

and subscripts p and m stand for the particle and the medium, respectively.

From Eq.1.5 we can see that DEP force have the following characteristics [32]:

1. DEP force is only generated when the electric field is non uniform, otherwise $\nabla E = 0$ and the force given by Eq.1.5 becomes zero.

2. The generated DEP force depends not only on the electrical properties of the particle and the medium but also on the frequency of the applied field. The dependence on the electrical properties is through the permitivity and conductivity of the particle and medium, see Eq.1.7.

3. DEP force depends on the sign and the magnitude of the CM factor: f_{CM}. If $f_{CM} > 0$, then the particles will be attracted by the electric field strength maximum and repelled from the minimum; this is called positive dielectrophoresis (p-DEP). If $f_{CM} < 0$, then the particle will be attracted by the electric field strength minimum and repelled from the maximum; this situation is called negative dielectrophoresis (n-DEP).

4. DEP force is proportional to particle volume, see Eq.1.5. Which makes DEP capable of differentiating particles by size.

5. The strength of the generated DEP force has a dependence to the magnitude of the applied electric field; which makes it non-linear phenomena due to dependence on E^2

By combining Eqs.1.6 and 1.7, the Clasious-Mossotti factor f_{CM} can be expressed as

$$f_{CM}(\epsilon_p, \sigma_p, \epsilon_m, \sigma_m, \omega) = \frac{(\epsilon_p - \epsilon_m) + \frac{j}{\omega}(\sigma_p - \sigma_m)}{(\epsilon_p + 2\epsilon_m) + \frac{j}{\omega}(\sigma_p + 2\sigma_m)} \qquad (1.8)$$

By examining Eq.1.8, it can be deduced that the sign of the CM factor is determined by the electrical conductivities of the particles and the medium at low frequencies; however, it is determined by the permitivities at higher frequencies. Between those two limits there exist a transition region. The point where n-DEP response switches to the p-DEP (or p-DEP response switches to n-DEP) is called *cross-over frequency*. It is the point where the complex permitivity of the particle is exactly equal to that of the medium. At that
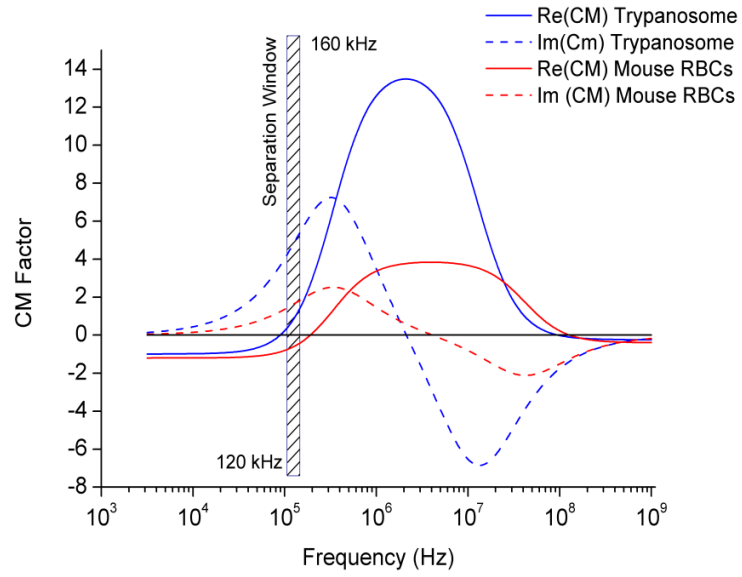
Figure 1.7: Simulation of Clausius-Mossotti factor(CM) for RBCs and trypanosome cells suspended in a medium with 30mS/m conductivity. Source: Clemens Kremer et al [33].

frequency, DEP will be zero ($\text{Re}[f_{CM}]=0$), during this condition particle and buffer are equally polarized so pole in liquid equal in charge to pole in particle.

In Fig.1.7 we have a simulation of the Clausius-Mossotti factor for mouse RBC and trypanosome cells [33]. Most of the sorter devices which apply dielectrophoresis use the cross-over frequency, see Fig.1.9, or some specially selected frequency(or range of frequencies) for which there is a negative and positive DEP, see Fig.1.7, in a way that makes possible to attract one specific type of particle and repel another.

In this technique the non-uniform electric field is applied by using specially designed external electrodes that are submerged into the reservoir. The internal electrodes are usually planar (2-D) electrodes (the height of the electrodes are in the order of hundred nanometers), and are fabricated within the device by means of relatively expensive manufacturing techniques such as e-beam evaporation, which results in less economically feasible systems [9, 32].

Dielectrophoretic separation of bio-particles from heterogeneous biological samples is possible because the DEP force can differentiate across different types of cells due to variations in features such as cell radius, electrical properties and cell shape. In the Fig.1.8 an example of a dielectrophoretic microfluidic chip that incorporates filtering, focusing, trapping, and detecting in a single device. [9].
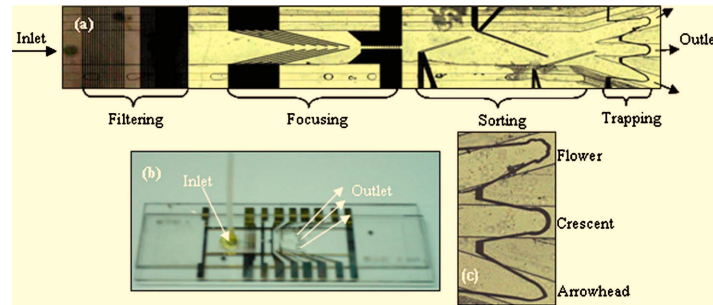
Figure 1.8: Example of a microfluidic chip that make use of DEP. The DEP chip has four stages: filtering, focusing, sorting, and trapping. The device was utilized to separate a mixture of bacteria and latex particles into the three diferent electrode-trapping regions located near the device outlet. Source: I-Fang Cheng et al [9].
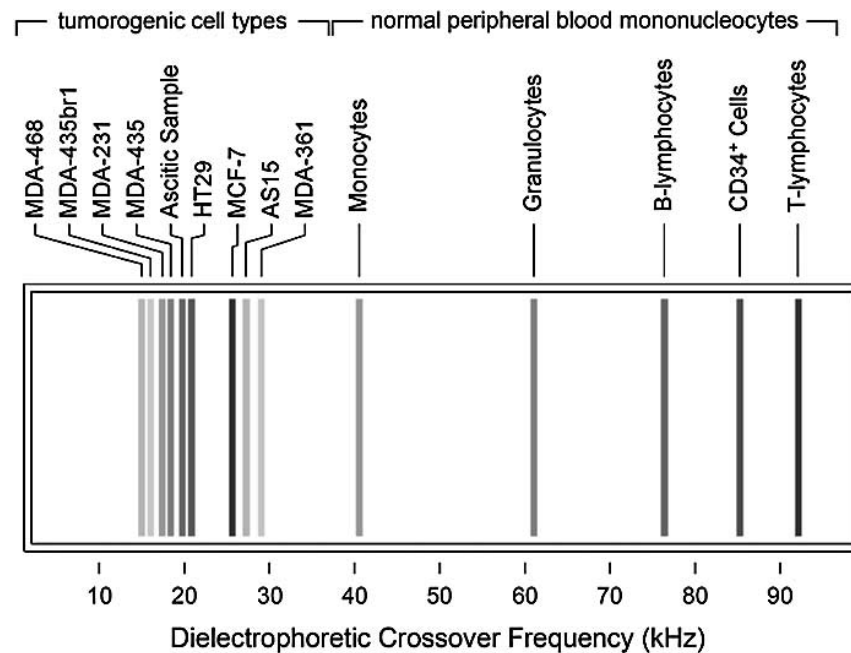
Figure 1.9: Crossover data for normal peripheral blood mononuclear cells and nine human tumor cells types. Source: Peter Gascoyne et al [34].

1.3.2   Advantages and potential drawbacks

Dielectrophoresis (DEP)	
Advantages	**Potential drawbacks**
- This method is label free. - It does not require complex instrumentation. The low operating voltage simplifies the equipment needed to generate the electric fields, prevents Joule heating and makes the system compatible with integrated circuits and suitable for battery powered hand-held devices. - DEP is able to induce both negative and positive forces.	- High manufacturing cost. Integration of on-chip circuits increases the cost of the device, which make it less attractive for disposable applications. This point is particularly relevant for biomedical diagnostic applications. - According to Peter Gascoyne et al [34] it becomes impractical to separate cell having less than 50% difference in their crossover frequencies by applying an AC electric field to trap one particle type by positive DEP while simultaneously repelling other types by negative DEP, see Fig.1.9. This point will become particularly relevant later on when we introduce our micro-particle separator in Chapter 4. - In oder to apply n-DEP and p-DEP simultaneously, it is necessary to carefully control the conductivity of the suspending medium.

Table 1.3: Advantages and potential drawbacks of dielectrophoresis.

1.4 Opto-electronic tweezers (OET)

1.4.1 Device operation

Optolectronic tweezer (OET) is a relatively new concept for the micro-manipulation of particles which was first introduced in 2005 by Pei Yu Chiou et al [10]. This technique uses both light and electrical bias to create a non-uniform electric field, which in turn exerts a force on dielectric particles [35].
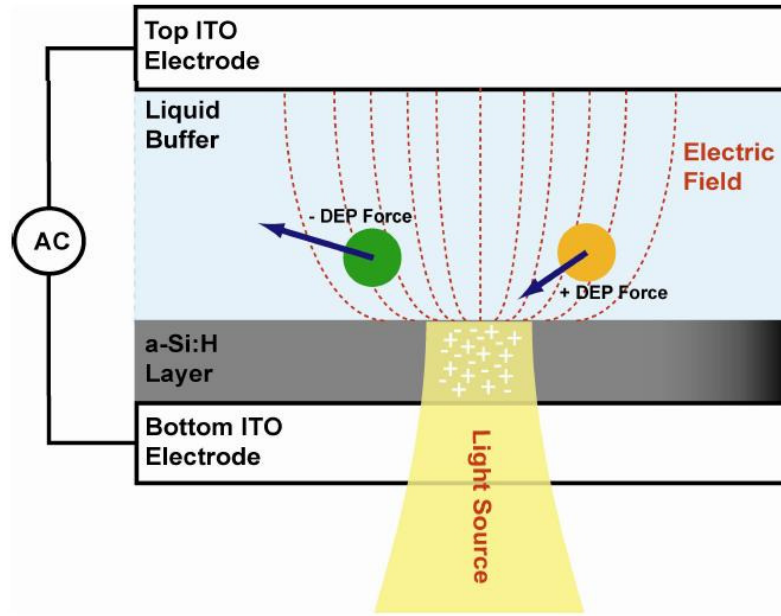
Figure 1.10: Optoelectronic tweezers (OET) device structure. The OET device consists of a top transparent ITO electrode and a bottom ITO electrode. There is a layer of photoconductive material (hydrogenated amorphous silicon) on top of the bottom electrode. An AC voltage is applied between the two electrodes. Source: [11].

The technique makes use of light to excite a photo-conductive layer and creates an electric field gradient in the sample. In the Fig.1.10 we have a diagram of the typical structure of the optoelectronic tweezers device (OET). The OET consists of a top transparent indium tin oxide (ITO) layer and a bottom ITO-coated glass substrate on top of which there is a 1 μm thick layer of photo-conductive material (hydrogenated amorphous silicon, a-Si:H) [11].
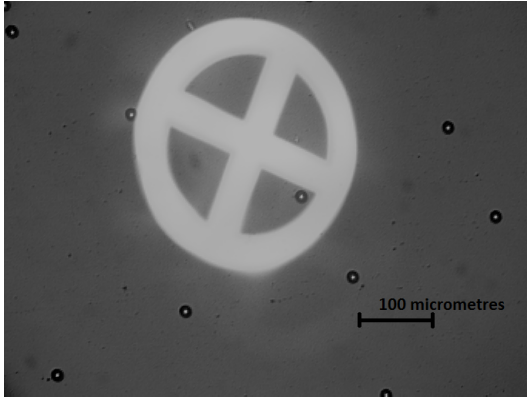
Figure 1.11: Programmable virtual electrode used to measure the maximum forces the technique can exert on polystyrene beads. Individual 15μm-diameter particles are forced to move in a uniformly accelerated circular motion. When the particle is unable to keep accelerating the program automatically calculates the maximum reached lineal velocity and saves all the relevant information.

The sample is contained in between a conductive layer and the photo-conductive one in the bottom substrate. This technique is essentially dielectrophoresis (DEP), but this time instead of metal electrodes *virtual electrodes* are generated using light patterns projected onto the a:Si photo-conductive layer. The amorphous silicon is deposited using plasma enhanced chemical vapor deposition, no photolithography or etching is needed; which represents an advantage over standard DEP techniques.

The time averaged OET force on a spherical particle in an AC-field remain the same as for DEP force [31]:

$$F_{DEP}(t) = 2\pi\varepsilon_m r^3 Re[f_{CM}]\nabla E^2 \qquad (1.9)$$

where E is the electrical field, ϵ_m is the absolute permitivity of the suspending medium and r is the particle's radius. f_{CM} is known as the Clasious-Mossotti (CM) factor, which is given by

$$f_{CM} = \frac{\bar{\epsilon}_p - \bar{\epsilon}_m}{\bar{\epsilon}_p + 2\bar{\epsilon}_m} \qquad (1.10)$$

where $\bar{\epsilon}$ is the complex permitivity, defined as

$$\bar{\epsilon} = \epsilon - j\frac{\sigma}{\omega} \qquad (1.11)$$

and subscripts p and m stand for the particle and the medium, respectively.

The generated DEP forces on neutral particles are the result of the interaction of the induced dipoles with the non-uniform electric fields generated by the projected patterns on photo-conductive substrate. Just like standard DEP, the force on particles depends on the electric field gradient and the electric properties of the particle and the suspending medium.

In Fig.1.11 we have an instance of a generated virtual electrode. It was designed for a careful measurement of the maximum velocities that can be achieved for the movement of 15μ-diameter polystyrene particles. We have a wheel-shaped pattern that was programmed with a uniformly accelerated angular rotation with respect to its central axis. Individual polystyrene particles are forced in a circular motion that keeps gradually accelerating until

Figure 1.12: a) Portable OET system. b) Optical manipulation of 20μm-diameter polystyrene beads. Source: Steven Neale et al [12].

DEP force is unable to overcome the Stokes drag force which has a lineal dependence with the relative velocity of the suspending medium, see Eq.1.2. In Fig.1.12 we have an portable version of the OET system developed by Steven L. Neale et al [12]. It was built from a small microscope with a 20X objective that uses bright field illumination from an LED array. For the generation of the light patterns it uses a mini data projector(Dell M110) which is controlled with a laptop. This example illustrates the manipulation of several 20μm-diameter polystyrene beads.

1.4.2 Advantages and potential drawbacks

Opto-electronic tweezers (OET)	
Advantages	Potential drawbacks
- This method is label free. - It is possible to achieve a high degree of control over the manipulation of microscopic and nanoscopic objects. - Another big advantage is that it confers total freedom over the trajectories one can implement in 2D. - The required photo-conductive layers are not patterned, which makes the fabrication process very straightforward and simple. - The potential for mass fabrication is high.	- Acording with Martinez-Duarte [36], the throughput of the device may not be high since the virtual electrodes generated using this technique are still surface effect. In most cases, all the planar electrodes are fabricated at the bottom substrate and thus an electric field gradient is only effectively established in sample volumes less than 30 micrometres high. - When working with bioparticles it would be necessary to work in culture media or physiological buffers that intrinsically exhibit high electrical conductivity; however, this technique can only operate in relatively low conductivity media. - An illumination system powerful enough to create the virtual electrodes is bulky and expensive. - This technique inherits one of the main problems dielectrophoresis has: in order to take advantage of the crossover frequency and/or n-DEP and p-DEP, it is necessary to fine tune the conductivity of the suspending medium.

Table 1.4: Advantages and potential drawbacks of opto-electronic tweezers.

1.5 Optoelectrowetting(OEW)

1.5.1 Device operation

One of the most important functions of a microfluidic device is to move a volume of fluid from one location to another. In this regard, optoelectrowetting is a very interesting option to achieve flow control. The use of optoelectrowetting based microfluidic devices has attracted a lot of attention recently due to the fact that it eliminates the need of pumps and valves for the manipulation of fluids.
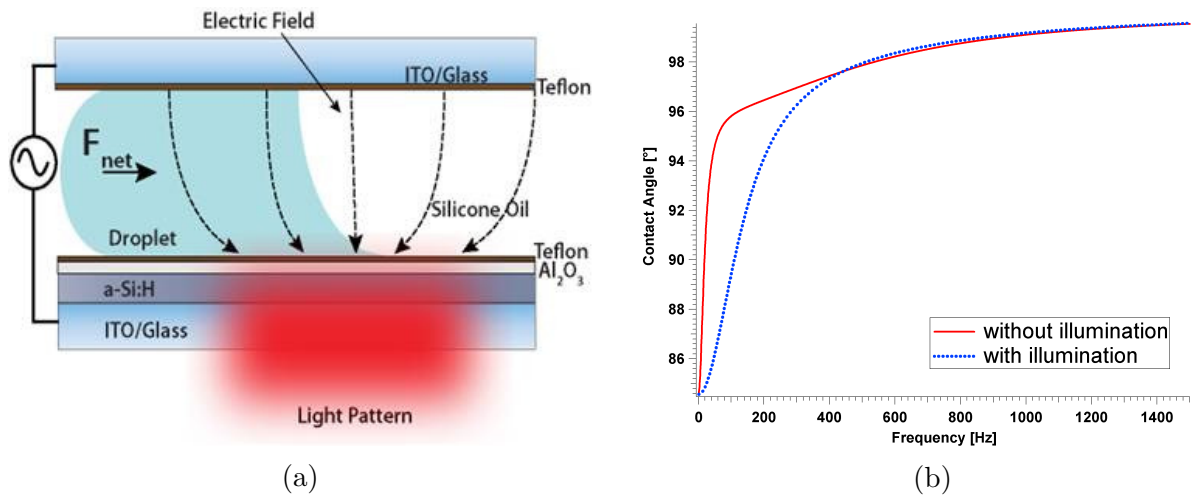
Figure 1.13: **a**) Diagram of a light actuated microfluidic device that optically manipulates nano to micro-liter scale aqueous droplets on the device surface. Source: A. Jamshidi et al [11]. **b**) Simulation results for the contact angle as a function of frequency for illuminated and non-illuminated photoconductive layers. Source : F. Krogmann et al [14].

In diagram of Fig.1.13a we can see a schematic of a optoelectrowetting based device similar to that developed by Justin K. Valley et al. [13]. It is a unified platform for that allow the manipulation of aqueous droplets with electrowetting and individual particles(within those droplets) with dielectrophoresis, all in the same device.

For the fabrication of the bottom substrate they used ITO (300nm) coated glass, a 1μm thick photoconductive a-Si:H layer, a 100nm film of Al_2O_3 and a 25nm film of spin coated 0.2% Teflon (300rpm, 30s). The top substrate is formed from another Teflon-coated ITO glass wafer. The two substrates are then placed on top of one another separated by a spacer layer of double-sided tape (100μm) forming the microfluidic manipulation chamber [13].
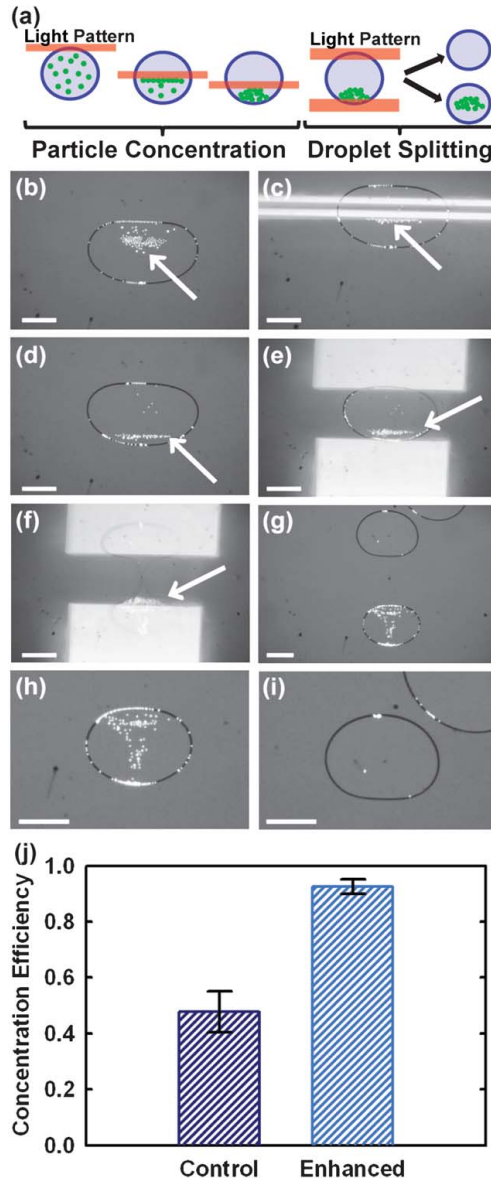
Figure 1.14: Particle concentration, in a 335nL droplet, of fluorescent beads using optoelectrowetting and optoelectronic tweezers in a unified platform. Source: Justin K. Valley et al [13].

The droplet containing the particles to be concentrated is sandwiched between the top and the bottom surfaces. By applying light to an specific region of the bottom substrate and a voltage between the electrodes, an additional energy is introduced into the system, which yields to a reduction of the contact angle of the liquid. This effect can be described by the Lippman-equation [14] as follows:

$$\cos(\theta) = \cos(\theta_0) + \frac{\epsilon\epsilon_0}{2\gamma_{LG}d}V^2 \qquad (1.12)$$

where V is the voltage applied, d the thickness of the dielectric layer(Al_2O_3), θ_0 the initial contact angle, ϵ the dielectric constant of the dielectric layer and γ_{LG} the inter-facial tension between liquid and oil.

The Fig.1.13bb shows the simulation results for the contact angle as a function of the frequency of the applied voltage for an examples system, consisting of an amorphous silicon layer, a silicon dioxide layer and a water droplet [14].

In Fig.1.14 we have an illustration of some of the results obtained by Justin K. Valley et al [13] for the concentration of fluorescent polystyrene beads inside a 355nL droplet with conductivity of 10mS/m. First they used OET for concentrating the particles towards one end of the droplet, Fig.1.14c. In the next step the droplet is split in two using OEW, one containing the particles and the other remaining mostly empty, Fig.1.14e-f.

1.5.2 Advantages and potential drawbacks

Optoelectrowetting(OEW)	
Advantages	Potential drawbacks
• The device is relatively easy to fabricate because no lithography is required. • Able to optically manipulate aqueous droplets in real time. • Reconfigurable, the device can easily be reconfigured to make chemical reactions with droplets, for example. • It's possible to scale up the system by increasing the active OEW area.	• According to Justin K. Valley et al. [13] the voltage needed to operate the device is about 40 Vpp. This voltage level would require bulky and expensive electronic, which will make it less suitable for a portable device. • The capacity to manipulate droplets alone does not seems to be very useful for manipulation of individual microparticles. • This technique inherits all the disadvantages of the dielectrophoresis technique.

Table 1.5: Advantages and potential drawbacks of Optoelectrowetting(OEW).

1.6 Optical Tweezers

1.6.1 Device operation

Optical tweezers is a very well established technique for the trapping and manipulation of micro-particles in three dimensions. It applies highly focused laser beams to generate an attractive/repulsive force on particles depending on their refractive index. This phenomenon was firs reported by Artur Ashkin [15] in 1970. A proper explanation of optical trapping must take into account the size of the trapped particles. However, when the diameter of the particle much bigger than the light's wavelength ray optics can be used to give a simple description of the phenomenon, see Fig.1.15.
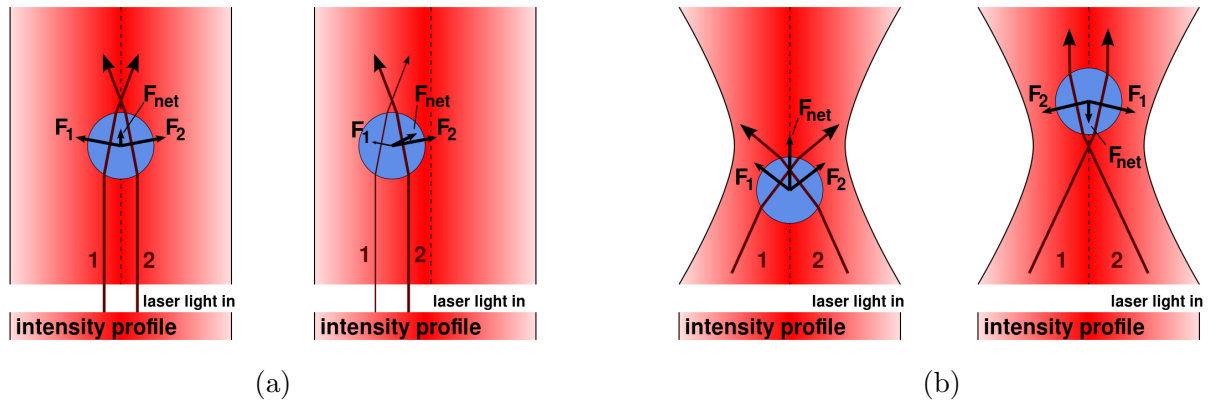
Figure 1.15: **a**) Unfocused laser representation: the net force tends to restore towards the center of the laser. **b**) Focused laser: a focused laser keeps the particle in a fixed axial position. Source : Roland Koebler, CC BY 3.0, https://commons.wikimedia.org/w/index.php?curid=15083883.

Given the light has momentum associated with it, a light intensity profile with stronger intensity towards the center of the laser(TEM_{00} mode Gaussian beam) will generate a net force tending to restore the particle toward the center of the laser, see Fig.1.15a. Moreover, a focused laser will keep the particle in a fixed axial position, see Fig.1.15b [37]. A much more complete technical discussion of the different aspects of the technique and its implementation can be found elsewhere [38].

A typical implementation of Optical Tweezers uses one or two traps. However, there are some designs that implement more than two traps by time sharing a single laser beam between different traps [16] or by using diffractive optical elements to split the beam into many continuously illuminated traps. As an example of the later we have the work done by M. P. MacDonald et al [17]. They used a single laser beam to generate an three-dimensional *optical landscape*, which is used to sort a mixture of particles(in microfluidic flow) based on their sensitivity to the optical potential, see Fig.1.16. The particles used for
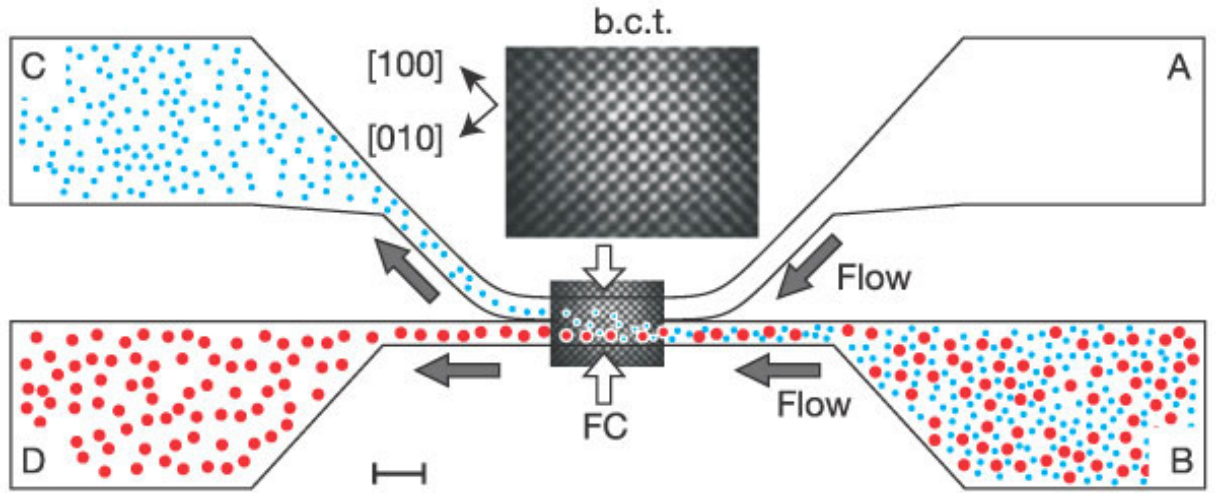
Figure 1.16: An optical lattice is used to sort a mixture of 2μm-diameter silica and polystyrene beads and a mixture of 2 and 4μm-diameter protein micro-capsules. Source: M. P. MacDonald et al [17].

testing the system were a mixture of 2 and 4μm-diameter protein micro-capsules moving at 20μm/s, see Fig.1.17.

The light patterns and the interlinks between the lattice sites were tailored to deflect particles into the desired trajectories. The sorting mechanism takes advantage of the drag force particles experience when particles flow through the optical lattice. By a careful design of the optical lattice it is possible to create an optical path where the optical force dominates and define the particle's trajectory, see Fig.1.17. However, this requires a fine tuning between the drag force and the optical force.
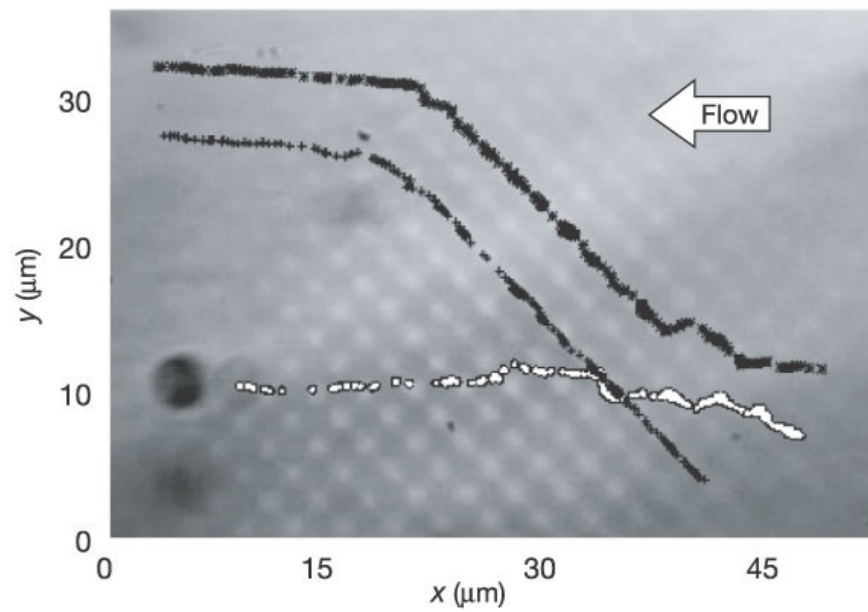
Figure 1.17: Frame by frame tracking of 2 and 4μm-diameter protein microcapsules, represented by the black and white crosses respectively. The flow speed was 20μm/s and a laser power of 530 mW. Source: M. P. MacDonald et al [17].

1.6.2 Advantages and potential drawbacks

Optical Tweezers	
Advantages	**Potential drawbacks**
• This method is label free. • High degree of flexibility on the generation of specially engineered optical landscapes. • There is no need to control the conductivity of the suspending medium. • It's possible to scale up the system by increasing the effective region. This can be done either by sharing a single laser beam between several optical tweezers or by splitting a single laser into multiple traps using a diffractive system as we just saw on previous example.	• The technique requires a careful tuning between the drag force and the optical force. • Even the most basic optical tweezer setup requires expensive, complex and delicate optical equipment which makes it unsuitable for a portable application. • The high intensity of the focused laser light, which generates the traps, typically 10^9 - 10^{12} Wcm^{-1} results in local heating [39].

Table 1.6: Advantages and potential drawbacks of optical tweezers.

Chapter 2

Selected DEP applications

In this chapter we will focus on microparticle sorting technologies that apply dielectrophoresis alone or in a combination with other forces. However, we will only give a brief introduction to some of the micro-particle separation techniques the author considers to be the most representative of the latest trends in DEP particle sorting, or the most relevant and/or similar to our own design. We will be considering continuous and discontinuous techniques. We have selected a small group of DEP techniques that is relevant to the work we have done. We will be discussing: Stepping Electric Fields, Pulsed Dielectrophoresis, Dielectrophoresis Field Flow Fractionation(DEP-FFF), Magnetophoresis-Dielectrophoresis Field Flow Fractionation(MAP-DEP-FFF), Multiple Frequency Dielectrophoresis and Traveling Wave Dielectrophoresis. A few of these techniques apply DEP exclusively, others use it on a combination with external forces, and some even apply DEP forces discontinuously in time. One of these designs was developed having in mind a portable device, but most require sophisticated and bulky equipment; however, we believe they all are a representative sample of current state of the art DEP techniques.

In this brief review we will try to highlight their main features, their strengths, weaknesses and novelty of these different approaches to particle sorting. Later on, in Chapter 4, when we introduce our own DEP technique for particle sorting, this review will help us to better understand and identify the fundamental differences between our technique and previous works, its strengths, limitations and the place it has in the microparticle sorting field as a whole.

2.1 Stepping Electric Fields
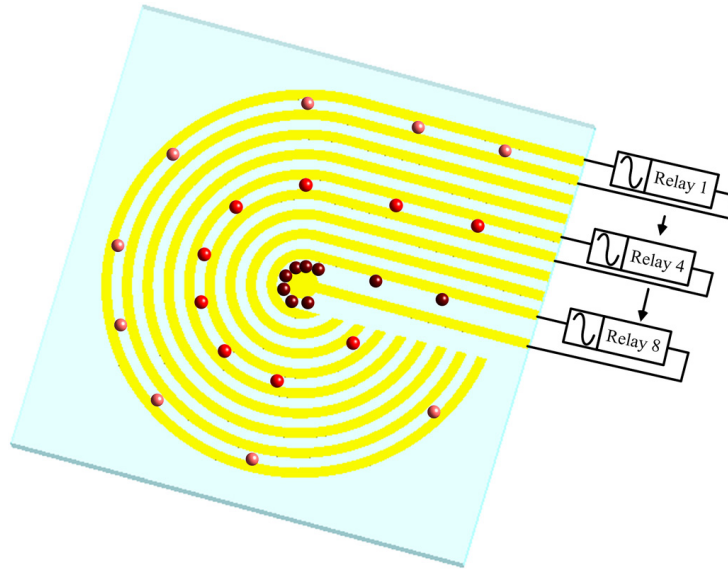
Figure 2.1: Stepping fields: An array of relays is used to switch adjacent pairs of electrodes in a total of 16 switching steps. The 8 relays are sequentially switched on/off using a microcontroller. Source: Chun-Ping Jen et al [40].

The first of the particle sorting techniques we will discuss in this chapter is one that has some similarities to our own technique. Maybe the most important one is the ability to independently control a group of individual electrodes. Also, just like in our case, this technique was implemented on a portable device; however, there is also some very important differences we will discuss in the next sections.

As mentioned previously, *stepping electric fields* is a technique with the capacity to control several electrodes independently. In this sense this technique is different to most DEP techniques. The majority of current DEP designs make us of different variations of two metal electrodes in a single or interdigitated configuration. Devices of this kind have been used to trap bacterial cells in continuous flow [41] and take advantage of differences in the electrical properties of the particles and medium; where the direction of the applied DEP force is a function of the frequency of the applied signal.

Even though this devices can achieve a remarkable performance when utilized properly for specific applications, they are *rigid* and *non reconfigurable*. Reconfigurability is a desired characteristic, specially in research and development where there is a need to experiment with new conditions in a fast and easy way. When we have access to several electrodes we also have the capacity to generate *traveling electric fields* and experiment with a broader group of variables, for example: voltage, frequency, and electrode activation time to affect the sorting speed.

Another advantage of this approach is that it can increase the throughput of the device by using an array of electrodes covering a bigger area in which the generated electric gradients are effective. We could argue that there is a price to pay because an electronic system is needed in order to achieve individual control of each one of the electrodes in an array. However, the advances in electronics, computing and micro-fabrication have made possible the rapid prototyping of very sophisticated systems able to integrate electronics, hardware and software in small and reliable components that now have become standard and are easily available.

Figure 2.2: The system of planar electrodes was etched on ITO glass. The electronic module includes all the required electronic components for the operation of the device. Source: Guang-Hong Chen et al [42].

One excellent example of the application of stepping electric fields is the work done by Guang-Hong Chen et al [42] and Chun-Ping Jen et al [40]. They adapted this technique into a small portable device that uses circular micro-electrodes to isolate and concentrate rare cells. The array of circular metal electrodes is planar and fabricated through a standard photo-lithography process. To generate the *stepping electric fields* they used an array of relays to switch adjacent pairs of electrodes sequentially, see Fig.2.1. The relays are controlled by an 8-bit on-board microcontroller and the AC signal used to power the electrodes is generated through an on-board dedicated IC function generator. Cells are displaced using positive DEP along the direction of the stepping electric fields.

The microfluidic device was designed as an open-top chamber for the concentration of cells. The array of 16 planar electrodes was fabricated by etching a indium tin oxide(ITO) glass substrate using HCl solution. Also a 3μm tick film of hexane-diluted PDMS was spin-coated onto the substrate to prevent electrolysis and cell adherence to the electrodes. The chamber itself was fabricated using PDMS and bonded to the ITO substrate using oxygen plasma treatment(50s). The chamber has a capacity of about 160μL.

The electronic module was designed as all-in-one aparatus. It uses a voltage-frequency converter(MAX 038) and a operational amplifier(AD817) to generate the sinusoidal wave needed for the dielectrophoretic manipulation of cells in the chamber. The system of 8 dual relays(DG201CJ) was controlled using an 8-bit microcontroller(Atmel AT89C51). This is how they achieved stepping electric fields with 16 switching steps. All these

electronic components, including the microfluidic chip, were mounted on a printed circuit board(PCB), see Fig.2.2. The concentration of cells was observed and recorded using an inverted fluorescence microscope.
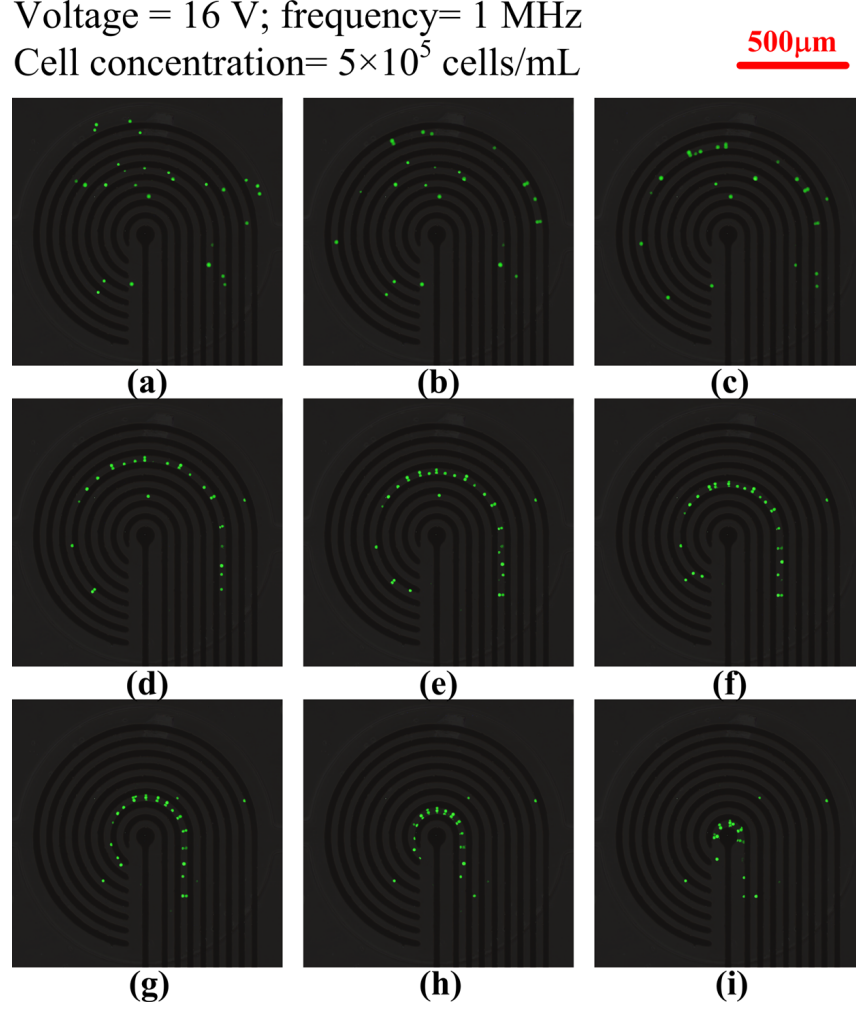
Figure 2.3: Stepping fields: HeLa cell concentration towards the center of the spirals array. The time interval of relay switching was 20s and the total duration of the sequence (a) to (i) was approximately 160s. Source: Guang-Hong Chen et al [42].

Figure 2.3 shows some results concerning the concentration of HeLa cells in a sample with density of $5X10^5$ cells/ml. Each individual electrode is powered with a sinusoidal signal of 16Vpp and a frequency of 1.0MHz. The activation sequence is started from the outermost pair of electrodes towards the center of the chamber. Each pair of electrodes was held on for 20 seconds before switching to the next pair. As we can see in Fig.2.3 HeLa cells are guided towards the center of the chamber following the activation sequence. The time required to concentrate the cells from the outermost electrode to the center is about 160s.

2.1.1 Conclusions

This technique resembles the Spiral Electrode technique, which we will discuss in section 2.5 but they are actually fundamentally different. Here an array of individual electrodes is sequentially activated with positive DEP in order to concentrate the target particles towards the center of the circular array. This technique has some of the most desirable characteristics we would look for on a truly portable device for cell sorting and concentration. First of all, it is truly portable and self contained. It contain the microfluidic device and and all the electronics required to implement the technique. All of this in a sophisticated and small electronic device. Secondly, the device is truly programmable; which allows the user to easily change parameters including frequency, voltage amplitude and electrode activation time through software. This is not a small thing given that most cell sorting devices of this kind are completely analogue. On the other hand, this device has some weaknesses. Maybe the most important of all is that it is not a continuous device which compromises the throughput of the technique. Another disadvantage is the fact that it uses positive DEP for cell manipulation. This often have some disadvantages because it exposes the target cells to high electric gradients in the edge of the electrodes. This is another example of the many DEP based microseparator devices which require the use of a *crossover frequency* to achieve particle sorting and hence an careful control of the medium's conductivity. How does this technique compares to our own? There a some similarities in the concept. This device, just like ours, was conceived to be self contained and portable, it uses DEP force to operate and is programmable. However, we believe all similarities end there. Our micro-particle separator works in a continuous way, uses negative DEP exclusively, and does not need a crossover frequency. Moreover, our technique is able to tailor *long range potential energy landscapes* through software. We will explain this in detail later in Chapter 4.

2.2 Pulsed Dielectrophoresis
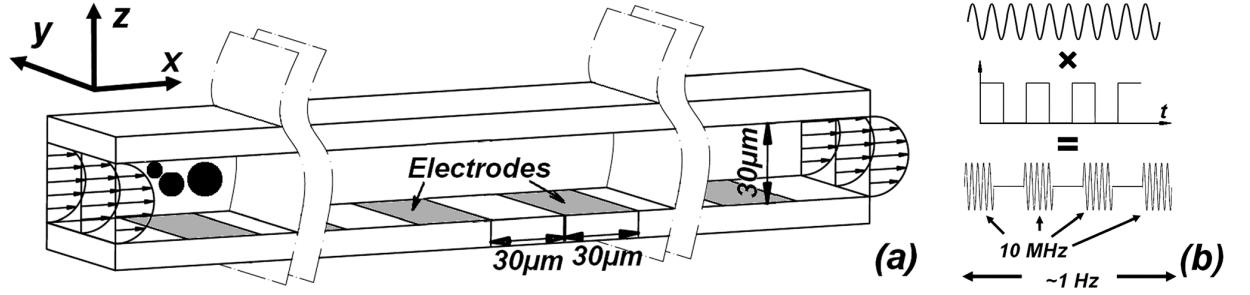
Figure 2.4: Pulse DEP: schematics. The interdigitated electrodes are patterned at the bottom substrate. a) Polystyrene beads are levitated using negative DEP at the same time the interaction between pulsed negative DEP force and a constant fluid flow enacts the separation of particles. b) Schematic illustrating how the applied pulsed AC signal is generated. Source: Hai-Hang Cui et al [43].

The majority of DEP-based separation methods apply DEP forces continuously in time, one emblematic example of this kind of techniques is DEP field-flow fractionation(DEP-FFF); which we will introduce in section 2.3. In this section will be discussing a DEP-based separation method that applies time-varying force fields for particle separation in microfluidics. This technique was introduced by Hai-Hang Cui et al [43].

This particular DEP separation technique relies on a direct competition between a constant fluid drag and a pulsed DEP force. A mixture of polystyrene particles of different sizes flows perpendicularly to an array of metallic electrodes patterned at the bottom of a microchannel, see Fig.2.4a.

This technique uses negative DEP exclusively in conjunction with drag force to sort particles. DEP force is used to levitate all the beads to the channel ceiling, see Fig.2.4, where the interaction of pulsed negative DEP force and fluid flow make the separation. One radius away from the top surface, the DEP force is given by [43]:

$$F_{DEP} = \frac{4\pi^2\epsilon_0\epsilon_f \text{Re}[K(w)]AV^2}{\lambda}\cos\left(\frac{2\pi x}{\lambda}\right) \tag{2.1}$$

Where A is a constant that takes into account the geometry of the model, V is the magnitude of the AC voltage applied to the electrodes, λ is the wavelength of the electrode structure.

$$F_{stokes} = -6\pi c_1 \mu r \left(U_p - U_f\right) \tag{2.2}$$
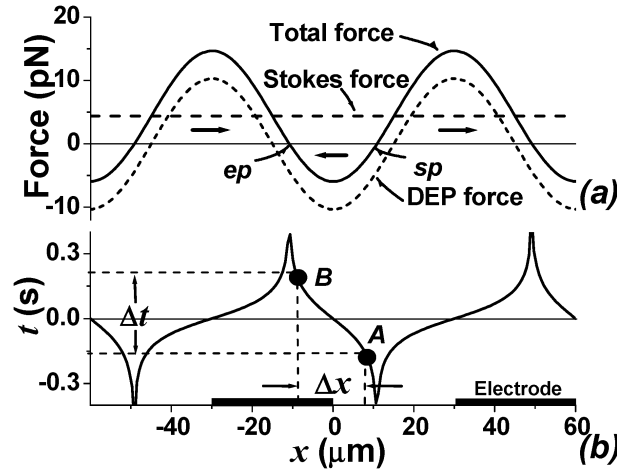
Figure 2.5: DEP force, Stokes force, and total force on a 5μm particle for an applied voltage V=20Vpp. Source: Hai-Hang Cui et al [43].

Taking into account a combination of drag and DEP forces we have a resulting force given by:

$$F_{total} = 6\pi c_1 \mu r \left(U_f - U_p\right) + F_{DEP} \tag{2.3}$$

here U_f is the local flow velocity, U_p is the particle's velocity, r is the radius of the polystyrene beads and c_1 is a correction factor.

$$U_f = \frac{6c_2 r \left(H - r\right)}{H^3 W} V_{flow} \tag{2.4}$$

where H is the height of the channel, W is the width, V_{flow} is a the volumetric flow rate, and c_2 is a second correction factor.

This method works by first turning on a negative DEP force to stop all particles upstream of the electrodes. Subsequently the DEP force is deactivated for a short period of time in order to release the particles downstream. Given that the force acting on particles of different size vary, see Eq.2.4, particles of different size will attain different velocities and reach different positions after a given time Δt. After this sort period of time some particles will have moved past the electrode, while others will not. By activating the DEP force again after a period of time Δt has passed, the particles not yet past the electrode will be pushed upstream(against the fluid flow) while the other will be pushed downstream. The key of this method is to tune the duration of the DEP pulse Δt as well as its strength in order to selectively trap our target particles at the same time unwanted particles travel unaffected through the microfluidic channel. In Fig.2.5 we have an schematic of the DEP force, stokes force and total force acting on particles in relation to the electrode geometry. We also have a representation of the points where the total force is zero: the stable equilibrium point (ep), the point where a particle is stopped and can not move; and the
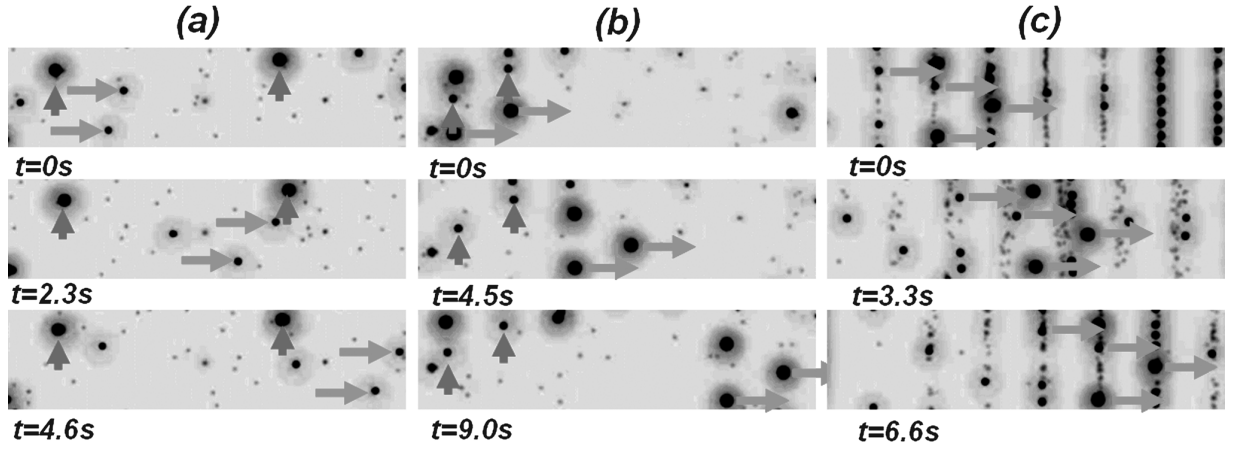
Figure 2.6: Pulsed DEP: particle retention using different settings. a) f = 2Hz and V=12Vpp; 10μm bead are retained while 3μm and 5μm bead are moved downstream. b) f=1.05Hz and V = 20Vpp; 5μm beads are retained while 3 μm and 10μm beads move downstream. c) f = 0.3Hz and V = 20Vpp; 3μm beads are retained while 5μm and 10μm beads move downstream. For this figure we have $\uparrow$ = particle moving forward and $\rightarrow$ = particle stopped. Source: Hai-Hang Cui et al [43]

unstable equilibrium point, here denoted as separation point(sp), where a particle passing this point will be pushed further away. In Fig.2.6 we have a some pictures intended to illustrate the separation of polystyrene beads of different size by a carefully selected set of values for the applied frequency, pulse duration and voltage strength.

2.2.1   Conclusions

In this work Hai-Hang Cui et al [43] introduced a new particle separation technique which depends on the tuning of a pulsed DEP force with a constant preexisting fluid force. This technique allows the user to retain particles of specific size by modulating the flow rate, magnitude of the applied AC voltage and the duration of the DEP pulse.

In the end, this is another example of a system that relies on competing forces of different nature for achieving cell sorting. It applies time varying DEP forces in conjunction with hydrodynamic forces to selectively retain particles of interest. This technique is simple and there is nothing fundamentally new in the sorting method itself; however, it is one of the very few instances of the use of pulsed DEP, which makes this technique relevant to our own work as we also apply pulsed DEP.

One disadvantage of this technique is that it is not a continuous method; which requires extra work for the recovery of the targeted particles. Moreover, it relies heavily on a steady and well controlled fluid flow rate as it is one of the key parameters for the sorting itself. Our micro-particle separator works in a continuous way and it does not relies on fluid forces to achieve particle concentration and sorting. However, it does use pulsed DEP forces but in our technique the electric fields switch faster than the particles can move

so that we can produce sum of forces from each electrode. We will explain in detail our technique later on in Chapter 4.

2.3 Field-Flow Fractionation
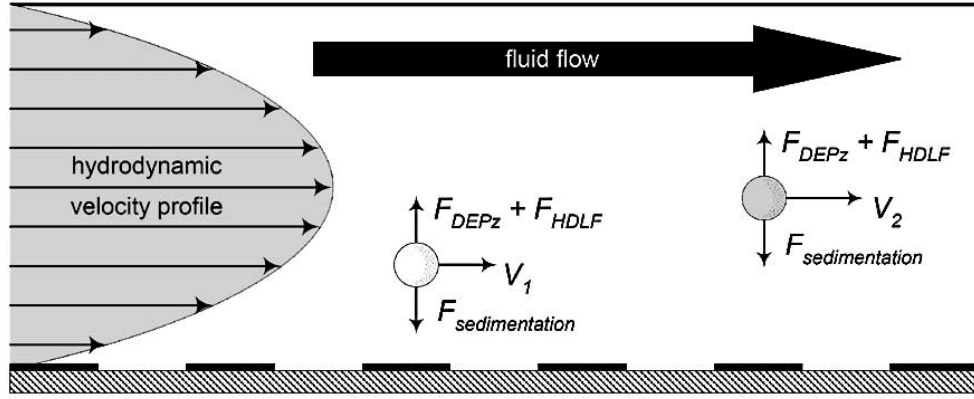
Figure 2.7: Dielectrophoretic field-flow fractionation: operational principle. Source: Peter R. Gascoyne et al [34]

DEP Field Flow Fractionation(DEP-FFF) is a particle separation methods in which particles are positioned within a fluid flow velocity profile using negative DEP forces. The goal is to fractionate a sample mixture of particles as they move throughout a microfludic channel, see Fig.2.7. This is done through the use of a DEP force to position different particle types at different altitudes in the fluid flow and hence achieving different characteristic velocities. As a result, the different particle types emerge from the device at different times. The main forces acting on particles are three: the particle sedimentation force, DEP force, and the hydrodynamic lift force(HDLF). The HDLF comes as a result of the migration of particles towards the fastest flowing region in the center of the channel. For a microfluidic system we have a flow velocity profile given by [34]:

$$v(h) = 6\langle v \rangle \frac{h}{H}\left(1 - \frac{h}{H}\right) \tag{2.5}$$

where h is the height of the particle in reference to the bottom substrate, $\langle v \rangle$ is the mean velocity, and H is the channel's hight. In this way particles of different type are carried through the microfluidic channel with a velocity given by Eq.2.5 at a equilibrium hight given by [34]:

$$h_{equilibrium} = \frac{d}{2\pi}\ln\left\{\frac{3\epsilon_m E_{RMS}^2 A_p}{2(\rho_c - \rho_m)g}\text{Re}(f_{CM})\right\} \tag{2.6}$$

where d is the separation between electrodes in the bottom substrate, ϵ_m is the permitivity of the suspending medium, E_{RMS} is the RMS electric field, A_p is a value that accounts for any reduction of the field's strength due to electrode polarization effects,
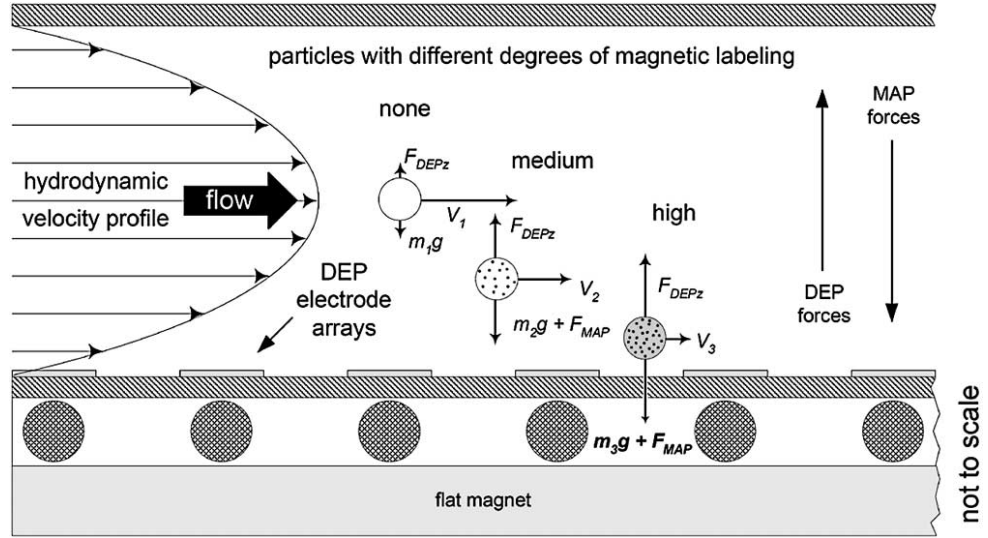
Figure 2.8: Magnetaphoretic-dielectrophoretic field-flow fractionation: operational principle. Source: Peter R. Gascoyne et al [44].

$(\rho_c - \rho_m)$ is the difference between the density of the particle and the suspending medium, and g is the acceleration of gravity.

As we can see from Eq.2.6, the equilibrium hight for a particle is fully defined in therms of the particle's electric properties and its density. The particle's levitation hight can be easily altered by adjusting the applied DEP voltage and frequency; which makes this technique ideal for a programmable device. In Fig.2.8 we have a variation of this technique in which in addition to a DEP and gravitational force we also have an opposing magnetic force to enhance the discrimination power of the technique. This variation is called magnetophoretic-dielectrophoretic field-flow fractionation(MAP-DEP-FFF) [44].

2.3.1 Conclusions

DEP-FFF and MAP-DEP-FFF are separation techniques that apply dielectrophoretic, magnetic and gravitational forces to position particles of different kinds at different equilibrium heights on a flow velocity profile and in this manner achieve spatial separation. This technique also exemplifies the separation methods that apply DEP forces in conjunction with external forces of a different nature. In this particular case we have magnetic and gravitational forces competing against DEP in order to achieve the characterization of particles of different kinds. The spatial separation of particles is done by giving particles distinct velocities as they move through a micro-channel. Even though these kind of techniques could become reliable and efficient enough for the fast sorting of micro-particles, they still rely on a careful characterization of the competing forces. Furthermore, we also have the added complexity that comes with the handling of extra external forces; which could make the device more complex and expensive. For example, magnetophoretic-

dielectrophoretic field-flow fractionation illustrated in Fig.2.8, requires the use of magnetic labeling on the target particles in order to take advantage of the technique.

The ideal DEP sorting technique would be one which does not require the application of external forces or tags on target particles; a technique that is also simple, reliable and cheap to implement. In Chapter 4 we will introduce a technique that does not rely on having an equilibrium between competing forces of different nature; one that relies solely on negative DEP force for the continuous sorting of particles.

2.4 Multiple Frequency Dielectrophoresis

In this work, Thomas Braschler et al [45] designed and built a particle sorter that applies more than one frequency simultaneously. This technique relies on the competition of lateral opposing dielectrophoretic forces; which focus particles of different type to different streamlines in a flow channel. Assuming constant gradient, the DEP force has a dependence on the applied voltage and real part of the Clausius-Mossotti factor in the following way [46]:

$$F_{DEP} = 2\pi\epsilon_m r^3 \mathbf{Re}(f_{CM})\nabla E^2 \approx \alpha \mathrm{Re}(f_{CM})V^2 \tag{2.7}$$

where r is the particle's radius, ϵ_m the permittivity of the medium, V the applied AC voltage and $\mathrm{Re}(f_{CM})$ the real part of the Clausius-Mossotti factor.
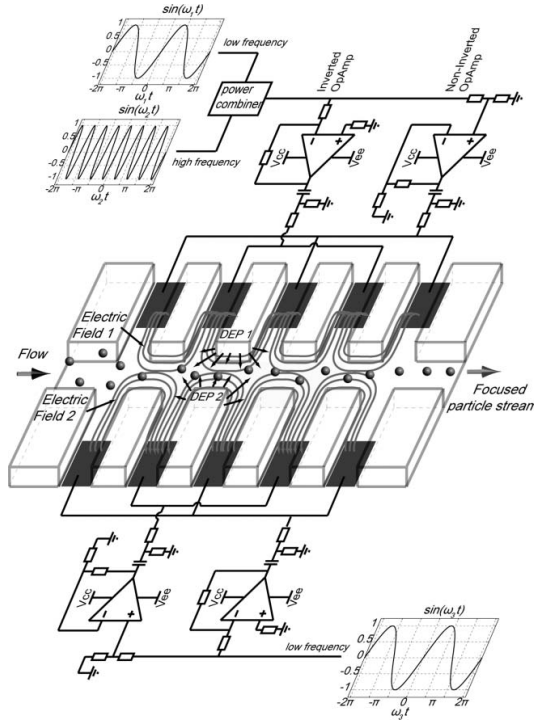
Figure 2.9: Diagram representing the main components in the multiple frequencies electronic device. The particles are affected by the two array of electrodes located in the sidewalls. In all these experiments three frequencies are used. Source: Thomas Braschler et al [45].

The DEP forces are generated by an array of liquid electrodes located in both sidewalls of the main flow chamber, see Fig.2.9. These two electrode arrays are powered with AC signals of different frequencies. The device uses three frequencies; a low frequency on each sidewall and a high frequency signal superimposed on one side only. In this way it is possible to focus a stream of particles towards different positions depending of the particle's dielectric response.

To generate the two arrays of electrodes on the sidewalls metal electrodes were patterned using standard lift-off technique on 550μm float glass wafers. Channels are then fabricated on top of the electrodes using a 20μm layer of SU-8. After this the chips are sealed by a flat piece of PDMS containing reservoirs. Subsequently the device is electrically connected to a printed circuit board using an electrical interface based on spring contacts.

As we can see from Eq.2.7, the DEP force experienced by the particles is proportional to the square of the applied electric field. From Eq.2.7 we can arrive to the following relation:
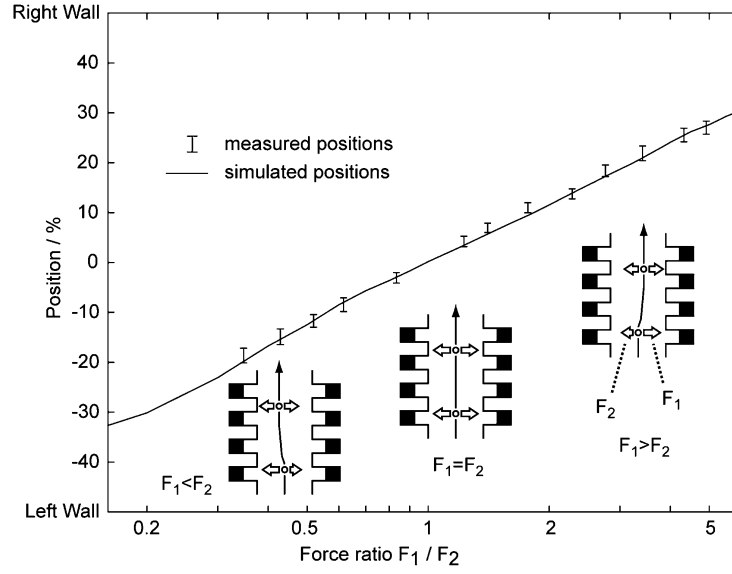
Figure 2.10: Calibration steps for the microfluidic device. Source: Thomas Braschler et al [45].

$$\frac{F_1}{F_2} = \frac{\text{Re}(f_{CM})_1 V_1^2}{\text{Re}(f_{CM})_2 V_2^2} \tag{2.8}$$

For calibration purposes a frequency range was chosen for which the Clausius-Mossotti factor remains constant for the polystyrene beads chosen for calibrating the system. In these experiments 5.14μm-diameter polystyrene bead were used. By varying the voltage applied to the two liquid electrode arrays it is possible to generate arbitrary ratios of force F_1/F_2 to focus the beads towards different positions in the channel, see Fig.2.10.

The device was tested for the separation of viable and nonviable yeast cells. A low frequency of 60kHz and 90kHz was applied to the left and right side respectively. For this condition we have all cells focused towards a common position, see Fig.2.11A. When adding a high frequency signal(100kHz) on the left side we have a particle stream moving towards the right as we can see on the cell count histogram in Fig.2.11B. However, there is no clear differentiation between the two distributions. In Fig.2.11C the frequency of the additional signal was increased to 5MHz; this time the viable cells are attracted towards the left side for a full differentiation between viable and nonviable cells.

2.4.1   Conclusions
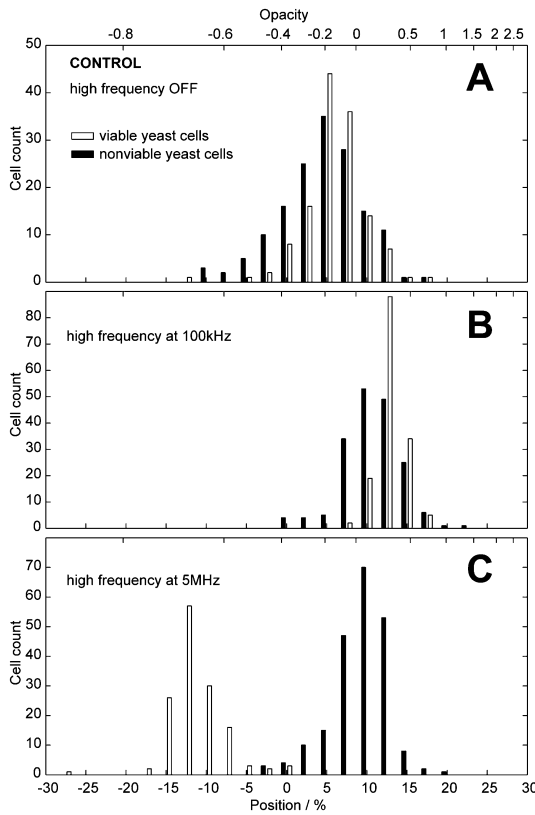
Figure 2.11: Experimental results concerning the separation of viable and nonviable cell using using multiple frequencies. A) Control experiment in which we have 60kHz and 90kHz and there is no high frequency. B) A 100kHz added to the left side. C) The high frequency signal was set to 5MHz. Source: Thomas Braschler et al [45].

This technique uses two competing lateral DEP forces to focus a stream of particles in different positions according to the particle's electrical properties; in a way forcing all particles moving through the channel to reach an *equilibrium* position on their own. This technique does not rely on extra external forces besides DEP and it has shown to be an effective way to differentiate and separate viable from nonviable Yeast cells, see Fig.2.11. However, this is a very binary sorting with the electrical properties of live and death cells being very different and not as sophisticated as sorting cell types. Moreover, given the short distance reach of DEP forces; which is typically around 30μm the microfluidic channel has to be narrow for the DEP forces to have an effect on the flowing particles. In this design the channel is about 20μm wide, which seriously compromises the throughput of the system. The ideal system would be one in which particles reach their equilibrium position on their own, just like in this case, but the applied DEP force is able to simultaneously affect particles in the entirety of a much wider microfluidic channel.

2.5 Spiral Electrodes

As mentioned previously, the DEP force a neutral particle would experience on a non-uniform electric field E is given by [31]:

$$F_{DEP} = 2\pi\epsilon_m r^3 \mathbf{Re}[K(\omega)]\nabla E^2 \tag{2.9}$$

In Eq.2.9 is valid for DC fields and stationary AC fields. However, if the phase of the AC field has spatial variations, we will have a DEP force given by [8]:

$$F_{DEP} = 2\pi\epsilon_m r^3 \mathbf{Re}[K(\omega)]\nabla E^2 + 4\pi\epsilon_m r^3 \mathbf{Im}[K(\omega)]\sum E^2\nabla\phi \tag{2.10}$$

where **Re** indicates the real part, **Im** the imaginary part and ϕ is the phase component of the AC field. The second term in Eq.2.10 accounts for the imaginary part in the Clausius-Mossotti(CM) factor, which depends on the frequency of the applied electric field and the complex permittivities of the particle and the suspending medium. The polarity of $\mathbf{Im}[K(\omega)]$ defines the direction of the particle's movement; which can be along or against the direction of the traveling field.

Figure 2.12: Diagram representing the electronic setup needed to generate a spiral electrode array. Source: Peter Gascoyne et. al. [47]

In Fig.2.12 we have a diagram showing a typical spiral electrode configuration used for the application of DEP forces in conjunction with traveling wave DEP to the sorting and concentration of cells. It consists of four interdigitated spiral electrodes that are energized by signals of the same frequency but phases of 0°, 90°, 180°, and 270° to generate a concentric traveling field that sweeps the targeted particles towards the center of the spiral. This sorting mechanism relies on the biophysical differences between cell types. Like many existing methods for bio-particle enrichment, this DEP technique depends on a cross-over frequency. As mentioned previously, this is the frequency where viable cells experience a transition between negative DEP to positive DEP; a viable cell would not experience a DEP force at this frequency. This frequency should be experimentally determined and carefully controlled in order to achieve an effective separation of bio-particles.

Figure 2.13: Separation of malaria infected erythocytes from uninfected cells. Malaria infected cells are concentrated towards the center of the spiral. Source: Peter Gascoyne et. al. [47]

One example of a typical application of this technique is the work of Peter Gascoyne et al. [47]. In that work human erythocytes infected by the malarial agent *Plasmodium falciparum* were separated from uninfected cells. In Fig.2.13 fluorescently labeled human erythrocytes infected with malaria (Plasmodium falciparum) have been separated from uninfected red blood cells. Infected cells are focused from a scattered state towards the center of the spiral. One of the main advantages of this technique is that it simultaneously uses the real and imaginary dielectric properties of the cells, see Eq.2.10.

In Fig.2.14 we have a second example of the application of the traveling wave DEP technique for the discrimination of cells using a spiral electrode array. This work is from Anoop Menachery et al. [48]. The images show the separation of trypanosomes from healthy erythrocytes. The trypanosomes are focused towards the center of the spiral at the same time healthy erythrocytes are sweep towards the periphery of the spiral.

2.5.1 Conclusions

The spiral electrodes technique has the capability of simultaneously applying positive and negative dielectrophoresis to exert a force on a binary mixture of particles in different directions. In Fig.2.13 and Fig.2.14 the technique makes use of positive and negative DEP in conjunction with traveling wave DEP to differentiate and concentrate malaria infected red cells and trypanosomes respectively. Unfortunately, according to P. Gascoyne et al [34] the generated forces are not strong enough to withstand hydrodynamic forces even from fluids flowing at low rates; which makes this technique impractical for a continuous sorting/concentration device and more suitable for static conditions. However, static separation/concentration methods generally make the target sample recovery difficult. Furthermore, this is another example of the use of a crossover frequency for the simultaneous application of negative and positive dielectrophoresis; which requires a careful control of the medium's conductivity, which could be difficult in a portable device for point-of-care diagnostic testing.
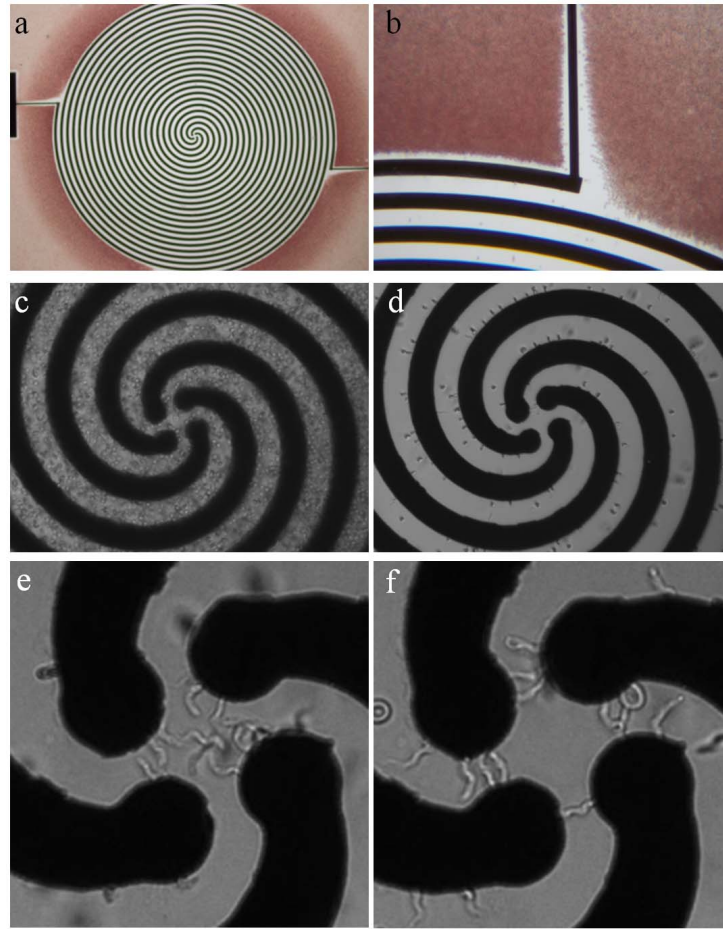
Figure 2.14: Spiral electrodes array. (a,b) The diameter of the spiral is about 2.9mm and the width of electrodes 30μm with a inter-electrode separation of also 30μm. (c-f) Enrichment of trypanosomes from infected blood using a spiral electrode array. Trypanosomes accumulate in the center of the spiral. Source: A. Menachery et al [48].

Chapter 3

Computerized Bio-particle Identification

Computer-aided Diagnostics(CAD) are procedures in medicine that assist in the interpretation of medical images. These techniques are commonly used in X-ray, MRI, and Ultrasound diagnostics. For example, CAD systems are used to support preventive medical check-ups in mammography(diagnostics of breast Cancer) and lung cancer [49]. Some very sophisticated computer-base techniques have been applied for aiding in blood count [50], anaemia identification [51] and even the detection of malignant melanoma [52] through the analysis of features in lesion images. However, the detection and identification of parasitic infections is still relying heavily on manual microscopic examination of blood samples [53]. A reliable automatic system for the detection and classification of different types of cells would be of great utility in this field.

Confirmatory diagnosis of parasites in body fluids is commonly done using bright field microscopy. The concentration of most parasites in blood is commonly low and the detection limits of some techniques are not good enough. Thick blood films, for example, have a detection threshold of 5000 trypanosomes per ml of blood [54]. Concentration methods are used to increase the concentration of parasites and hence the chances of detecting the parasite using microscopy. For example, the method used for the detection of trypanosomes in blood involves red blood cell(RBC) lysis, followed by the concentration and examination of the sediment by microscopy. Subsequently, thin smears made from sediment are stained with acridine orange and examined by fluorescence microscopy. This last step has shown to further enhance the sensitivity and speed of the method [53]; however, the detection of parasites by direct microscopy is still a challeng mainly because:

1. A large number of white blood cells are stained in addition to our target particles. The process of lysis and concentration leaves a large number of white blood cells stained intensely; this is the case for the detection of trypanosomes using acridine

orange and Giemsa [53].

2. Low parasitemia. Due to low parasitemia, the detection of particles of interest can be a stressful, tiring, and challenging even for a trained technician who would have to carefully scan a large number of particles to achieve a detection limit that is good enough for the particular application.

3. The use of fluorescence microscopy in clinical settings still requires sophisticated infrastructure [53]. Conventional fluorescence microscopes, for example, are expensive and delicate to operate.

4. The light emitted is not strong enough for a fluorescence microscope to be used outside a dark room [53].

We work towards the development of an aiding tool for the automatic detection and counting of biological or non-biological particles of interest in suspension. This tool should be able to work as a complement to the usual concentration methods e.g. red blood cell lysis and centrifugation, but eliminating the need for selective dyes to enhance contrast in particles. Our technique applies microfluidic technology, machine learning and normal video microscopy to scan a sample of diluted blood to detect and count particles of interest(white blood cells in this case). Our central goals/requirements for this work are:

- The detection of target particles in suspension using standard video microscopy without the use of any other technique to enhance cell contrast, like selective dyes.

- Versatility. Our computer vision application should be able to track and count polystyrene beads or living cells in suspension. Taking advantage of a group of distinctive shape and colour characteristics the software should be able to track and differentiate between micrometre-sized particles.

- Incorporate changes in the bottom substrate of our microfluidic channel. One of the biggest challenges when working with fluids in microfluidic channels is the accumulation of debris and other particles in our bottom substrate(background). Our software should be able to generate a background model that is capable of incorporating those changes.

In summary, we envision our software as an aiding tool for the automatic detection of target microparticles using a microfluidics channel, machine learning and normal video microscopy, but without the use of selective dyes to enhance the contrast in images of particles. In this chapter, we introduce the central aspects of our computerized vision system which is capable of detecting and identifying microparticles of interest as they pass through a microfluidic channel without the need for biomarkers, which can be done in real time or using pre-recorded videos. However, before going in full to the details of our software implementation we are going to spend a few lines introducing some previous work done in the field of automatic particle identification and counting. Hopefully, this will help us highlight the novelty, strength, and shortcomings of our approach.
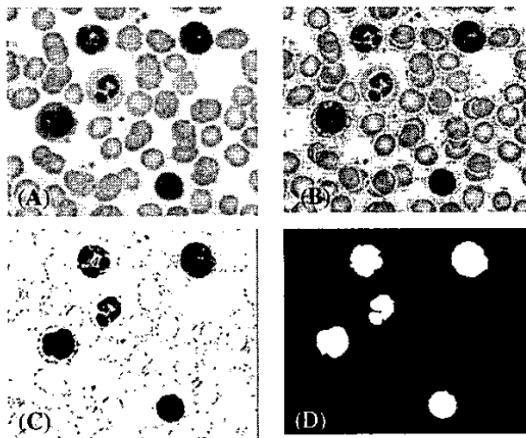
Figure 3.1: Intermediate steps for white cell identification. A) After converting the original image to gray scale. B) Contrast-stretched image. C) After applying an opening operation. D) After segmentation of image C. Source: Vincenzo Piuri et al. [55]

Some important work has been done previously regarding the fully-automated identification of bio-particles by digital microscope images. For example, Vincenzo Piuri et al [55] proposed a system for the identification and classification of white blood cells. Their system relies heavily on contrast stretching and edge detection to achieve a good image segmentation. For instance, during the extraction of the external membrane of white blood cells, the used steps are: contrast stretching, edge detection, dilation, and filling, see Fig.3.1. After segmentation, morphological indexes for each particle are computed in order to perform classification using a neural classifier. Some of the extracted morphological indexes are the following: Area, Perimeter, Convex Area, Solidity, Major Axis Length, Orientation, Filled Area, Eccentricity, Rectangularity and Circularity. These indexes are used to differentiate between five types of white blood cells by a classifier. The system was tested using sample-images extracted from an image repository. Even though the results indicate that the used morphological indexes make the classification of white blood cells achievable, this technique requires the use of a colourant to mark the white cell and in this way achieve a good segmentation. Moreover, this method only works on pre-recorded images and does not take into account red blood cells and platelets.

Another example of an automated vision system for the fast and accurate blood analysis is the work done by Mausumi Maitra et al [56] who developed an algorithm for the automatic location, identification and counting of red blood cells in microscopic blood cells images. Their algorithm uses edge detection, spatial smoothing filtering and histogram equalization as pre-processing steps for enhancing contrast and sharpening edges in the input images. After these steps, the detection of red blood cells relies on the Hough Transform, see Fig.3.2. This method uses the shapes and sizes of the located

Figure 3.2: Results of red blood segmentation after applying Hough transform. Source: Mausumi Maitra et al. [56]

particles in the input images in order to isolate red blood cells from the rest of the image. Even though the results obtained with this method are in agreement with the manual counting method, for now, it only works in bath mode. Moreover, the software does not take into account white blood cells and platelets.
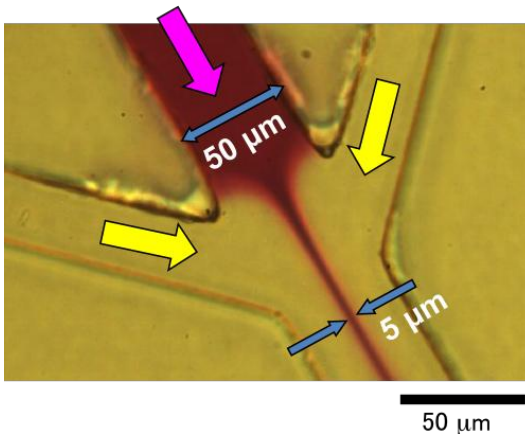
Figure 3.3: The lining-up of the biological sample is done using a three-forked sheath structure. Source: Masahito Hayashi et al. [57]

Regarding the identification of biological particles in microfluidic systems, some important work has been done previously. For example, Masahito Hayashi et al [57] developed an automated imaging flow cytometry system using a disposable plastic microfluidic chip. First, the microfluidic chip applies hydrodynamic focusing on lining-up the biological sample, see Fig.3.3. Subsequently, phase-contrast/fluorescence microscopy is used for real-time image processing and cell identification. First, a single background image is acquired and then images of particles flowing through the cell sorting area are acquired and the foreground image is obtained by subtracting the background image from each input image. Their image processing algorithm uses the particles area(in pixel units), mean intensity, length of the major and minor axis, and the degree of circularity as parameters in order to classify the particles in real time. Depending on the outcome of this classification, a DC voltage is applied to gel electrodes in order to separate the desired cells from the others using electrophoresis. The electrostatic force is only applied to cells which have to be removed; the target cells just flow down the laminar flow.

In summary, the authors developed an imaging cytometry system able to separate target cells. In order to accomplish that they combined different technologies into a single system that uses a fluorescent dye, electrophoretic force, and real-time image-recognition to discriminate between particles as they flow through the channel of the microfluidic chip; however, their method stills require the use of a fluorescence dye in order to enhance cell contrast. Also, the background model they use is unable to incorporate changes. At the beginning of the image processing, a single background image of the observation area is acquired. To obtain the image of the flowing particles(foreground), the background image is subtracted from the incoming frame and then binarized in order to start the segmentation process. This simple background subtraction method plays a very important role in defining the boundary of a particle in an image. Another shortcoming of the technique is the need of a buffer flow for particle focusing. The lining-up of the sample is done through hydrodynamic focusing which is generated by a three-forked sheath structure, see Fig.3.3. The algorithm also lacks adaptability in the sense that it was not designed to be flexible or easy to adapt for the detection of cells with different morphologies e.g. Trypanosoma. We believe that a bigger set of predictors and a pattern recognition algorithm able to learn and make predictions from the input data would be more suitable for the challenge of particle recognition/classification. Our computerized vision system was developed in C++ and makes extensive use of **Open source Computer Vision(OpenCV)** [58] libraries and a Support Vector Machine(SVM) algorithm [59] for feature extraction and image recognition respectively. The improvements and unique features of our algorithm(relative to previous work) is summarized in the next few points:

$\diamond$ The detection of target particles is done using standard video microscopy without the use of any other technique to enhance cell contrast e.g. selective dyes.

$\diamond$ Our generated background model is fully capable of incorporating changes. Our computer vision system is able of dealing with changes in the bottom substrate of our microfluidic channel.

$\diamond$ The chosen set of predictors and pattern recognition algorithm makes it able to learn and make predictions from the input data. Our computer vision system uses a specially chosen group of morphological characteristics. These characteristics or predictors represent a compact and robust description of the shape of an object, see Section 3.3.1. Also, the algorithm used for bio-particle classification is a *supervised machine learning model*: Support Vector Machine(SVM). We believe this characteristic actually makes the system more flexible regarding the range of possible applications. It could be used to differentiate red blood cells from white blood cells or to differentiate between a person and a car on a street.

◇ It does not require a buffer flow for particle focusing. Our system is capable of tracking and analyzing multiple particles simultaneously.

◇ Laser-based cytometers are available for the counting of blood cells; however, our method is image based and hence does not destroy the blood sample during analysis.

◇ The implementation of our algorithm was entirely made using open access tools. For instance, for image processing, we applied OpenCV with a C++ interface. Unlike proprietary software like MATLAB, which almost always have major restrictions on its use, each one of our tools can be accessed freely on the web by anyone.

In general terms, our computer vision system can be divided into two main parts: multi-particle tracking and particle identification. Similarly, these two main parts are divided into smaller steps. For multi-particle tracking we have: static background subtraction, apply morphological operations, image segmentation, particle tracking. On the other hand, for particle identification, we have the following steps: feature extraction, training of the particle recognition system, particle classification and image retrieval.

As we can see, multi-particle detection and tracking is a multi-step process that needs to be carefully implemented, structured and commented. Each one of the involved steps requires a careful selection and implementation of the algorithms and techniques that best suits our needs and the fine-tuning of some variables. Here we are going to give a brief overview of the main components of our computer vision system before giving a detailed description in the next sections.

1. **MULTI-PARTICLE TRACKING.**

    (a) **Static background Subtraction**: we subtract the background on each frame in order to extract the features of interest. To achieve this we applied a Gaussian Mixture Model [60] which is able to deal with background objects that are moving slightly; which represents a improvement over the standard background subtraction techniques.

    (b) **Apply morphological operations and filters**: we apply a group of morphological operations(dilation, opening, erosion and closing) [61] and other noise reduction techniques to better differentiate true particles from debris and noise.

    (c) **Segmentation**: once we have a clear foreground image we proceed to extract the image shapes corresponding to each individual micro-particle.

    (d) **Track particles**: using Object Oriented Programming(OOP) we give each individual particle an identity which helps to keep tracking of each one as they move throughout a frame. We do this by updating the particle's coordinates, which are given by the *centroid* (in pixel units) of each particle's shape, to the closest match in the next frame.

2. **PARTICLE IDENTIFICATION.**

    (a) **Feature extraction**: in oder to identify objects or to compare them with other components we need to perform some measurements and extract their main characteristics; here we define this specific characteristics as *predictors*. This properties are needed in the structural analysis of shapes. For example, some of the predictors we will be using in this work are: enclosing area(number of pixels inside), the contour of a particle, and the area of the minimum enclosing rotated rectangle in that shape. The most general version of this program includes fifteen predictors of different nature; which were carefully selected to achieve good performance under non-ideal circumstances.

    (b) **Train pattern recognition system**: nonlinear Support Vector Machine(SVM) is used to classify the particles in two classes through a hyper-surface in a high-dimensional space. In order to achieve a good separation we need to define the optimal hyper-surface. This is done through a proper training of the system using a large number of positive and negative sample that are fully labeled.

    (c) **Particle classification**: SVM can be applied to multi-class classification; however, this requires an algorithm that reduces the multi-class task to several binary problems. For this applications we only focus on two-class classification. Once the system has been properly trained using a relevant training data set we can proceed to make the relevant classification of bio-particles.

    (d) **Image retrieval**: Once the particle classification is done. The program proceeds to locate and retrieve a video segment showing every positively identified particle in the video. This is automatically done by the program for each one of the identified particles of interest. The idea is to make it easier for the user to locate the identified particles in the video and/or make a visual confirmation of the results.

    The program also displays on screen the number of identified particles and the total number of particles detected. It also generates a database containing the ID number, video file location and all the computed predictors for each one of the micro-particles found in the video.

As mentioned previously, it is also important for us to make the original source code fully contained and freely available so that anyone can improve it or adapt it for different applications. Following this idea, we made use of C++, Linux, OpenCV and other open-source tools. All the libraries and data analysis tools used for this work are freely available. OpenCV, for example, is a library that contains hundreds of algorithms for real-time image analysis and it is free for use under the open-source BSD license.

A computer sees an image as a matrix of numbers where each element in the matrix represents one pixel. In OpenCV the cv::Mat data structure is of particular importance because it is used to manipulate images as matrices. In fact, here an image is a matrix from a computational point of view. For example, on a grey-level image, the numbers in the matrix are positive 8-bit values where 0 corresponds to black and 255 to white. For a colour image we have three numerical values per pixel; each one corresponding to one of the three primary colours (Red, Green, Blue). Colour images use multiple channels for each pixel [62]. For instance, if we need to convert between colour representations and split the same colour image into their components channel images. Using C++ and the OpenCV library, this can be done using the **cvtcolor** and **split** functions [62] in just a few lines of code, see Appendix A.

All the processing functions are applied to each acquired frame of a videos sequence automatically. For convenience, we have encapsulated all our **OpenCV** video processing framework in a single class. Our easy to use C++ class implements all the high-level instructions for the different image processing steps. The whole work regarding this chapter can be seen as *stand-alone* image processing tool. The source program is a completely open source and self-contained. It is able to read, process, store, and display results. A supervised machine learning model(SVM) is used to identify the objects of interest. For object detection, it learns to identify objects(cells) based on a set of positive and negative samples. In this regard, we can say that our system is capable of learning and its performance is also dependant on the size and quality of the used training dataset; however, there is no clear answer to how much training data set is needed in order to achieve good predictive performance, this question should be answered through empirical investigation. Sometimes, when training data is not fully available, expensive, or just too difficult to obtain, a compromise must be made between the quantity of labelled data used for training and the predictive performance of the computerized system for that particular purpose. We will come back to this point later on in Section 5.1. We believe the leaning capability of our system is another strength of our model as it broadens the range of possible applications. In this work, we experiment with the detection and classification of micron-sized particles; however, the software could be easily adapted for a different task, the location and differentiation between brand logos, for instance.

3.1 Experimental Setup

Before going in depth about the several processing steps in our image recognition system we will spend a few lines describing the experimental setup used in our experiments. In Fig.3.4a we have a general diagram intended to represent our experimental setup. The
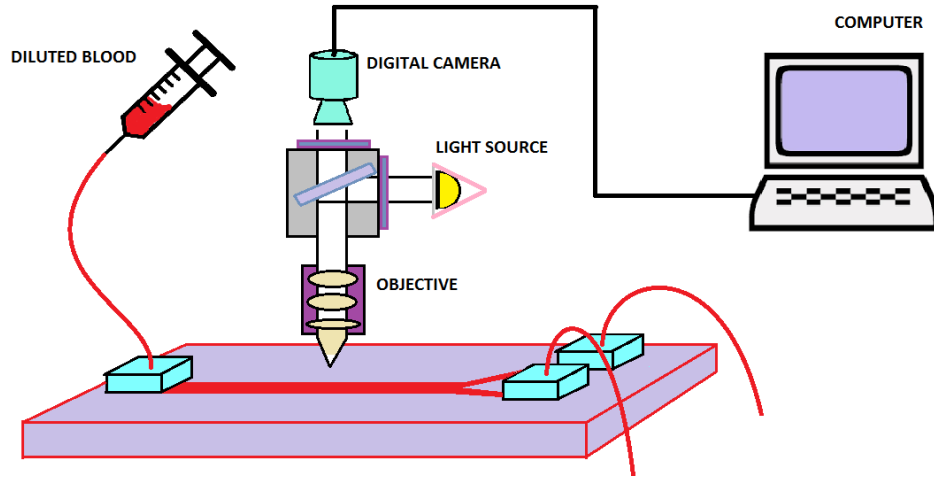
(a)
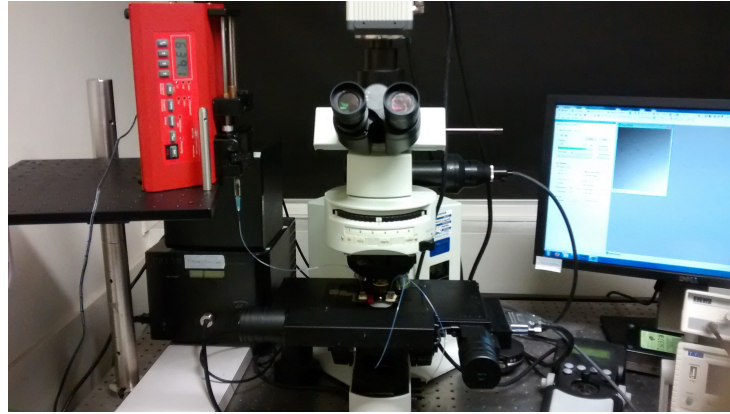
(b)
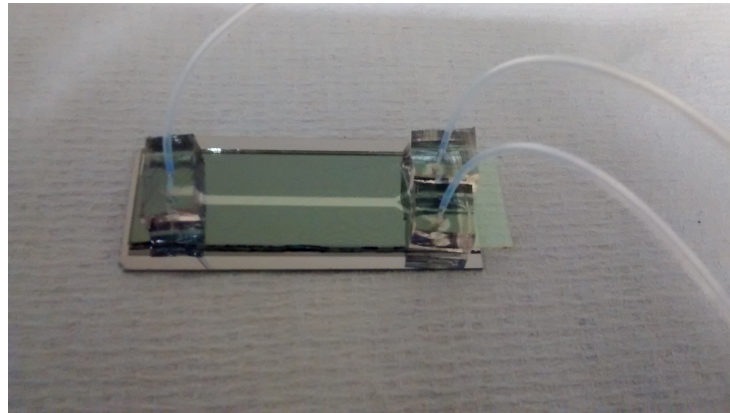
(c)

Figure 3.4: The main components in our experimental setup are: microscope, digital camera, micro-fluidic channel, syringe pump and a computer. a) Diagram of the experimental setup. It consists of a microfluidic channel mounted on the programmable stage of an upright microscope. The digital camera mounted in the microscope is used to capture images which are subsequently analyzed by a computer. b) An actual picture of the experiment taking place. A diluted blood sample is been delivered to the microfluidic channel at a flow rate of 2μL/min using a syringe pump. As the particle flow through our micro-channel, the captured images of particles are analyzed by our software. c) Micro-fluidic channel: one inlet and two outlets. The channel is 1.2mm wide, 4cm long and 100μm high.

microfluidic chip we need for this experiments has some particular characteristics that can not be achieved using standard techniques like PDMS-glass technology. A new technique is needed in order to achieve a device that is transparent and thin enough to be used with standard microscopy.

In Fig.3.4b we have an image of our experiment taking place. We have a micro-channel(100μm high by 1.2 mm wide) mounted on the stage of an upright microscope (Olympus BX51), a 1.0mL gas-tight glass syringe(MDN-0100 BASi), a syringe pump(NE-1000 New Era Syringe Pump System), a digital camera(Hamamatsu C11440) and a laptop computer. A diluted blood sample in PBS(0.25% v/v) is delivered to the microfluidic channel at a flow rate of 2μL/min using a syringe pump. A digital camera is used to record the bio-particles flowing through for later analysis.

The microfluidic channel shown in Fig.3.4c was fabricated by patterning SU8 resist on a silicon wafer using the standard lithographic process; the device has one inlet and two outlets. Here we are reusing a microfluidic channel that was originally designed for a continuous micro-particle sorter device(chapter 4). The idea behind having two outlets was to be able to easily collect the processed sample and residues at separate points. The bottom substrate is a cut to size silicon wafer, which has a high refractive index and gives good microscope images when the device is illuminated using upright reflective bright field microscopy. A layer(100 micrometres thick) of SU8 was spin coated onto the silicon substrate. Subsequently, the top ITO(already containing the predrilled holes) was immediately placed on top of the SU8 layer. This gives us a glass-polymer-glass structure in which our photoresist layer defines our channel geometry and acts as bonding agent at the same time, see Fig.3.4c. The exposure takes place through the top substrate(ITO-glass cover slip). Tubing was connected to the pre-drilled holes in the upper glass wafer through PDMS blocks that where bonded to the glass surface. If the reader is interested in more details regarding the channel fabrication those can be found in section 3.1 of Chapter 4. The exact same protocol is used for the fabrication of the microfluidic channel in our cell sorter device.

In the next sections will give a detailed description of the different steps involved in multiple-particle tracking and particle identification. Even though we will cover the fundamental concepts and techniques behind each one of the steps involved we will not give an extensive review of the several methods applied throughout this work. For specific details regarding the implementation of each step, the reader could refer to the source code which contains a properly commented description of the main sections in the code.

3.2 Multiple Particle Tracking

Tracking of multiple objects in video is a complex problem in computer vision. It has been approached in a variety of different ways. For example: Feature Point Tracking, Mean Shift, and Exhaustive Search have all been used. In colloidal science often a particle will have a bright center which can be used as a recognizable feature [63,64]. Techniques like these work effectively under a well controlled environment, and/or when the object we wish to track has enough stable and particular features that can be matched from frame to frame. However, in most real applications this is not the case. Take Exhaustive Search for example, in this technique a template is compared in every position using some metric; however, it is very likely the tracked object will change its appearance as it moves away or towards the camera. In other words, the appearance of the object will change just by changing the viewpoint of the object with respect to the camera. Given the huge possible changes in appearance for a single object, this technique is not the best option when dealing with bio-particle tracking. In this section I will give a very general description of the algorithm we developed to track many particles simultaneously. The C++ implementation of this algorithm allows us to successfully track multiple particles at the same time even under far from ideal conditions. Object Oriented Programming (OOP) and Gaussian Mixture Model play an important role in this work.

3.2.1 Static Background Subtraction

In our experimental setup we have a fixed camera observing a scene in which the background remains mostly unchanged. In this case the scene is a diluted blood sample flowing in a microchannel, see Fig.3.5. The background is the bottom substrate of our device. We are interested in the moving objects in the scene; in our case these objects are blood cells. The background remains mostly unchanged, but this is not always the case as there could be slight changes in illumination, debris and/or blood cell attachment to the bottom surface of our device, to mentions just two examples, later on electrodes will also feature. In order to extract the foreground objects we first need to build a model of the background that is able to deal with this kind of change, and then compare this model with a current frame in order to detect true foreground objects. In an attempt to incorporate background changes Stauffer and Grimson [65] developed an algorithm that models each pixel in a frame using a mixture of Gaussian distributions(Gaussian Mixture Model). This is a considerable improvement over standard background subtraction techniques like static background subtraction and running average [66]. The central idea of the Gaussian Mixture Model technique is to fit multiple Gaussian distributions to all the previous pixel data; which includes background and foreground. This means that for a given frame(m) each of the Gaussian distributions has a weight($\pi_n(i,j,m)$) depending of how frequently it

has occurred in the previous frames. When considering a new frame, each point $f_n(i, j)$ is compared to the Gaussian distributions currently modeling that specific point in order to determine the closest Gaussian distribution; in case there is any. As a norm, a distribution is considered close if it is within 2.5 times the standard deviation from the mean value. However, if no close Gaussian distribution is found then a new Gaussian distribution is generated to model this pixel. On the contrary, if a close Gaussian distribution is found, then that distribution is updated with this new point. Now, one of the important aspects here is that for each point $f_n(i, j)$ the largest Gaussian distributions are considered to represent the background. A pixel in a new frame is classified as foreground or background depending of whether its associated distribution corresponds to foreground or background respectively.

For this algorithm the distributions are updated according to the following rules [65]:

$$
\begin{aligned}
\pi_{n+1}(i, j, m) &= \alpha O_n(i, j, m) + (1 - \alpha)\pi_n(i, j, m) \\
\mu_{n+1}(i, j, m) &= \mu(i, j, m) + O_n(i, j, m)(\alpha/\pi_{n+1}(i, j, m)) \\
&\quad + (f_n(i, j) - \mu_n(i, j, m)) \\
\sigma_{n+1}^2(i, j, m) &= \sigma_{n+1}^2(i, j, m) + O_n(i, j, m)(\alpha/\sigma_{n+1}(i, j, m))((f_n(i, j) \\
&\quad - \mu_n(i, j, m))^2 - \sigma_n^2(i, j, m)) \\
\text{where } O_n(i, j, m) &= \begin{cases} 1 & \text{for the close Gaussian distribution} \\ 0 & \text{otherwise} \end{cases}
\end{aligned} \tag{3.1}
$$

Where $\pi_n(i, j, m)$, $\sigma_n(i, j, m)$ and $\sigma_n(i, j, m)$ are the weighting, average and standard deviation of the mth Gaussian distribution for pixel (i,j) at frame n.

In order to process a video sequence, we need to be able to read each one of its frames sequentially; we want to apply the same processing function to each frames of our video sequence. In our C++ implementation we do this by encapsulating our code into our own class. Then we crate a loop that will extract and process each video frame. We specify a processing function that will be called once for each frame of a video sequence. This function was defined as receiving a cv:Mat instance and outputting a processed frame of the same kind. In our processing function, the implementation of background subtraction is done easily just by creating a class instance and calling the method that simultaneously update the background and returns the foreground image, see Appendix B.

To illustrate background subtraction and other image processing techniques we will use a single image instance from our video sequence, see Fig.3.5. It corresponds to a sample of diluted whole blood flowing through our microfluidic channel; in the image we can see several red blood cells and a single platelet. First we apply static background subtraction to Fig.3.5. As explained previously the Mixture of Gaussian method can deal
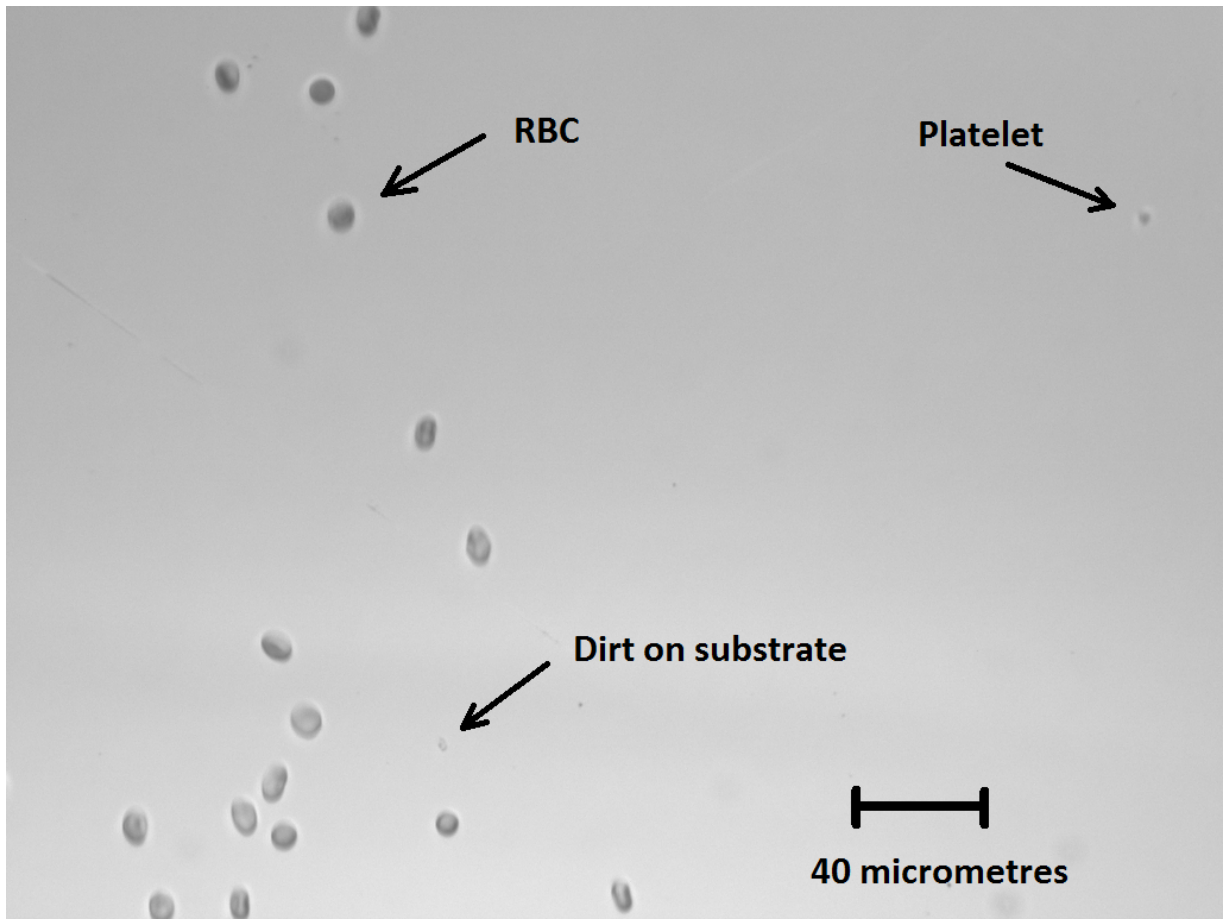
Figure 3.5: A single image instance from a video sequence: diluted whole blood flowing in our microfluidic channel at a flow rate of $2\mu\text{L/min}$. The image is a 32-bit colour image(1024 $\times$ 768), it was obtained using a digital camera(Hamamatsu C11440) mounted on the stage of an upright microscope(Olympus BX51). The image has three channels corresponding to red, green and blue wavelengths(RGB). In this particular frame we have red blood cells and a single platelet.

with a background that changes over time. This technique is very successfully applied and commonly found in video surveillance applications. What makes this technique particularly suitable for our needs is that in can successfully deal with changes in the substrate. It can incorporate a fair amount of changes in the background(substrate) due to debris and cell attachment to the bottom of our device and even slow changes in illumination; all relative to the speed of moving particles. As already mentioned previously, we constantly update the background image to account for lighting changes. We control how fast our background adapts to lighting or other changes through α. For all the experiments in this section, we used $\alpha = 0.01$. In essence, we build a model of the background that is constantly improved and updated.

Next comes one of the most fundamental tasks for image processing. We need to clear the image from noise and selectively extract certain regions of the image that could contain
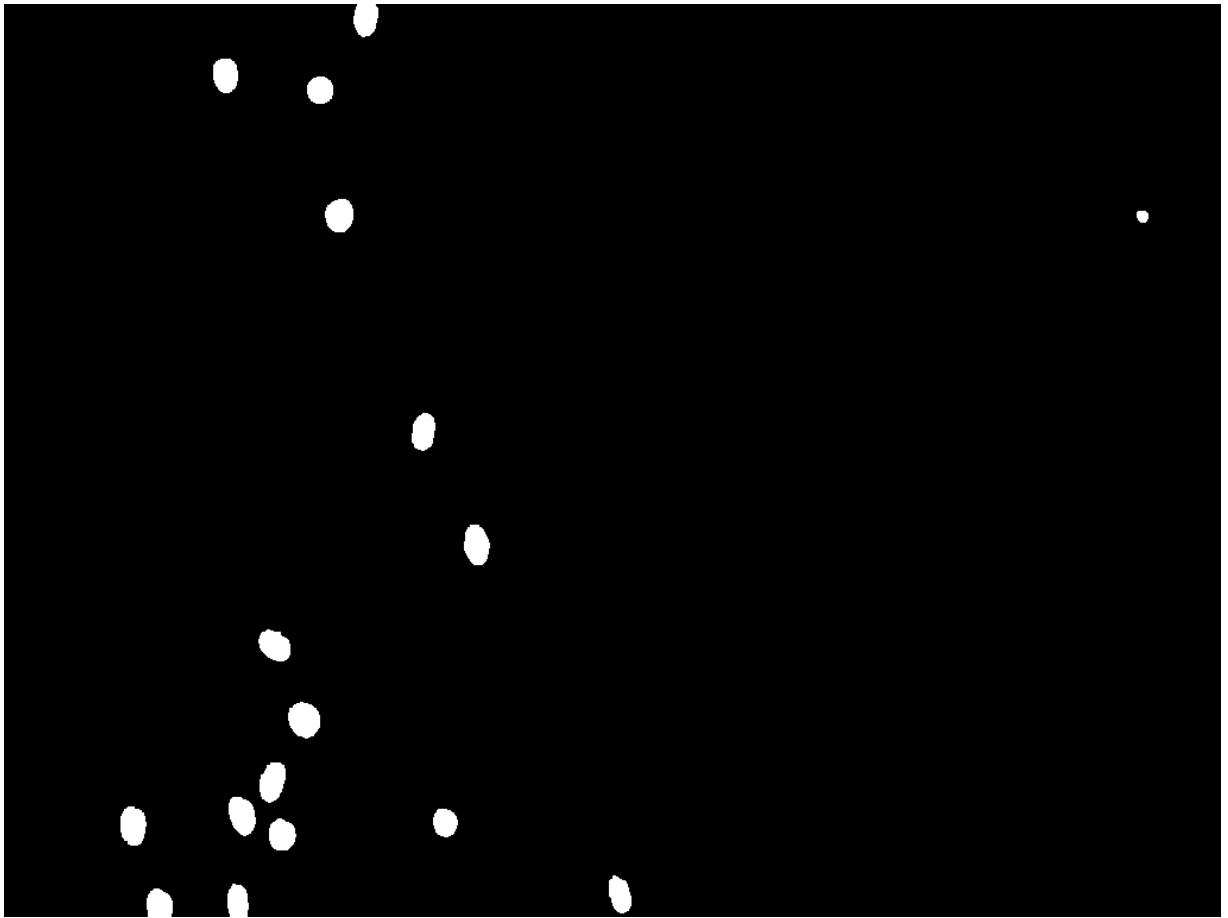
Figure 3.6: Binary image obtained after applying background subtraction and morphological operations on the original image to filter noise and debris.

important information for our particular application. We apply some high-level morphological operations to filter the image and reduce noise. First we apply a closing filter to re-connect the objects that where erroneously fragmented and to fill holes. Subsequently, we apply an opening filter to remove small image noise, Fig. 3.6 shows the result obtained after these operations. Closing and opening roughly maintains the size of objects, see Appendix C. After doing this we proceed to segmentation; segmentation is the process of dividing the image in multiple segments that could or could not correspond to particles. We will discuss a bit more about image segmentation in the next section. For now, we can see an example of image segmentation in Fig.3.7.

3.2.2   Tracking Multiple Particles Simultaneously

After obtaining a binary image of the foreground, which was explained in the previous section, we proceed to locate all foreground objects. First we will proceed to segment the image. As mentioned previously, image segmentation is the process of dividing the image into multiple segments of interest that could or could not correspond to objects of interest,

Figure 3.7: Result obtained after implementing the segmentation step. The obtained contours are drawn into our original image.

see Fig.3.7. In this step we extract the connected components in the image. In other words, shapes made of a set of connected pixels in our binary foreground image. Naturally, the input in this step is the binary image we previously obtained during background subtraction, Fig.3.6, see Appendix D for mode details.

The contour of each shape in the image is represented as a vector of **cv::Points** and stored in a vector container **cv::vector**. For the actual implementation, a flag is necessary to indicate that we are only interested in the external contours; holes inside shapes will be ignored. In OpenCV we can extract the contours of a binary shape through the function **cv:findContours**.

```
1  vector< vector<Points> > contours;     // a vector to contain the contours
   findContours(image,                     // our input image
3  contours,                               // a vector of contours
   CV_RETR_EXTERNAL,                       // retrieve only the external contour
5  CV_CHAIN_APPROX_NONE );                 // all pixels of each image
```
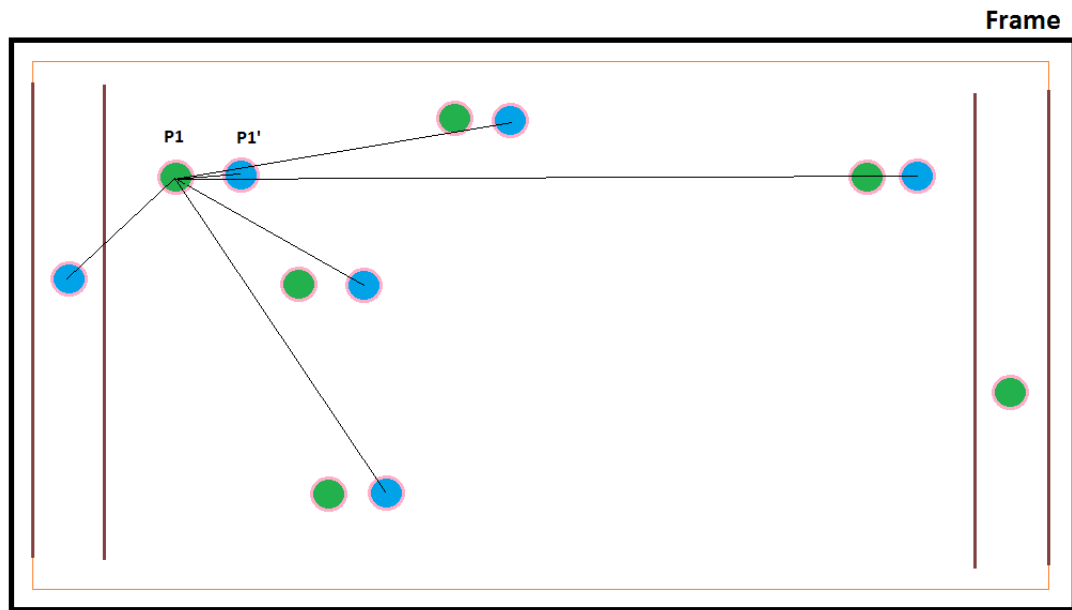
Figure 3.8: Diagram intended to make a graphical representation of the technique used for multi-particle tracking. A particle's coordinates(P1) on a given frame(red) are updated with the coordinates of the closest particle (P1') in the next frame(blue).

Under most circumstances we also have some extra information related to the size of the objects we will expect to find in the image. This gives us the option to discard contours that are too big or too small. In our particular application objects that are too small would normally correspond to noise or debris. On the other hand, objects that are too big will normally correspond to clusters of cells. Appendix E contains the implementation of these steps. In Fig.3.7 we have the results obtained after implementing the segmentation steps on Fig.3.6 and drawing these contours back into the original image; as we can see the final result is a good match. We have a good definition of the boundaries for each one of the detected particles. Please note that for this particular frame we have a several red blood cells, no white blood cells and a single platelet.

The next challenge is to automatically track all those objects through several frames; we must find where those objects are located from one frame to another. Obviously, since we are dealing with moving objects we should expect the position of these objects to changed in the next frame. In addition to this we also have the challenge of having to deal with multiple particles moving simultaneously and possibly some remaining noise from the background subtraction step.

When the program is executed over a video sequence it does not start the image segmentation and particle tracking steps immediately but instead uses the first ten frames to generate a good starting background model. We consider a background model to be good enough if it is able to identify all the background objects and moving particles correctly. For our considered leaning rate(α=0.01), we have observed experimentally that

10 frames seems to be the minimum number of frames necessary to generate a good background model. Of course, we can use a bigger number of frames to define it; however, that will delay the stating of the image processing steps that are next in line. A good compromise is needed between the number of initial frames used for the definition of our background model and the processing time required for such step. This step is particularly important because all the subsequent processing steps relay on having a good background model. Of course, the time needed will depend of the particular scene and frame rate used. For all our experiments ten frames seems to be enough to achieve a good starting background model.

Now is the right time to introduce one of the most powerful mathematical entities included in the OpenCV libraries: **Central Moments**. Central moments are commonly used for structural analysis of shapes and we will be making extensive use of these entities later when dealing with image recognition. For now we will use **central moments** just to locate the *centroid* of each one the the detected particles/contours on the frames. For a digital image with pixel intensity $I(x, y)$ the *raw moments* $M_{i,j}$ are defined by [67]:

$$M_{i,j} = \sum_x \sum_y x^i y^j I(x, y) \tag{3.2}$$

The central moments [67] are moments taken of a probability distribution around the mean of our random variable.

$$\mu_{p,q} = \sum_x \sum_y (x - \overline{x})^p (y - \overline{y})^q f(x, y) \tag{3.3}$$

where $\overline{x} = M_{1,0}/M_{0,0}$ and $\overline{y} = M_{0,1}/M_{0,0}$ are the coordinates of the *centroid*. This mathematical entity is very useful for us because it does not only allow us to get some useful predictors for image recognition but also let us compute the area and the coordinates of the centroid of each particle in an easy and reliable way.

To calculate the area of a binary image(e.g. black and white, with the particles pictured out in white) we need to compute the zeroth moment: $\mu_{0,0} = \sum_x \sum_y x^0 y^0 I(x, y) = \sum_x \sum_y I(x, y)$; given that in our binary image a pixel $I(x, y)$ is either 0 or 1. This means for each white pixel a 1 is added to the moment. As an end result we have the sum of white pixels; effectively calculating the area of the binary image.

To calculate the centroid of a binary image we need two coordinates: x and y. For the x coordinate we must calculate $\mu_{1,0}/\mu_{0,0}$ and for the y coordinate $\mu_{0,1}/\mu_{0,0}$. To make sense of this quantities lets first consider the row moments for x : $sum_x = \sum \sum x I(x, y)$, which gives us the sum of x coordinates for all white pixels; we must remember that for our binary image $I(x, y) = 0$(dark) or 1(white). Similarly, $sum_y = \sum \sum y I(x, y)$ gives us the sum of y coordinates for all white pixels. Now we have the sum of all all white pixels' x and y coordinates. To get the average we need to divide each by the number of white

pixels, which is given by $\mu_{0,0} = \sum_x \sum_y I(x,y)$.

As summary, for the area of a object(in pixel units) we have:

$$Area = \mu_{0,0} = \sum_x \sum_y I(x,y) \tag{3.4}$$

In the same manner, the x and y coordinates of the centroid of a particle is given by:

$$x = \mu_{1,0}/\mu_{0,0} = \sum_x \sum_y x I(x,y) / \sum_x \sum_y I(x,y)$$
$$y = \mu_{0,1}/\mu_{0,0} = \sum_x \sum_y y I(x,y) / \sum_x \sum_y I(x,y) \tag{3.5}$$

In OpenCV we have a data structure that encapsulates all computed moments in a shape; which is an object returned by the **cv::moments** function. A section of the actual implementation of this function can be found in Appendix F. In later sections we will learn that in addition to an easy computation of *area* and particle's centroid, the moments give us an easy and compact description of the shape of an object.

Now that we have a efficient way to compute the position for each particle we proceed to do the simultaneous tracking of particles through the frames. A fragment of the implementation of this can be found in Appendix G. In order to do a successful tracking of all the particles at once, we first compute the distance from each particle in the current frame to every single one of the particles in the next frame, see Fig.3.8. Subsequently, we update a particle's position with the position of the particle with the minimum distance. The minimum distance should correspond to the position of the particle in the next frame, see Fig.3.8; this assuming the frame rate of the video capture is not too low. The matching of the particle's coordinates from one frame to another is possible by giving each one of the particles an identity. This is achieved through the use of object oriented programming(OOP). We define a particle class that contains an ID number that is unique for each tracked particle. It also includes all the other properties like particle's coordinates and all the extracted predictors. In other words each particle has unique identity and characteristics, which serves us very well for giving individuality to each one of the particles in in the video sequence.

A particle ID number is assigned to each **new** particle coming into the frame. The distance from each particle to *all* the particles in the next frame is computed, see Fig.3.8. After this we update the particle's coordinates in that frame(red) with the coordinates of the closest particle in the next frame(blue). The particles that do not have a match in the previous frame and are located in a particular region of the frame(far left), see Fig.3.8, are those particles that appear for the first time in the frame; for these particles the program generate new instances of the class particle and assign them unique ID numbers. On the

other hand, the particles that do not have a match in the next frame and are located in a specific region of the frame(far right), see Fig.3.8, are those that just left the frame; for these particles the program will collect and store all the particle's information in a external database and after that eliminate the class instance of those particles.

For the particles for which we did not find a match, **and** for those with original position inside a particular region of the frame(the far right in Fig.3.15 we assume they are new particles coming into the frame and we create a new particle instance for it. Finally, we clear the vector of new incoming points before going into the next iteration. This is explained in Appendix H.

Some other considerations must be taken when tracking multiple particles. For example, if two or more particles collide during the tracking process the program will eliminate those class instances and will ignore those binary shapes in the foreground image. This must be done because when two particles collide or get too close to each other the program will not be able to make a proper differentiation.

3.3 Particle Identification

3.3.1 Predictors To Be Used

We will address the problem of particle recognition as an object classification among N possible known classes $(A_1, A_2, ..., A_N)$. In this particular application these classes refer to different types of cells. After a successfully detection and tracking of the flowing particles throughout the whole video sequence we are going to extract features from these objects/shapes in order to classify them. This information takes the form of a number of features $(X_1, X_2, ..., X_n)$. Here we refer to each individual feature X_i as **predictor**. We map the features into a n-dimensional feature space. The central objective is to get a set of predictors that is good enough so that the different classes $(A_1, A_2, ..., A_N)$ will map to clusters of feature vectors in the feature space. If these clusters can be separated by a hyper-plane then we say they are linearly separable. However, in most cases we need to make use of a hyper-surface. We will expand a bit more about this in section 3.3.2 when we introduce the pattern recognition algorithm we will be applying in our application. For now we will make a brief introduction to the several predictors we have chosen.

3.3.1.1 Colour Histogram Comparison

It is possible to extract specific features of a image by analysis of its colour histogram, which from now we will refer to as the 'histogram'. For example, in the Fig.3.9 we have a sample that contains red blood cells and protozoan blood born parasites called trypanosomes [33]. Using this figure, the histogram of different cell types was obtained.
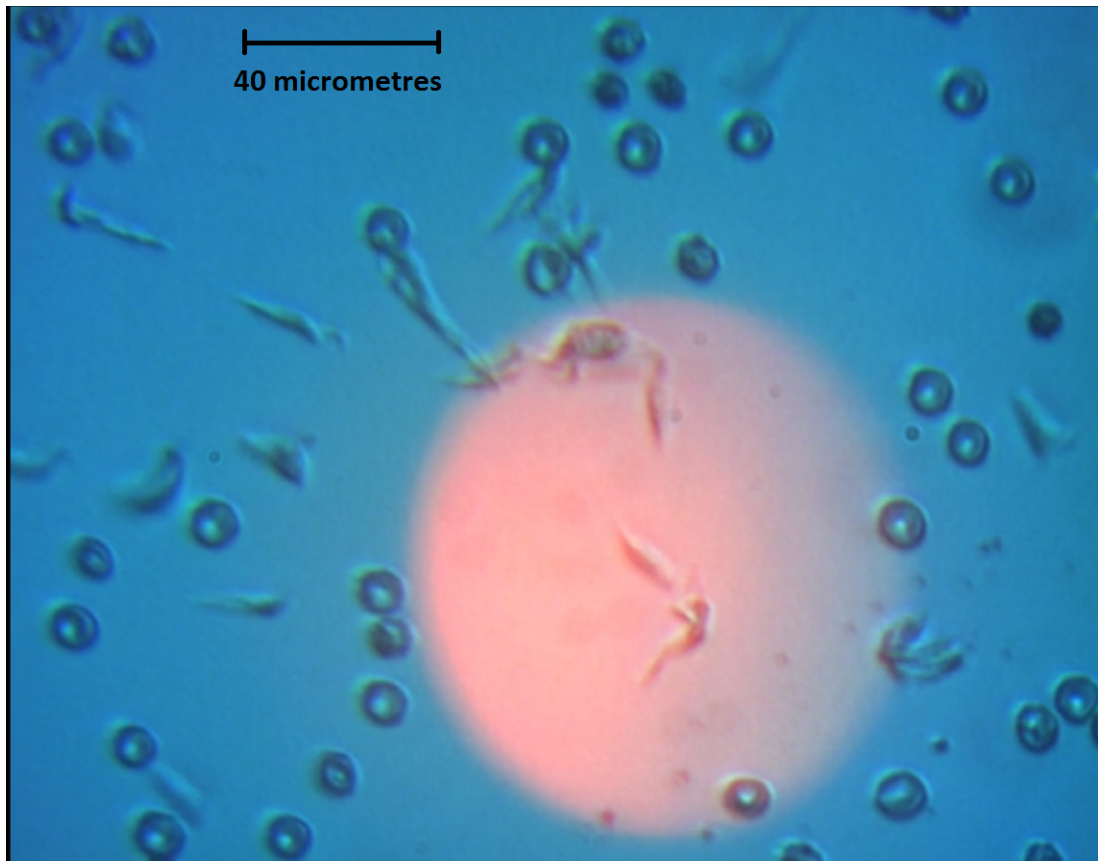
Figure 3.9: Image that was used to compute the histogram of red blood cells and trypanosoms [33].

The histograms for three different trypanosoms are shown in Fig.3.10 and the histograms for three different red blood cells are shown in Fig.3.11. It can be seen the histogram of trypanosoms is bi-modal and the histogram of red blood cells uni-modal. This represents the trypanosomes having many dark and light pixels but fewer intermediate values whereas the RBC have a preponderance of dark pixels; this kind of histogram information could be of great utility later on as a predictor. Histograms constitute an effective way to characterize an image's content. It has been extensively used in industrial applications because the information contained in a colour histogram is independent of the position and orientation of the object in the scene; which makes it a good predictor candidate in classification applications. For example, in Fig.3.10 and Fig.3.11 we can appreciate some qualitative differences in the shape of the histogram distribution for two different kinds of particles.

Since we have learned that histograms constitute an effective way to characterize an image's content, it seems promising to use histogram comparison for particle identification. The idea here is to measure the similarity between two images by simply comparing their histograms. In order to use it for bio-particle identification we will compute the histogram of all the particles currently being tracked and compare them with a histogram prototype

(a) Trypanosoma 1   (b) Thypanosoma 2   (c) Thypanosoma 3
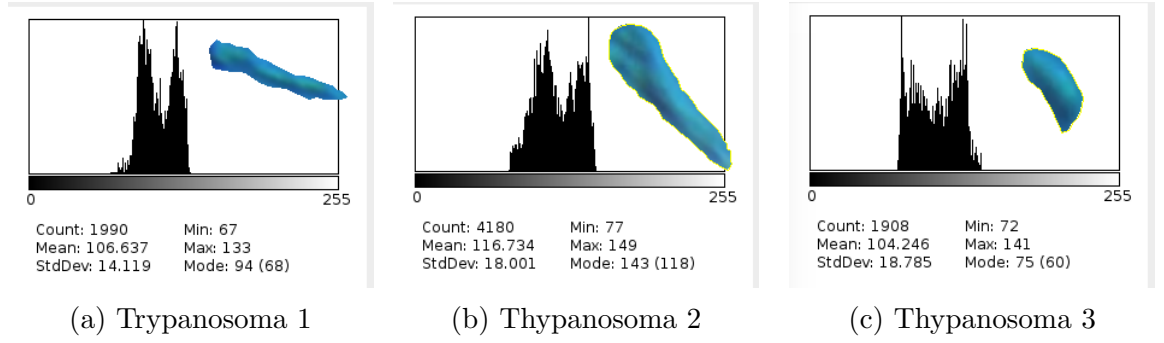
Figure 3.10: 1D histogram of three different trypanosoms cells.

(a) Red blood cell 1   (b) Red blood cell 2   (c) Red blood cell 3
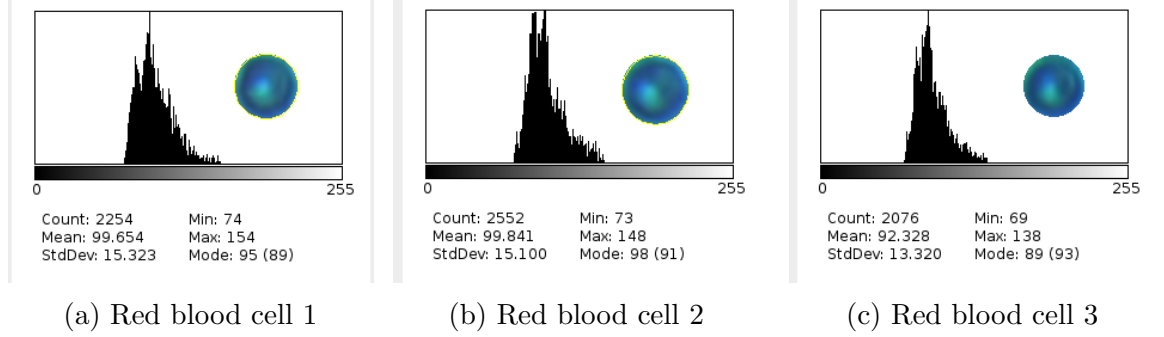
Figure 3.11: 1D histogram of three different red blood cells.

of the particle we are looking for. A measurement function(metric) that will estimate how different, or how similar, two histograms are will be needed. There are a number of metrics that could be used to compare histograms [62]. One of these metrics is the intersection method which simply compares, for each bin, the two values in each histogram and keeps the minimum one. The similarity measure, then, is the sum of these minimum values. Another possibility is to use the Chi-Square measure which sums the normalized square difference between the bins. Another of the metrics is the Bhattacharyya measure, which is used in statistics to estimate the similarity between two probabilistic distributions. The particular suitability of each one of these metrics depends on the particular application. In subsection 3.4.2 we apply these three metrics to the comparison of color histograms of bio-particles of different kinds in order to investigate if it is possible to make particle differentiation.

$$D_{\text{Correlation}}(h_1, h_2) = \frac{\sum_i (h_1(i) - \overline{h_1})(h_2(i) - \overline{h_2})}{\sqrt{\sum_i (h_1(i) - \overline{h_1})^2 \sum_i (h_2(i) - \overline{h_2})^2}} \tag{3.6}$$

$$D_{\text{Chi-Square}}(h_1, h_2) = \sum_i \frac{(h_1(i) - h_2(i))^2}{(h_1(i) + h_2(i))} \tag{3.7}$$

$$D_{\text{Bhattacharyya}}(h_1, h_2) = \sqrt{1 - \frac{1}{\sqrt{\overline{h_1 h_2} N^2}} \sum_i \sqrt{h_1(i) h_2(i)}} \tag{3.8}$$

where $\overline{h_k} = \frac{\sum_i (h_K(i))}{N}$ and N is the number of bins in the histogram h

3.3.1.2 Area Comparison

This predictor is used to make a differentiation between different kinds of particles based in the particle's apparent size. To compute the area of a shape we must just count the number of pixels on that particular shape. As explained previously, the area of a shape is given by the raw moment $\mu_{0,0}$:

$$Area = \mu_{0,0} = \sum_x \sum_y I(x, y) \tag{3.9}$$

In our actual implementation we compute area through the use of a data structure which is returned by the **cv:moments** function.

3.3.1.3 Moments and Moment Invariants

As we have learned in previous sections, moments can be used to measure a particle's area and its position in a frame. However, moments can be used for much more than that. Here we will use it as features in statistical pattern recognition. We previously defined the *raw moments*:

$$M_{i,j} = \sum_x \sum_y x^i y^j I(x, y) \tag{3.10}$$

From here we can derive the central moments $\mu_{p,q}$ which are *invariant to translations* [67].

$$
\begin{aligned}
&\mu_{0,0} = M_{0,0} \ \mu_{0,1} = 0 \ \mu_{1,0} = 0 \\
&\mu_{1,1} = M_{1,1} - \frac{M_{1,0}M_{0,1}}{M_{0,0}} \\
&\mu_{2,0} = M_{2,0} - \frac{M_{1,0}M_{1,0}}{M_{0,0}} \\
&\mu_{0,2} = M_{0,2} - \frac{M_{0,1}M_{0,1}}{M_{0,0}} \\
&\mu_{2,1} = M_{2,1} - \frac{2M_{1,0}M_{1,1}}{M_{0,0}} - \frac{M_{0,1}M_{2,0}}{M_{0,0}} - \frac{2M_{1,0}M_{1,0}M_{0,1}}{M_{0,0}M_{0,0}} \\
&\mu_{0,3} = M_{0,3} - \frac{3M_{0,1}M_{0,2}}{M_{0,0}} + \frac{2M_{0,1}M_{0,1}M_{0,1}}{M_{0,0}M_{0,0}} \\
&\mu_{1,2} = M_{2,1} - \frac{2M_{0,1}M_{1,1}}{M_{0,0}} - \frac{M_{1,0}M_{0,2}}{M_{0,0}} + \frac{2M_{1,0}M_{0,1}M_{0,1}}{M_{0,0}M_{0,0}} \\
&\mu_{3,0} = M_{3,0} - \frac{3M_{1,0}M_{2,0}}{M_{0,0}} + \frac{2M_{1,0}M_{1,0}M_{1,0}}{M_{0,0}M_{0,0}}
\end{aligned}
\tag{3.11}
$$

From these central moments we can compute *scale invariant moments* through the following transformation:

$$\eta_{xy} = \frac{\mu_{xy}}{\mu_{00}}^{1+\frac{x+y}{2}} \tag{3.12}$$

Finally, from these scale invariant moments we can derive moment invariants which are *invariant to translation, scale and rotation* [68].

$$
\begin{aligned}
I_1 &= \eta_{20} + \eta_{02} \\
I_2 &= (\eta_{20} - \eta_{02})^2 + 4(\eta_{11})^2 \\
I_3 &= (\eta_{30} - 3\eta_{12})^2 + (3\eta_{21} - \eta_{03})^2 \\
I_4 &= (\eta_{30} + \eta_{12})^2 + (\eta_{21} + \eta_{03})^2 \\
I_5 &= (\eta_{30} - 3\eta_{12})(\eta_{30} + \eta_{12})((\eta_{30} + \eta_{12})^2 - 3(\eta_{21} + \eta_{03})^2) \\
&\quad + (3\eta_{21} - \eta_{03})(\eta_{21} + \eta_{03})(3(\eta_{30} + \eta_{12})^2 - (\eta_{21} + \eta_{03})^2) \\
I_6 &= (\eta_{20} - \eta_{02})((\eta_{30} + \eta_{12})^2 - (\eta_{21} + \eta_{03})^2) \\
&\quad + 4\eta_{11}(\eta_{30} + \eta_{12})(\eta_{21} + \eta_{03}) \\
I_7 &= (3\eta_{21} - \eta_{03})(\eta_{30} + \eta_{12})((\eta_{30} + \eta_{12})^2 - 3(\eta_{21} + \eta_{03})^2) \\
&\quad + (\eta_{30} - 3\eta_{12})(\eta_{21} + \eta_{03})(3(\eta_{30} + \eta_{12})^2 - (\eta_{21} + \eta_{03})^2)
\end{aligned}
\tag{3.13}
$$

These moments have a specific name, they are called Hu moments. These moment invariants have proven to be very useful for visual pattern recognition. Together all these values represent a compact and robust description of the shape of an object. The central moments and moment invariants(Hu moments) can be computed from a particle's contour using the following instructions:

```
Moments contour_moments;
double hu_moments[7];
contour_moments = moments( contours[contour_number] );
HuMoments( contour_moments, hu_moments );
```

3.3.1.4 Perimeter Length

This predictor is an estimation of the length of the contour of a particle's shape; as long as the points are all neighbors along the contour.

```
// compute perimeter
int perimeter;
perimeter = contour.size();
```

3.3.1.5 Length to Width Ratio for the Minimum Bounding Rectangle

The length to width ratio is the length divided by the width of the minimum bounding rectangle. Here the minimum bounding rectangle is defined as the smallest rectangle which will enclose the entire shape. This predictor provides a useful metric to discriminate particles by shape. The actual implementation is done by using an algorithm that computes the minimum rectangle in all possible orientations.

```
// get the length to with ratio of the minimum bounding rectangle
RotatedRect minBoundingRectangle = minAreaRect(contours[contour_number]);
lengthWidthRatio = (float)minBoundingRectangle.size.width/(float)
    minBoundingRectangle.size.width;
```

3.3.1.6 Rectangularity

The rectangularity of a particle's shape is the ratio between the region's area and the area of the minimum bounding rectangle.

```
// get the rectangularity of a shape which is the ratio of the region area
    and the area of the minimum bounding rectangle.
int areaRectangle = minBoundingRectangle.size.height * minBoundingRectangle.
    size.width;
float rectangularity = (float)contourArea(contours[contour_number]) / (float
    )areaRectangle;
```

3.3.2 Particle Classification

After segmenting all the frames and computing all the predictors for each particle, we now need to reliably identify the particles we are looking for. For this work we have approached bio-particle recognition as a classification problem. We make use of one of the basic Machine Learning techniques: Support Vector Machine (SVM) with a novel combination of particle's colour histogram, size and shape as predictors.

A Support Vector Machine (SMV) is a pattern recognition algorithm that is part of a family of supervised-learning algorithms that were originally designed for binary classification. The term *supervised learning* refers to a machine-learning algorithm that learns through the use of labeled data. Before using our particle detection application we

need to train the algorithm with an amount of data that is properly labeled; which means each data set needs to a have a class.

Before doing any classification it is necessary to train the system. This should be done with a different data set to the one we plan to use for actual classification. Also, this step requires a sufficient amount of labeled data. There is no clear answer to how much training data is needed to achieve good predictive performance. The right amount of training data must be discovered through empirical investigation. For the training of our computer vision application, we used a group of digital images containing 1654 particles obtained from a buffy-coat e.g. a diluted blood sample with an increased concentration of white blood cells(WBCs). The group of labelled data for training included white blood cells(WBCs), red blood cells(RBCs), platelets, debris and clusters of particles. For our case the acquisition of labelled data is a complex and time-consuming process; this was probably the main restriction we had to face during the training process. Even though the results obtained using this training dataset were satisfactory we believe that more investigation is needed to properly capture the relationship that may exist both between input features and output features, we will discuss more about this in section 5.1.

3.3.2.1 Support Vector Machine (SVM)

(a) Separating lines   (b) Optimal hyperplane
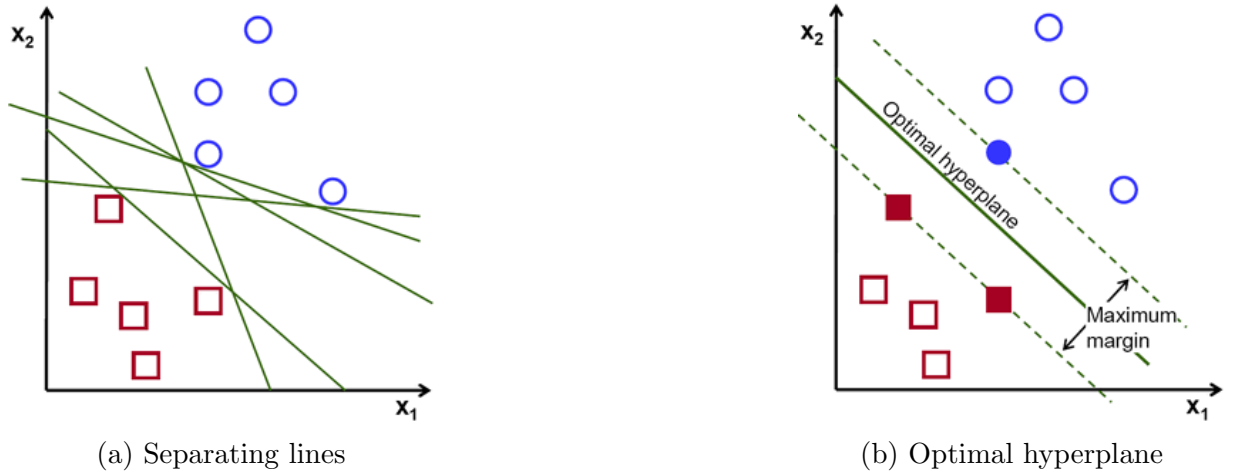
Figure 3.12: Maximum margin classifier. a) In two dimensions a hyperplane is represented as a line. Support vector machines(SVM) attempt to determine the optimal hyperplane to separate the different classes; however, there is an infinite number of possibilities(green lines). The way SVM defines the optimal hyperplane is through computing the minimum distance from support vectors. b) The optimal separation hyperplane maximizes the margin of the training data. Source: opencv.org [58].

Support vector machines [59, 69] provide a mechanism to attempt determining the optimal hyperplane to separate classes, see Fig.3.12. In a few words, by making a proper selection of N predictors $(X_1, X_2, ..., X_N)$ we attempt to classify clusters of vectors $\overline{X} = (X_1, X_2, ..., X_N)$ in a hyperspace of N dimensions through the optimal hyper-plane

or hyper-surface. This hyperplane/hypersurface is placed at a minimum distance from the *support vectors*; which are the instances of the various classes which are closest to the classification boundaries, see Fig3.12.

The technique used for the computation of the optimal hyperplane is called *maximum-margin hyperplane algorithm* and it was originally introduced by V. Vapnik in 1963 [70]. The optimal hyperplane can be represented in a infinite number of ways by scaling α and α_0. The representation we will use is the so called **canonical hyperplane**:

$$\mid \alpha_0 + \alpha^T x \mid = 1 \tag{3.14}$$

where x symbolizes the training examples closest to the hyperplane. The training examples closest to the hyperplane are called **support vectors**.

The distance between a point x and a hyperplane (α, α_0) is given by:

$$distance = \frac{\mid \alpha_0 + \alpha^T x \mid}{\parallel \alpha \parallel} = \frac{1}{\parallel \alpha \parallel} \tag{3.15}$$

The margin M is twice the distance to the closest examples:

$$M = \frac{2}{\parallel \alpha \parallel} \tag{3.16}$$

It all comes to maximizing M subject to some constrains. The constrains model the requirement for the hyperplane to classify correctly all the training examples x_i.

Formally, this could be represented as:

$$\min_{\alpha, \alpha_0} L(\alpha) = \frac{1}{2} \parallel \alpha \parallel^2 \tag{3.17}$$

subject to:

$$y_i(\alpha^T x_i + \alpha_0) \geq 1 \forall i \tag{3.18}$$

where y_i represents the labels of the training examples. This is a Lagrangian optimization problem, and can be solved using Lagrange multipliers to obtain the weight vector α and the bias α_0 of the optimal hyperplane.

3.3.2.2   Non-linear Classification (SVM)

Most real computer vision applications of SVM require a more powerful tool that the linear classifier previously introduced. Here we introduce the *Kernel Trick* commonly used to improve classification results when applying SVM to data that is non-linearly separable.

INPUT SPACE   **FEATURE SPACE**
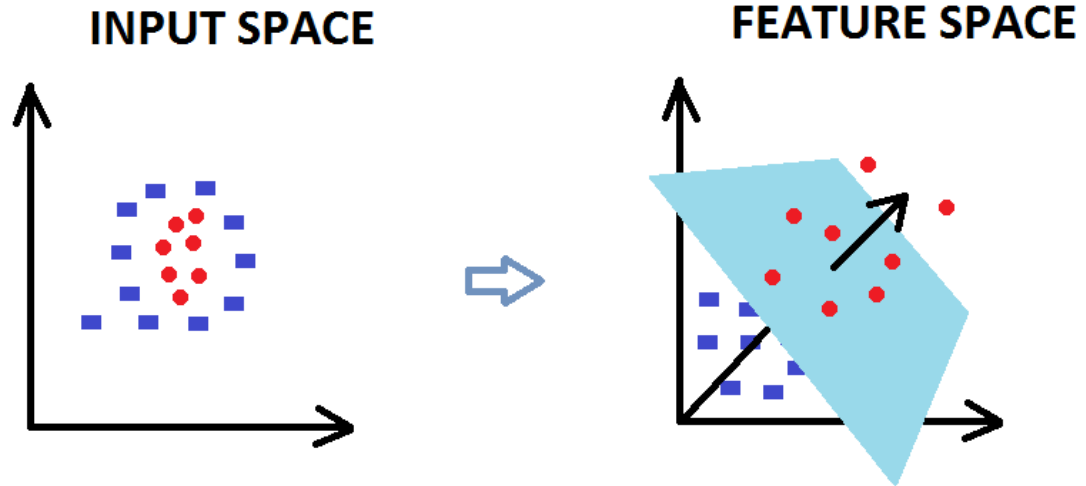
Figure 3.13: Objects of different classes (shown by dots of different shapes) mapped into 2D feature space. On the left, the classes are not linearly separable. After mapping the data using a kernel function the classes become separable and hyper-surface (or a hyper-curve) is shown between them.

This algorithm for non-linear classifiers was originally introduced by Boser et al [71] in 1992.

When dealing with non-linear datasets a kernel trick is used for aiding in the classification. Groups of vectors $\overline{X} = (X_1, X_2, ..., X_N)$ which are not *linearly separable* in the original space may be separable in a higher dimensional space. In this technique the dot products are defined in term of the *kernel function* $k(x, y)$ in such a way that the hyperplanes in the higher dimensional space are defined as a set of points whose dot product with a vector in that space is constant.

$$\sum_n \alpha k(x_i, x) = constant \tag{3.19}$$

In a few words, it works by mapping data points into a higher dimensional feature space using a *kernel function*. The whole point in doing this is to improve the separation of classes, see Fig. 3.13

Unfortunately, choosing the "right" kernel is not easy because it depends of the particular needs of the application and is mostly done following a trial and error methodology. In addition to this, we also needed to tune the kernel parameters in order to achieve good performance in our classifier application. Here we have chosen to implement the Radial Basis Function(RBF) kernel; which is a kernel in the form of a Gaussian function.

A kernel is a function of the form:

$$K(\mathbf{X}, \mathbf{X}') = \langle \phi(\mathbf{X}, \mathbf{X}'), \phi(\mathbf{X}, \mathbf{X}') \rangle \tag{3.20}$$

where ϕ is a function that projects a vector $\mathbf{X}$ into a new vector space. The RBF kernel projects vectors in to a infinite dimensional space.

$$k(x, y) = exp(\frac{\parallel x - y \parallel^2}{\sigma^2}) \tag{3.21}$$

3.4 Results and Discussion

3.4.1 Multiple Particle Tracking

We successfully developed a computer vision application in C++ using the OpenCV library. The program can simultaneously track many micron-size particles using standard optical microscopy(bright field microscopy). We only use a basic upright microscope (Olympus BX51), along with the appropriate lighting equipment and a digital camera (Hamamatsu C11440) connected to a computer to store and process sequences of images. We don't use any other techniques to enhance cell contrast e.g. selective dyes. The video analysis can be made in real time or with the use of pre-recorded videos.

In Fig.3.14 we have four snapshots taken at random points during a video sequence. Here our software is tracking all the particles in a mixture of 10 and 20m-diameter beads flowing from top to bottom. The used acquisition frame rate for all these experiments was 20 frames/second. The polystyrene beads are suspended in distilled water, which flows in our microfluidic channel at a flow rate of 0.5μL/min. The rectangular shape of the frame is in order to cover most of the width of our microfluidic channel.

As mentioned previously, the first step is to generate a good quality background model, which is done automatically using the first ten frames in the video sequence. Subsequently, the program proceeds to run the multi-tracking algorithm. Each particle is treated as an independent entity; which has it own identification number(ID), characteristics(the complete set of predictors), and position in each frame.

The purpose of Fig.3.14 is to illustrate how our computer vision application behaves during a few of the most common situations. In Fig.3.14a we have the first two particles appearing in the video sequence after setting up the background model is completed. The software automatically computes the position and characteristics(predictors) of these new particles instances as they move through the frame. As we can see in the figure, the centroid of the particle is marked with a small colored circle next to the identification number, which starts at zero. In Fig.3.14b we have the simplest of cases in which a single

(a)

(b)

(c)

(d)
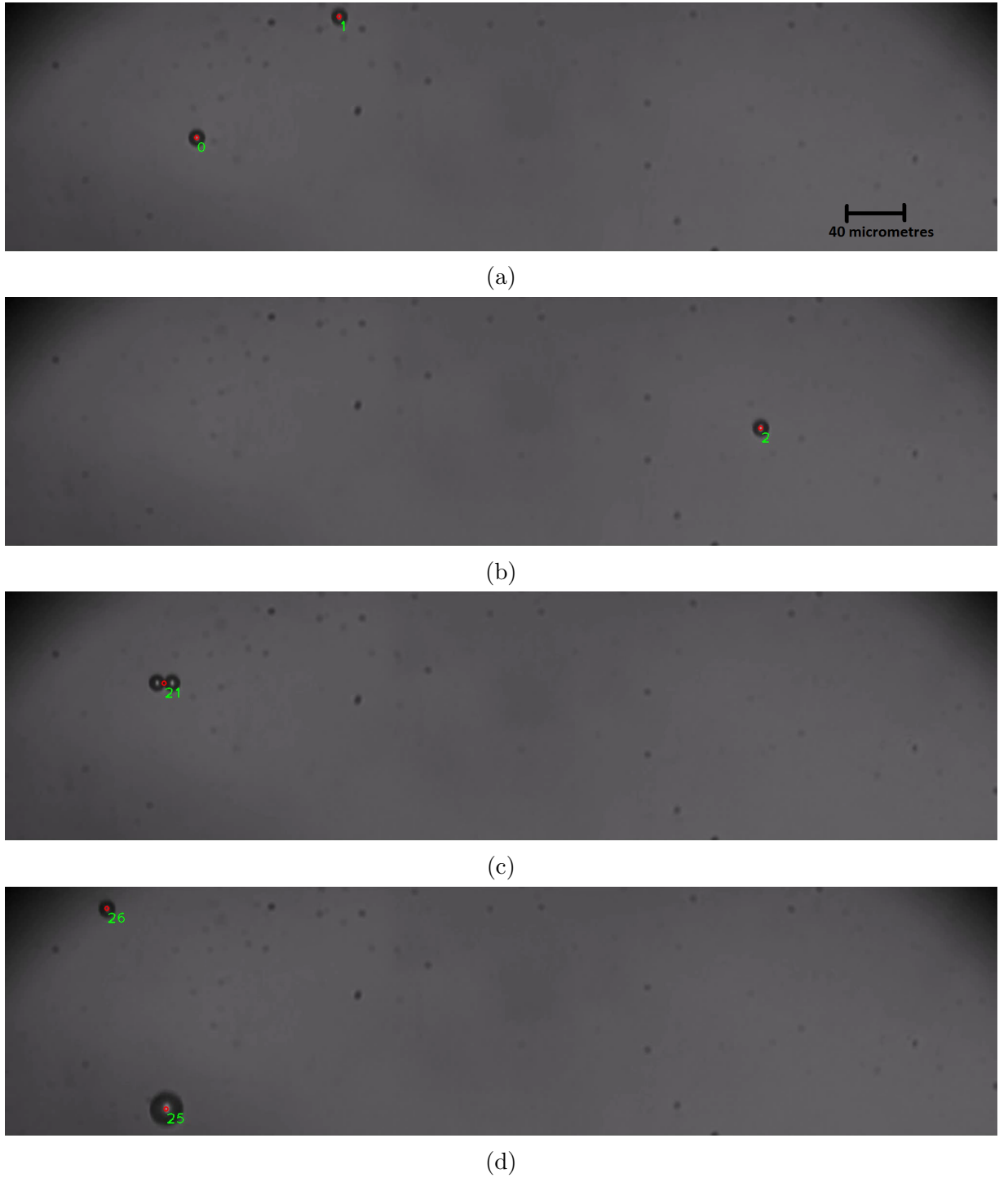
Figure 3.14: A few snapshots taken at random points during the particle multi-tracking of 10 and 20μm-diameter polystyrene beads. In the video sequence, particles flow from top to bottom at a flow rate of 0.5μL/min. These snapshots are intended to illustrate a few of the common scenarios: a) the first two particles flowing simultaneously, the assigned ID numbers are 0 and 1 respectively. b) A single particle flowing down the stream; the most simple case. c) A cluster of two particles; which at this point our system recognizes as a single particle. d) Two particles of different size in the shame frame; our system has no problem making the tracking and differentiation.

particles flows through the frame. The next case, see Fig.3.14c, corresponds to a cluster of two particles moving through the frame; in this situation it is interesting to notice that the computed centroid is right in between the two particles. At this point the computer is unable to differentiate between a single particle and a cluster. We must remember that at this stage the system is collecting information of *all* detected particles. In later steps, when all particles in the video sequence have been detected, the system will proceed to apply a machine learning algorithm to properly identify our target particles from a mixture of particles that includes clusters and debris. At this stage, the system will treat this cluster as an individual particle. It is also worth mentioning that this case could be considered as a failure of our segmentation algorithm; we could argue that by better adjusting the parameters used for background subtraction and image segmentation we could overcome situations like this one. However, we propose that this is not the right way to approach these kinds of situations because the big number of particles the system detects through the whole video sequence gives us a countless number of variations and possibilities that it becomes impossible to cover them all by just changing a few settings. The best way to deal with this is to properly train our system with as many labeled examples of our target particle as possible. Finally, in Fig.3.14d, we have two particles of different kind(10 and 20μm-diameter) moving throughout the frame simultaneously. This situation does not really represent a challenge because as we will see in a later section the chosen set of predictors can easily handle particles of the same material but different size.

In Fig.3.15 we have a situation that is a bit different. These particles are 20 μm-diameter particles suspended in DI water flowing in a glass capillary tube. This time the diameter of the capillarity tube is too wide to focus on the particles. However, regardless of this, our program is still good at particle detection and tracking. When we say that our application performs well we are referring to the capacity our software has to effectively locate and simultaneously track the flowing beads in a microfluidic channel or capillary tube even for non-ideal conditions of contrast and/or a changing background. All the flowing particles are localized and simultaneously tracked as they flow from right to left. In this figure we can see the ID number assigned to each particle as they flow from right to left. Our algorithm performs well even under challenging conditions. For instance, low contrast between foreground and background like the situation we have in Fig.3.15, or with a substrate that contains a considerable amount of particles and debris attached to the substrate, see Fig.3.14d.

These results allows us to highlight two of the main strengths of our algorithm. The first one is our dynamic background model that is able to incorporate changes. The implementation of a Gaussian Mixture Model for background subtraction seems to be the ideal choice for moving micro-particle detection using video microscopy. Another distinctive characteristic of our algorithm is the method we use for the simultaneous tracking of particles, which it is simple but at the same time effective. The usual

approach to object tracking uses a group of special points or features in the object, the so called **key points**, i.e. Harris corners [58], which look at the average change in directional intensity in a small window around a possible interest point. In this kind of techniques the central idea is to select special points; features that are unique and stable in the image and perform local analysis on them. These kinds of techniques can perform well as long as there is enough of such points and they are unique and stable features that can be accurately localized over a video sequence. This approach, however, is not the ideal fit for our needs because we have objects(particles) that experience changes in image contrast, orientation and viewpoint. In this work we have followed a different approach. Instead of looking at an object of interest as a collection of special points, we see it as a *rigid object* who has identity, characteristics and position. Based on this, we implement a efficient tracking mechanism based on the tracing of each particle's centroid on every frame in the video sequence.

The computation of individual trajectories, velocities and accelerations is now straightforward; this is because we have access to the ID and position of all successfully tracked particles at all times.
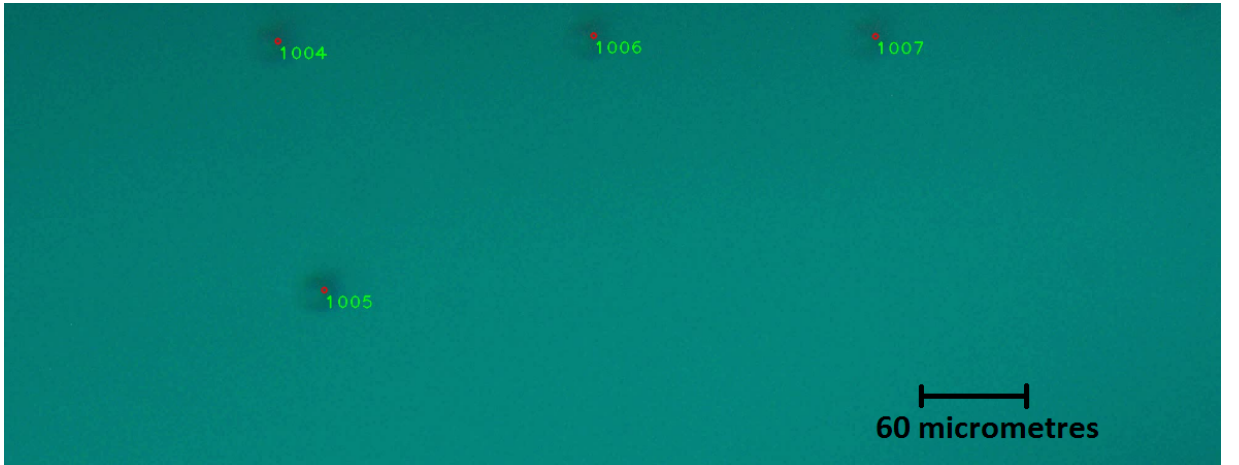
Figure 3.15: Polystyrene particles(20μm-diameter) flowing in a capillarity tube; this is a single frame from the output video. The program successfully tracks the centroid of a group of particles as they move through a frame even though the contrast of the image is nonideal. In colour, we can see the particle's centroid and the ID number assigned to each particle as they flow from right to left. The tracking capability of our software is particularly important for the automatic counting of particles. The multitracking capability is also useful for the differentiation between particles as they move together throughout a frame, which requires being able to reliably identify the position of each particle in each successive frame.
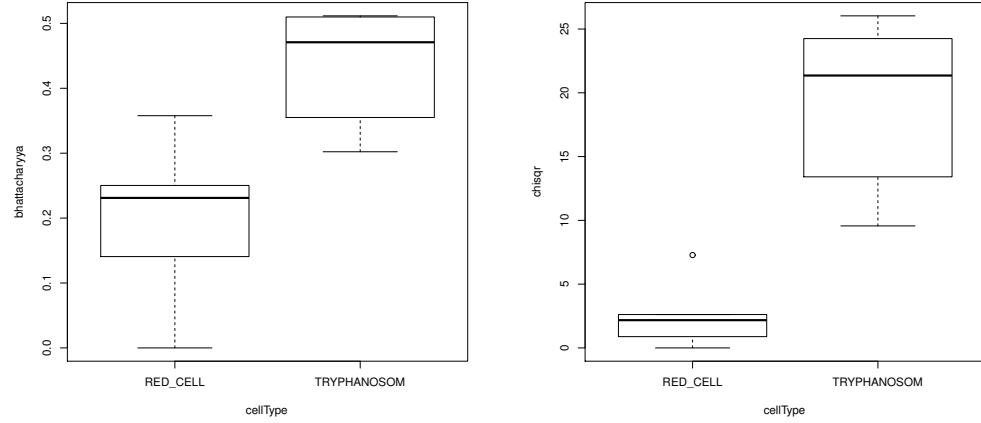
(a) Bhattacharyya metric

(b) Chi-Square metric
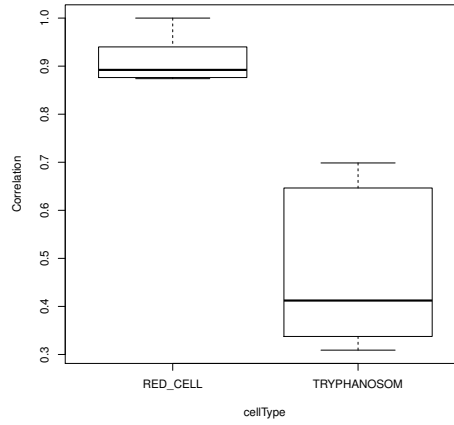
(c) Correlation metric

Figure 3.16: Matching scores obtained from the comparison of colour histograms derived from images of trypanosomes and red blood cells. Three different metrics where applied: Bhattacharyya, Chi-Square, and Correlation. A reference image (single red blood cell) was compared against ten randomly selected red blood cells images and ten trypanosome images. For the Bhattacharyya and Chi-Square metrics, the lower the score the best matching we have with our reference image. On the other hand, for the Correlation metric, a higher score means a better matching to our reference image. We can observe that for all these three metrics our reference image(red blood cell) has a colour histogram that is more similar to other red blood cells that to Trypanosoma cells. The relatively high degree of differentiation achieved for each metric(especially for the correlation metric) suggests histogram comparison could make a good predictor for cell classification.

3.4.2   Color Histogram and Particle's Size as Predictors

In Section 3.3.2 we suggested to approach the challenge of particle detection as a classification problem. In this subsection we will try to determine the value of histogram and area comparison as predictors in a more quantitative way. In doing this we will also measure/study the capabilities of our tracking algorithm.

Lets start with histogram comparison. As mentioned previously, this is intended to be one of the continuous predictors; however, a metric must be defined first. In Fig. 3.16 we compare a single reference image(red blood cell) against ten randomly selected red blood cells and ten trypanosoms. Three different metrics were selected: Bhattacharyya, Chi-Square, and Correlation, see Eqs.3.6, 3.7, and 3.8. For these examples we have used a 1-channel gray level image, where each pixel has a value of between zero(black) and 255(white).
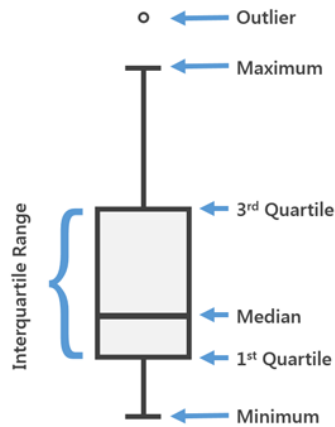
Figure 3.17: Box plot showing five key values of a distribution: minimum, firt quartile, median, third quartile, and maximum. Source: https://pro.arcgis.com.

In order to visualize and compare the different distributions obtained for the three different metrics, we are expressing our results in a box and whisker plot. A box plot allows us to easily visualize five key values of each distribution: minimum, first quartile, median, third quartile, and maximum, see Fig.3.17. As we can see from the results shown in Fig.3.16, there are no boxes overlap for any of the three metrics: Bhattacharyya, Correlation, and Chi-Square. We must remember that our reference image is a red blood cell and each one of the three figure represents the correlation scores for a group of red blood cells and a group of Trypanosome cells. In the results obtained for the Bhattacharyya metric, for instance, we have two groups corresponding to red blood cells and trypanosomes respectively. For the particular case of the Bhattacharyya metric, the higher the score the worst the matching correlation actually is. In Fig.3.16a we can see that the third quartile of the red blood cell distribution is lower than the first quartile of the Trypanosoma distribution, so there is a fundamental difference between the two groups regarding the matching score levels. The Trypanosoma group has a greater score than the red blood cell group. In other words, red blood cells are a better match for our reference image(red blood cell). Please note that the difference in matching scores is even greater for the Correlation and Chi-Square metrics; there is a relatively high degree of differentiation, especially for the correlation metric. These findings suggest that histogram comparison could make a reliable predictor in our SVM algorithm. The distribution of pixel values across an image constitute an important characteristic of that image and it seems to have value as a pre-
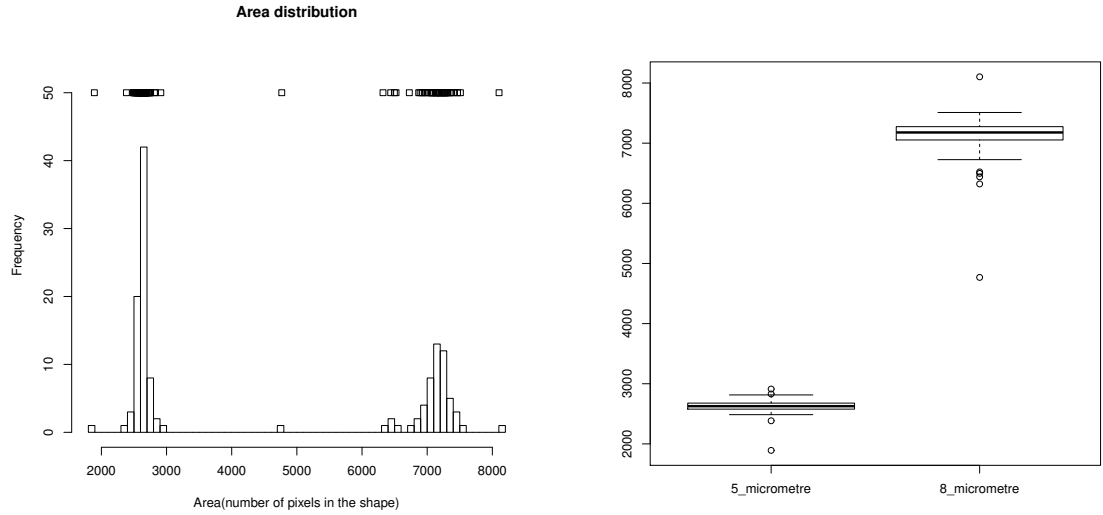
(a) Size histogram for a binary mixture of particles: 5 and 8 micrometre diameter beads.

(b) Area distribution for the two components in the mixture.

Figure 3.18: To test the value of area(number of pixels in the shape) as a predictor, we also computed the area of each particle in a mixture(5 and 8 micrometer in diameter beads) flowing in a microfluidic channel. As we can see, the two area distributions are very well defined. This unsurprisingly suggests the number of pixels in a shape could be useful as a predictor.

dictor in the discrimination between cells. Please note that we do not/should not expect a particular metric to be perfect as a predictor; otherwise, we would not need to make use of a machine learning algorithm in the first place. In a real application, we would expect to have a more noisy and difficult environment in which the differentiation will be a bit more challenging. As we can see from these results each one of these three metrics offers some valueble for cell discrimination, this is why we have chosen to use ***all three metrics*** as predictors. A properly trained SMV algorithm with a good quality set of predictors will give us the best prediction that can be made from the evidence supplied.

For testing the relative merit of particle size as a predictor we used our multiple-particle tracker program to compute the area of each particle in a mixture of polystyrene beads. We are defining *area* as the number of pixels in a particle's shape; which is computed using Eq.3.9. The sample is composed of beads of 5 and 8 μm in diameter. In Fig.3.18a and b we have the size histogram and size distribution respectively. As we can observe from these results, we can perfectly differentiate between these two size distributions as they are very well defined. This suggest the number of pixels in a shape could make a good second predictor for our application. Actually, this could arguably be one of the most reliable predictors we will have in our group for the identification of cell types of different size such as red blood cells and white blood cells; and also one of the easiest to compute. For particles of the same kind(size) we would expect the number of pixels in a shape to

(a) Size histogram for diluted blood sample.

(b) Feature space for two predictors: particle's size and perimeter, in diluted blood. The units for area and perimeter are pixels.
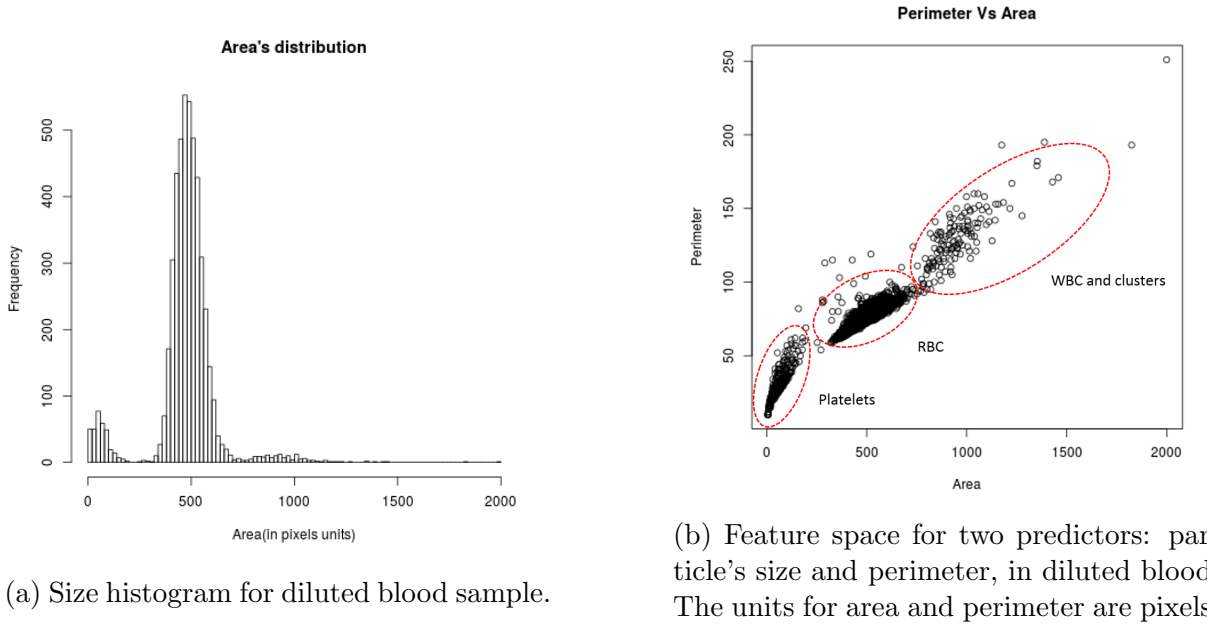
Figure 3.19: a) Particle's size histogram for whole blood diluted in PBS(0.25% v/v). The Gaussian distribution for platelets and red blood cells can be appreciated. b) 2D feature space for the same for the same sample using just two predictors: particle's size and particle's perimeter length, all in pixels units.

follows a standard distribution, also called bell curve, e.g. the diameter of the beads is not all the same; however, in spite of the different sizes of beads, the majority of the values are clustered around the mean value, with a few measurements to the right of this value and a few measurements to the left of this value. The resulting shape looks like a bell and is the shape that represents the normal distribution of the data. In the real world, no examples match this smooth curve perfectly, but many data plots, like our computed areas(pixels), are approximately normal. It seems reasonable to attribute the data point that is in-between the two distributions to a natural aberration to the normal size of beads.

In Fig.3.19 we have the results of a similar experiment, but this time we are analyzing blood cells instead of beads. A sample of whole blood diluted in PBS(0.25% v/v) was pumped through our device at a flow rate of 2μL/min, see Fig.3.5. As mentioned previously, our program gathers information about each cell as they move through the frame, from top to bottom; however, in this section we are only focusing on studying the relevance of a particle's size as a predictor. In Fig.3.19a we have the size histogram of all the particles detected in that particular video sequence.

As we can see, just like the previous results with beads, this time we also have size distributions that seems to be well defined. It is possible to make an easy distinction between the different types of cells based on size(pixel units). Here when we say that our distributions are well-defined we refer to the fact that the mean of our three subpopulations

are sufficiently separated, see Fig. 3.19a. To be more specific, the mean values μ of two consecutive distributions are separated by at least twice the maximum standard deviation, so $\mid \mu_1 - \mu_2 \mid > 2\sigma_{max}$. First we have platelets; these are the second most common type of blood cells in our sample, in Fig.3.19a it corresponds to the first distribution into the left. The second distribution towards the right corresponds to red blood cells, which are by far the most numerous type of cells in our sample. The third distribution into the far right corresponds to a combination of white blood cells and clusters of red blood cells; this group corresponds to the smallest number of particles in the whole sample.

In addition to the particle's size histogram we also have a simple 2D feature space for two predictors: particle's size and particle's perimeter; in this space each point corresponds to an individual particle. One of the purposes of this is to illustrate an example of a two dimensional feature space. In Fig.3.19b we have only two dimensions, corresponding to the perimeter and area of all particles in the video sequence. It is interesting to notice that we still have a good differentiation of our three distributions: platelets in the bottom left; RBC, which we can easily identify as the darkest(densest) group of points; and finally a combination of WBCs and RBC clusters, which corresponds to the lightest group of points in the top right of the graph.

Based on the results we have obtained so far we believe the particle's color histogram and particle's size can be successfully applied for the fast and efficient classification of micro-particles using normal microscopy and without the use of any kind of bio-marker or any other method to physically enhance image contrast in the video scene. However, it is important to mention that non of this would be possible without our approach to foreground subtraction, image segmentation, and multi-particle tracking. All of which has been implemented in a fast and efficient C++ framework. We also realized that there is no reason limiting ourselves to just these four predictors: three metrics for histogram comparison and particle's size. we have decided to go one step further and also implement the selection of predictors introduced in section 3.3.1 in a SVM algorithm. Our final implementation includes the three metrics for histogram comparison, the seven moment invariants, particle's size, particle's perimeter length, the length to width ratio for the minimum bonding rectangle, and the rectangularity of a particle's shape as predictors. All this for a total of 14 predictors for image recognition. Before testing our computer vision application we trained our system using a different dataset containing images from a 'buffy-coat' e.g. a sample with an increased concentration of WBC that contained of a group of 14 white blood cells and 1640 non white blood cells, the later was a combination of red blood cells, platelets, debris and clusters of particles. Our testing dataset consists of a group of images for which we have made a visual inspection to corroborate that there were no target particles(WBC). In a similar way, the positively identified particles are visually inspected to determine if there are false positives. This process is simple because our application puts colour marks and identification numbers to all our positively identified

particles, see Fig.3.20.

When testing our system for the identification of our target particle(white blood cells), we found 100% positive classifications that are correct. For this example, the total number of processed frames was 657. The number of identified particles(WBC) was 18 from a total number of 5953 detected particles of all kinds and the processing time was 48884.5 ms or about 49 seconds.

In Fig.3.20 we have an example of the image retrieval step in which the system displays the results as a sequence of images containing the located WBC in a colored circle and indicating its identification number. After a visual inspection of the retrieved images, we corroborated there was no false positives in this results regardless a considerable number of debris and clusters.
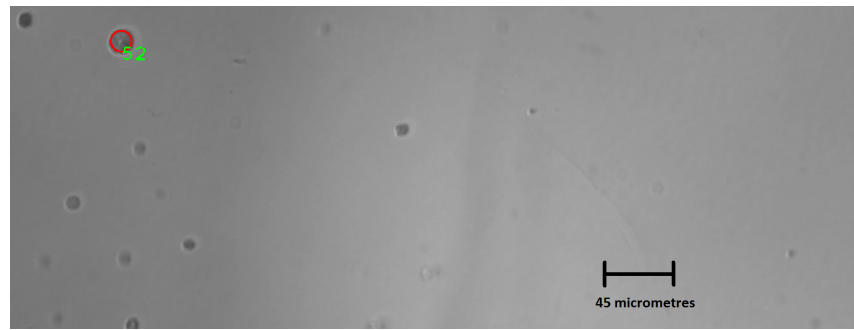
(a)
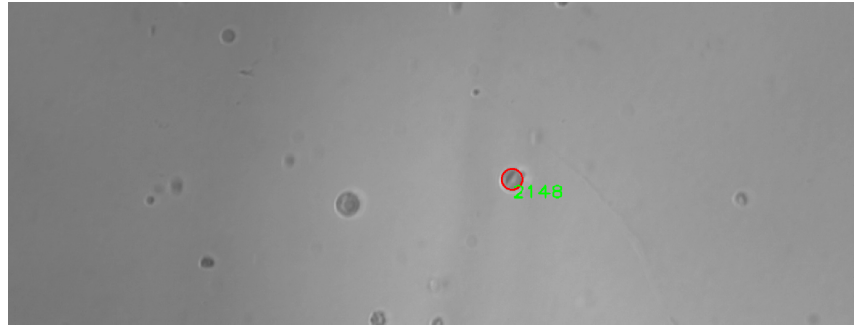
(b)
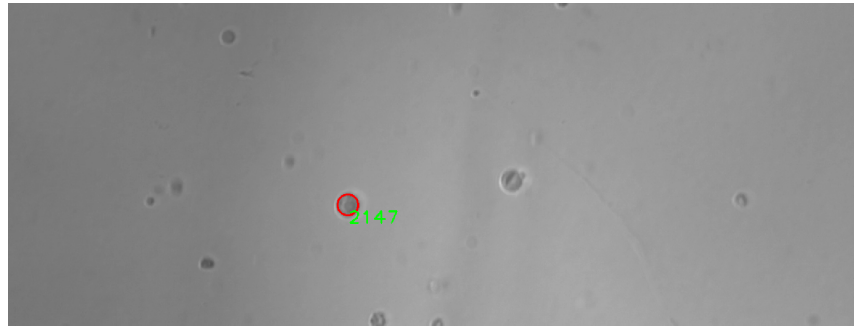
(c)
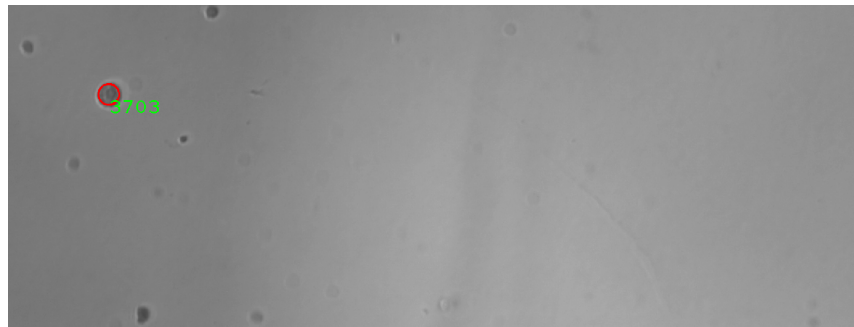
(d)

Figure 3.20: An instance of image retrieval for the identified white blood cells. The program locates and shows the detected WBC circling them in color and also displays their identification(ID) number.

Chapter 4

Tailoring the potential across a microfluidic channel for particle separation in a portable device

4.1 Introduction

The ability to isolate and enrich a specific type of micro particles from a heterogeneous sample is a very important requirement for biomedical applications and rare cell detection and identification. To this day several technologies have been developed for the manipulation and separation of micro particles in an aqueous solution. They are very different in nature as they apply different physical principles: optical, acoustic, hidrodynamic, magnetic and electrical methods, just to mention some of the most popular out there. Two of the most popular technologies for cell detection and separation are: Fluorescent-Activated Cell Sorting(FACS) [18, 19] and Magnetic-Activated Cell Sorting(MACS) [20, 21]. However, we will not consider this techniques in this work because they require the use of tags or labels.

One of the main goals of lab-on-a-chip(LOC) technologies is to develop a technique that is more versatile, user-friendly and compact; a system that is able to make spatial separation of multi-component mixtures under real conditions. This is one of the reasons LOC technology applied to the continuous separation of microparticles is becoming increasingly prevalent within the area of biology and medicine. Dielectrophoresis(DEP) is of particular interest for cell discrimination and isolation because the magnitude and direction of DEP forces are determined by the dielectric properties of the biological particle as well as the medium; which are frequency dependent.

At the beginning of my PhD studies, our interest was focused on applying optoelectronic tweezers for the manipulation of micro-particles in aqueous solutions in order to assess whether or not it is possible to adapt the technology to a portable device. The ex-
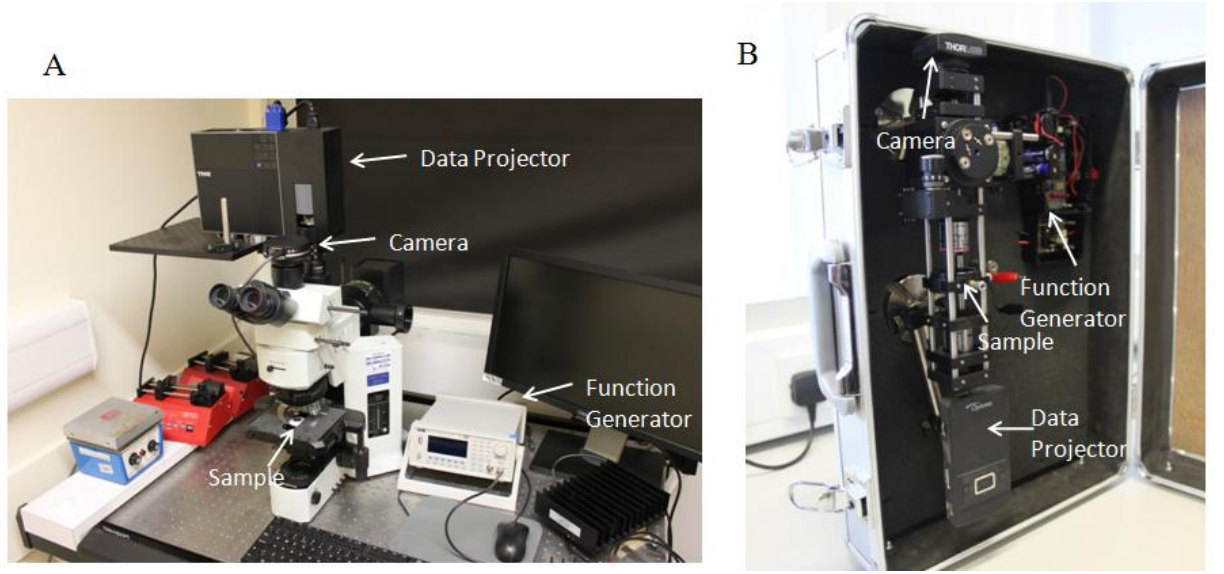
Figure 4.1: A) Conventional experimental setup for the OET experiment. B) Our portable version of the same setup; which incorporates all the elements in a briefcase and can be run with batteries.

perimental setup used for that purpose consisted of a upright microscope(Olympus BX51) and a data projector for the generation of light patterns(virtual electrodes) on the surface of amorphous silicon(a:Si); where the conductivity of the illuminated areas is increased by orders of magnitude. In Fig.4.1a we have a picture of this system indicating its main components: data projector, camera, function generator and sample.

The first step when trying to assess how effective OET force is for the manipulation of micro-particles is to measure the maximum velocities that are possible to reach in function of the medium's conductivity. For this purpose we developed a computer program that generates a circular frame that revolves on its axis, see Fig.4.2a. Using this technique individual polystyrene beads are forced to move in a uniformly accelerated circular motion. The equations of rotation(constant aceleration) are given by [72]:

$$\theta = \theta_0 t + \frac{1}{2}\alpha t^2$$
$$\omega^2 = \omega_0^2 + 2\alpha\theta$$
(4.1)

where θ, α and ω correspond to the angular displacement, angular acceleration and angular velocity respectively. Using Eq. 4.1 and the equation for the lineal velocity $V_T = R\omega$ of a particle moving in circle of radius R we obtain:

$$V_T = \alpha R t$$
(4.2)

this last relation is the one our software applies to compute the maximum linear velocity V_T the particles reach. The linear velocity of particles is increased slowly and steadily

<div align="center">(a)   (b)</div>
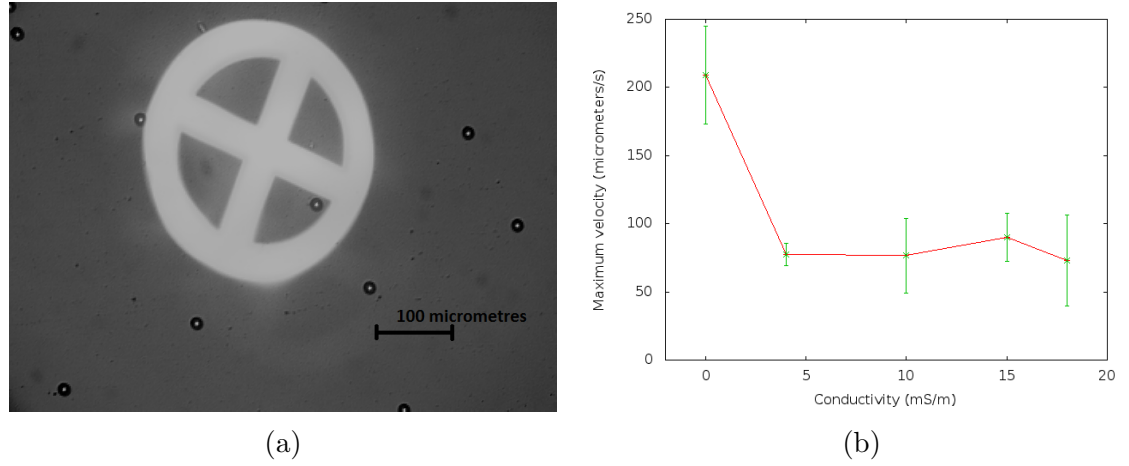
Figure 4.2: A) Individual polystyrene beads are forced to move in a uniformly accelerated circular motion. The liner velocity of particles is increased steadily until the OET force in unable to counteract the drag force. At this point the user stops the program and the software automatically calculates the maximum linear velocity reached and saves all relevant information into a file. B) The experimental results for attained using the Olympus setup for 15μm diameter bead and five different conductivities: 0.1mS/m (distilled water), 4mS/m, 10mS/m, 15mS/m and 18mS/m. The used voltage and frequency was 11kHz and 20Vpp respectively. The radio for the circular motion was 102.98μm.

until the applied OET force is unable to counteract the Stokes drag force; when this happends the program computes the maximum reached lineal velocity and saves all relevant information. The results obtained for the maximum velocity in function the conductivity of the suspending medium are shown in Fig.4.2b. Every point represents the mean value of five measurements and the error bar corresponds to the range of the obtained results for each conductivity. As we can see, there is a sharp drop in the maximum velocity from 0.1mS/m to 4mS/m and remains relatively steady all the way up to 18mS/m. The application of this technique to this kind of measurements turns out to be very useful, practical and reliable; However, one of the central goal of the whole project was to develop a portable system that allow the use of OET technology outside the laboratory. An important step towards this goal was made by S.L Neale et al [12]. They developed a portable optical micromanipulation setup based on Optoelectronic Tweezers. In Fig.4.1b we have a picture of the device. It uses a mini data projector(Dell M110) to generate the light patterns; which are focused through a 20X objective(Olympus, 0.4 N.A.) on the amorphous silicon substrate. The system contains a small battery powered function generator which is capable of producing a sinusoidal signal of up to 9Vpp in amplitude and up to 78kHz in frequency. All the components in this system are battery powered, except for the mini data projector which requires one power socket. This system performs well under controlled circumstances; the medium's conductivity must be carefully controlled in order to achieve a OET force that is strong enough to effectively move particles.
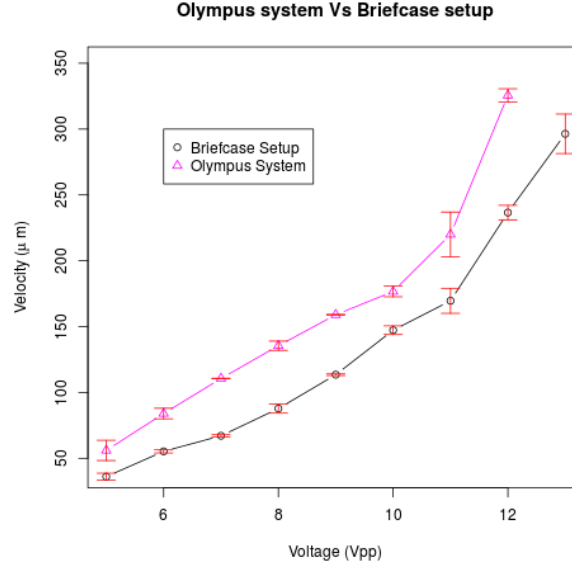
Figure 4.3: Comparison between the Olympus and Briefcase setup. We measured the maximum velocity attained for a range of voltages for the Olympus system and the Briefcase setup. For all this experiment we used 45μm-diameter polystyrene beads suspended on a medium with 0.1mS/m. The applied frequency was maintained constant at 20kHz.

An important step when investigating the performance of the technique on a portable device it to compare the conventional OET experimental setup, shown in Fig.4.1A with our portable version, Fig.4.1B. After using our program on both systems we obtained the results shown in Fig.4.3. The purpose of the experiment was to compare the maximum velocities obtained using our conventional OET setup with the ones obtained using our portable version. The selected conductivity for these experiments was 0.1mS/m; which is the lowest conductivity we have access to in our laboratory and corresponds to the conductivity of distilled water. We chose the lowest possible value of conductivity because we want the strongest and most reliable OET force we can generate in both systems. We can see from Fig.4.2b that the highest velocities, and hence the strongest forces correspond to the lowest conductivity(distilled water).

The selected size for the beads was 45 micrometres. The reason for the selection of this particular size is because the generated OET force in our portable device is too weak and unreliable for beads that are smaller than 45 micrometres. We must remember that the OET force is directly proportional to the volume of the particles; the bigger our beads the strongest our OET force will be. Each point in Fig.4.3 represents the average of five different measurements of the maximum velocity of beads. The error bars correspond to the range of the five measurements for each voltage. The particular value of frequency used during these experiments was selected because we found experimentally that it gave the strongest OET response for both systems.

On the results shown in Fig.4.3 we have a steady increase in the maximum reached velocity in function of the applied voltage for both system; however, our Olympus system performs systematically better than the Briefcase setup by about $50\mu m/s$. This difference is probably due to the difference in light intensity in the two systems. The Olympus setup uses a bigger and more powerful light projector that is able to generate stronger electric gradients in the device.

There are some serious limitations on both systems:

- **Our current OET system is not suitable for the manipulation of a big number of micro-particles simultaneously**: Our OET technique as it is does not allow the systematic manipulation of a much bigger number of particles simultaneously. We believe this kind of applications is much more suited for the individual analysis of particles rather than the sorting and enrichment micro-particles in big numbers.

- **It requires the use of a crossover frequency**: An application of this technique for the separation/enrichment of micro-particles would require the use of a crossover frequency for the discrimination of particles based on its dielectric properties; this would require a careful tunning of the medium's conductivity. Of course, the need of a crossover frequency for particle sorting in not exclusive to or our system. Virtually every application of DEP/OET uses a crossover frequency and/or relies on a competition between OET/DEP force and an external force of different nature to achieve particle sorting/discrimination. Two common examples of this would be: Free Flow Fractionation [73], which depend on a competition between DEP force and gravity; and Pulsed DEP [43], which relies on a competition between a pulsed DEP force and a constant fluid force.

- **OET force's dependence on the conductivity of the suspending medium**: We also have a dependence of OET force with the conductivity of the suspending medium, see Fig.4.2b. The conductivity of the suspending medium needs to be experimentally adjusted in order to generate an OET force that is effective for the movement of particles.

- **Our OET system as it is only works in batch mode**: Another disadvantage of our current OET system is that it works on a batch mode only; which compromises the particle throughput and make the loading and recovery of samples relatively complicated for an user with non relevant technical skills in this matters.

Besides these three main limitations mentioned already, there are also some other minor disadvantages which are more technical in nature. For example, an optical system like the

one shown in Fig.4.1A and B is fragile, bulky, susceptible to mechanical perturbations and relatively expensive to implement.

Several different continuous and discontinuous bioparticle separation techniques that involve a DEP force in one way or another have been developed over the years. For example: free flow fractionation, which uses gravity force against DEP [73]; Optoelectronic tweezers (OETs), which uses a photoconductive material to create virtual planar electrodes [10]; multiple frequency DEP, which sort cells according to the dielectric response to cells at multiple frequencies [45]; lateral driven DEP, which is generated by a planar interdigitated electrode array placed at an angle to the direction of flow [74]; and pulsed dielectrophoresis, which makes separation of polystyrene beads of different size by tuning the interaction of a pulsed DEP force with a constant fluid force in a microfluidic channel [43]. For a more comprehensive review of DEP-based separation strategies please refer to Chapter 2 of this thesis or to the excellent review on DEP technology done by Ronald Pethig [22].

Many these methods have proven to be effective for the separation of highly specific bio-particles. Between these designs, we can find a wide range of particle sorting rates. The work done by Matthew Pommer et al. is probably a good example of a DEP based microseparator with one of the highest sorting rates. Their design can sort 2.2×10^4 particles/second; which is used to enrich platelets in label-free manner. Ronald Pethig [22] summarizes the performance reported in the literature for several DEP-based particle sorting devices which do not employ labelling or tags. Considerable advances have been made regarding the maximum sorting rate achieved for some highly specific target particles; however, conventional DEP technology adapted to lab-on-a-chip devices still requires bulky electronics and other specialized lab equipment to operate. There is still work to do regarding the developing of automated and simplified systems for clinical diagnostics without requiring the tagging of target particles. Moreover, discontinuous microseparators usually require complicated manipulation of fluids due to a discontinuous operating procedure that involves: sample loading; particle trapping using DEP; washing of unwanted particles; and particle recovery [9].

The vast majority of continuous and discontinuous microparticle separation techniques make use, in one way or another, of positive DEP force, negative DEP or a combination of DEP and an external force of different nature. Usually this requires a careful control of the conductivity of the suspension medium in order to take advantage of the crossover frequency. Here we have followed a different approach, we have developed a portable, all-in-one, continuous flow DEP based electronic microparticle separator **capable of tailoring the potential energy landscape** a particle would experience across the entirety of our microfluidic channel by using just negative DEP. The tailored potential energy landscapes allow us to achieve lateral sorting and/or concentration of a heterogeneous mixture of particles as they travel through an especially designed microfluidic channel. The potential energy landscapes are created and shaped through a combination of non-uniform

electric fields, which are generated by a system of 64 individually addressable metallic electrodes embedded at the bottom of our microfluidic channel.

This is not the first time a system of individually addressable electrodes is implemented on a DEP device. Previously, Chun-Ping Jen et al [40, 42] designed a handheld device for cell concentration. In their design the microfluidic module uses circular electrodes to generate stepping electric fields in order to concentrate cancerous cells in a batch mode. Their handheld electronic device comprises a voltage-frequency converter and an operational amplifier module. However, what is different about this work is that to the author's knowledge, this is the first time a portable device is reported that uses a system of individually addressable electrodes to shape and control the particle's potential energy profile across the entirety of a microfluidic channel and in this way achieve lateral sorting of microparticles in continuous flow. We present simulation results to illustrate the physics behind this new technique along with experimental results demonstrating the separation of polystyrene beads. The electronic device is illustrated in Fig.4.5.

4.2 Operational principle.

The DEP(dielectrophoresis) force is a field induced force able to act on neutral particles when these are immersed in non-uniform electric fields. The DEP force on a particle of radius r; suspended on a fluid can be expressed as [46]:

$$F_{DEP}(t) = 2\pi\varepsilon_m r^3 Re[f_{CM}]\nabla E^2 \qquad (4.3)$$

where E is the electrical field, ϵ_m is the absolute permitivity of the suspending medium and r is the particle radious; f_{CM} is known as the Clasious-Mossotti (CM) factor, which is given by

$$f_{CM} = \frac{\bar{\epsilon}_p - \bar{\epsilon}_m}{\bar{\epsilon}_p + 2\bar{\epsilon}_m} \qquad (4.4)$$

where $\bar{\epsilon}$ is the complex permitivity, defined as

$$\bar{\epsilon} = \epsilon - j\frac{\sigma}{\omega} \qquad (4.5)$$

and subscripts p and m stand for the particle and the medium, respectively.

This technique relies on a competition between time-varying DEP forces. The device is able to shape the resulting forces affecting the microparticles throughout the whole microfluidic channel. This allows us to generate a long-range slopping-shaped potential with periodic wells embedded on it. By adjusting the settings we can control the long-range potential's slope as well as the depth and width of the wells.
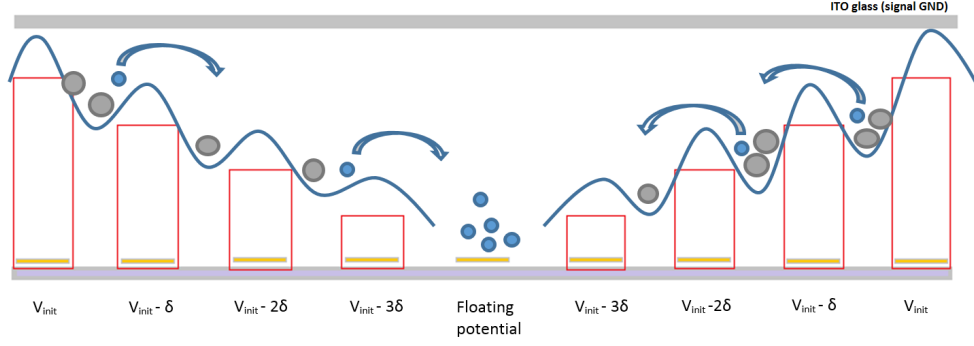
Figure 4.4: Diagram representing an instance of a tailored potential energy landscape shown as a blue line. Several local minima and a long range potential slope are generated over the whole length of the microfluidic channel; which allows us to trap particles of one kind and at the same time sort laterally particles with different electric properties, size or shape. The metallic electrodes run parallel to one another down the whole length of the microchannel. They are 20μm wide and have a separation of 30μm between them. The ceiling of the channel is ITO glass connected to a ground signal. A 15kHz sinusoidal wave is applied to each electrode for which $V_{init} = 14V_{pp}$ and a pulse duration $\Delta=300\mu$s. The applied AC voltage is changed by the same magnitude δ from one electrode to the next. On this diagram we depicted only 9 electrodes, however, the real device has 64 electrodes. The main section of our micro-channel is 3.2mm wide, 100μm high and 4.0cm long.

The gradient of the electric field to the square ∇E^2 is the term that defines the shape of the force field particles will be subject to; however, a particle is not subject to the effect of just one electrode but many(64 in our experiments). The resulting force on a given particle will be produced by the sum of the effects of every single electrode in the vicinity. For achieving a potential profile able to trap/release micro particles of given characteristics we have experimented adjusting the values of voltage, inter-electrode separation and the pulse duration; leaving the frequency unchanged as we intended to work only with negative DEP forces: particles moving away from high electric gradients. Working with negative DEP exclusively make things easier given that positive DEP causes the attachment of particles to the electrodes. In order to create a potential ramp the voltage value of each electrode was set according to:

$$V_{n,t} = V_{init} + n\alpha_{n,t}\delta \tag{4.6}$$

where V_{init} is the initial voltage in the sequences; $V_{n,t}$ is the voltage in the n-th electrode; and α is a two dimensional matrix that defines the structure of the long range potential in space and time, the first subindex n defines the structure in space and t defines the temporal sequence as dynamic potential structures are created by generating long range potentials sequentially. The parameter α can take three values: 1, 0, or -1; these numbers define a voltage increase, voltage decrease and inactive electrode respectively.

On the other hand, the variable δ can take the following values: 0.0V, 0.078V, 0.156V, 0.234V and 0.312V; which we redefine as $\delta 0$, $\delta 1$, $\delta 2$, $\delta 3$ and $\delta 4$ respectively. This steps are defined by the minimum resolution of our digital potentiometer. This will be explained in a bit more detail in section 4.3.2.

When a particular electrode is activated, a non-uniform electric field is generated between the metallic electrode and the grounded ITO glass on top of the chamber, see Fig.4.21 a. Each electrode in the array is activated sequentially according to a preprogrammed sequence the onboard microcontroller holds in memory. A particular electrode is activated for a short time period $\Delta t = 300\mu s$ before deactivating it and activating the adjacent electrode for the same time interval but using different voltage according to Eq.4.6. Once the last electrode on that particular sequence has been activated, the system goes back to activating the first one and so on. We have given each electrode the same weight on the combined electric gradient by making Δt the same for each electrode. We have found experimentally that the DEP force field gets stronger and more effective as we decrease Δt, but only until it reaches values around 300 microseconds. Pulse durations smaller than 300 microseconds do not seem to make any difference to the performance. On the other hand, values that are considerably higher than this will break the potential gradient and remove the relation to δ values. The result of this is to produce a sweep of electric field that passes across the device. Keeping the frequency and pulse duration Δt constant and adjusting the values of Δt, inter-electrode separation and V_{init} we are able to shape the energy potential over the whole microfluidic channel and use it to accomplish particle concentration and sorting.

Polystyrene beads of 1, 3, 5, and 10 micrometers in diameter(Polysciences, Inc USA) were used for the different experiments described in this paper, in a single kind or as a mixture of different sizes. When preparing a sample we mixed the bead solution with deionized water and Tween 20 to prevent the beads from sticking to the surfaces or to each other. The conductivity of the solution was monitored using a Horiba Scientific portable conductivity meter(model B-771). Finally, the PCB was mounted on the stage of an upright microscope(Olympus BX51). A 1.0mL gas-tight glass syringe(MDN-0100 BASi) and a Syringe pump(NE-1000 New Era Syringe Pump Systems) was used to deliver the sample to the microfluidic device(flow rate of $1.0\mu L/min$) through PTFE tubing(AWG size 24) with a inside diameter of 0.56mm. The motion of the polystyrene beads was recorded by a digital camera(Hamamatsu C11440). On each experiment we have: a pulsed sine wave signal with a frequency of 15kHz, which was generated by the on-board digitally programmable frequency synthesiser IC(AD9850); an initial maximum voltage V_{init} =17Vpp; and a pulse duration of 300 microseconds. The pulse duration Δt, frequency, V_{init}, δ, and the shape of the long-range potential structure were controlled using an android mobile phone via Bluetooth connection.
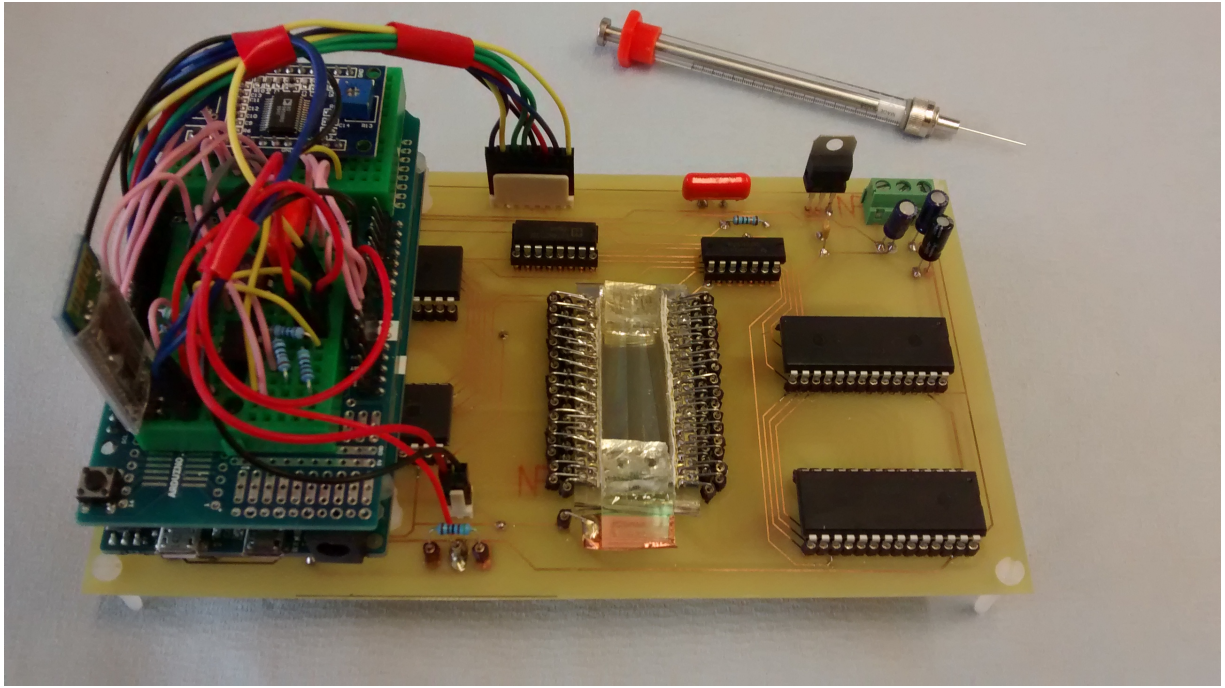
Figure 4.5: A picture of the electronic micro-separator: the microfluidic device is mounted over the main printed circuit board and electrically connected to the main circuitry. Each one of the 64 electrodes is controlled independently by the on-board micro-controller.

4.3 Experimental Section

The electronic device, see Fig. 4.5, contains the microfluidic chip and all the required electronics: function generator, signal distributor system, amplification module and a Bluetooh module for wireless communication to a mobile phone. All these components are contained in a single 11cm width by 19cm long printed circuit board(PCB) which I designed and build for this purpose.

4.3.1 Chip Fabrication

Our needs demand a different micro fabrication process for the microfluidic channel; we need a single electrode on top and an array of metal electrodes at the bottom of our microfluidic channel, which the soft-lithography method using PDMS does not allow. The internal electrodes are planar(2-D); they are fabricated using photo-lithography and lift-off technique. Subsequently, we fabricate the micro-channel over this substrate with bonded ITO glass on top [75]. In this design we use ITO glass on top of the channel to set the ground signal; this generates an electric gradient between the bottom and top of the channel in a similar manner as with optoelectronic tweezers(OET). In this respect this design is different to the common DEP configurations in which 2D planar electrodes are usually fabricated only at the bottom of the channel and thus an electric field is only effectively established in close proximities to bottom substrate.

The microfluidic chip also has 64 pads that allows soldering wires between the chip and the printed circuit board. The pads are big enough to allow an easy electrical connection of each electrode to the main PCB board using soldering iron.

The main section of the micro-channel was designed to be 3.26mm wide, 100μm high and 4.0cm long, see Fig.4.6 c. There were two main reasons for the selection of these particular dimensions for our microchannel. The first reason is related to the size and number of electrodes in our device. We decided to implement 64 metal electrodes, each one 20 micrometres wide and 4 centimetres long. We also experimented with electrodes thinner than 20 micrometres; however, those tended to break easily rendering many electrodes useless.

The intention was to make our microfluidic device as big as possible in order to increase processing rates. The separation between consecutive electrodes was 30 micrometres, which gives, as a result, the previously mentioned dimensions for the microchannel.

The other reason for that particular size was that we are very interested in testing the practicality of the technique over relatively long dimension. One of the central features of our device is its capacity to generate lateral forces through tailored potential energy landscapes. One of the central questions was whether or not those landscapes can be sustained over the entirety of a microfluidic channel that is several centimetres long and several millimetres wide.

The micro fabrication technique we used for our microfluidic channel is a modified version of one originally introduced by Cristian Witte [75] who used it for the fabrication of smaller microchannels(about 200μm wide) in an amorphous silicon(a-si) substrate. Our needs required the creation of much wider microchannels(3 millimetres wide) on a glass substrate. In order to fit our needs, we experimented with the original microfabrication protocol to achieve the desired characteristics.

The modifications to the original protocol are the following:

1. Our microfluidic device uses a customized microscope slide as a substrate. In the original protocol, ITO coated glass substrates were modified with amorphous silicon(a-Si) to obtain a photoconductive layer.

2. In the original protocol, the exposure time was 60 seconds($200\ mJ/m^3$) for a resist thicknesses less than 50 micrometres. In this work, the protocol needed to be changed to account for a SU8 film that is greater than 50 micrometres. The exposure time was increased to 160 seconds to account for a resist thickness of 100 micrometres and the absorption of UV-light by the top ITO coated coverslip.

3. Another important modification to the original protocol was made to the post-

(a) Mirror plus electrode array.

(b) Electrode array plus SU8 and ITO glass.

(c) After developing.

(d) After PDMS-glass bonding.
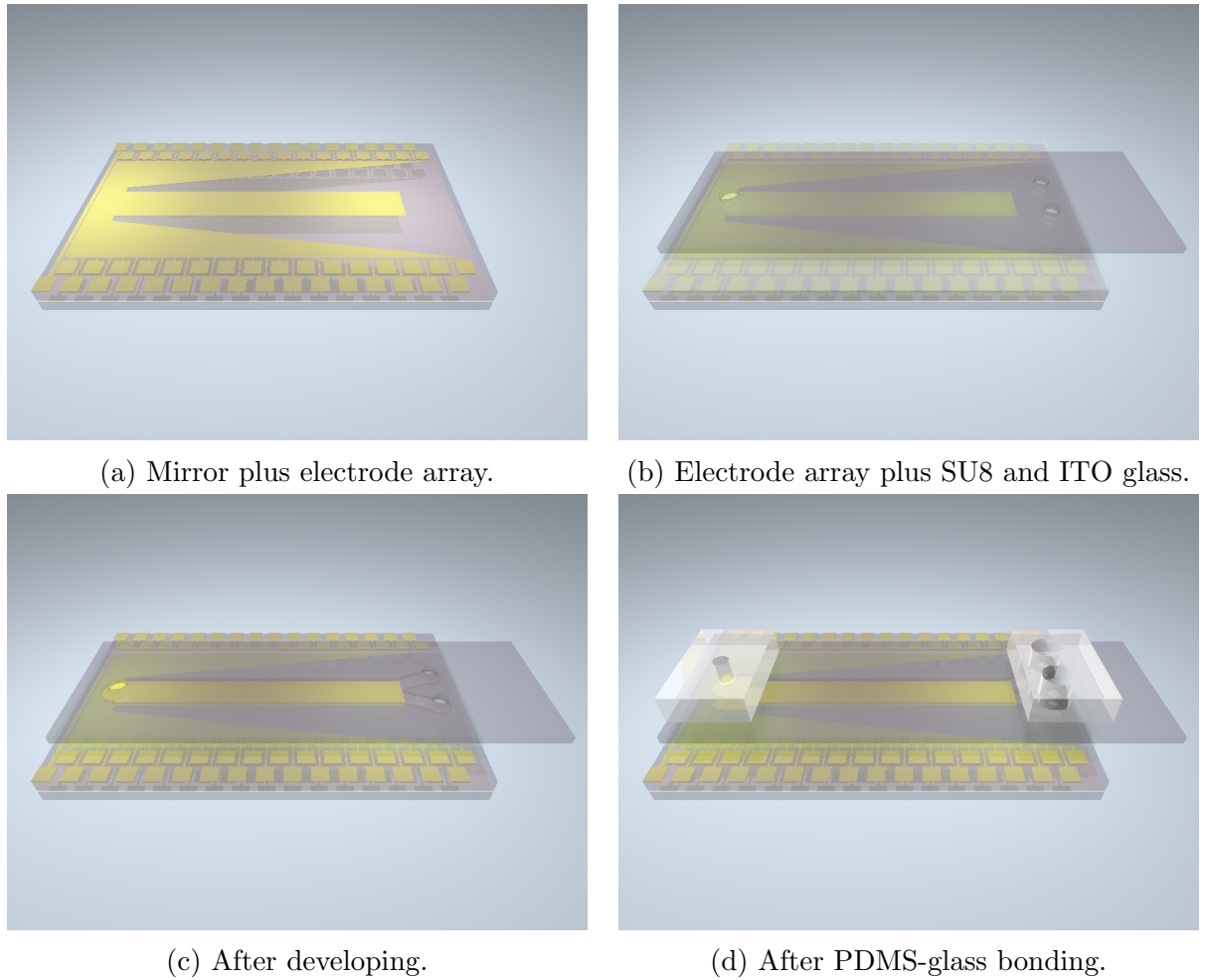
Figure 4.6: A graphical representation of the different steps involved during the microfabrication process. The finished microfluidic device contains 64 gold electrodes on a glass substrate. The microfluidic channel was designed to be 3.26mm wide, 100 μm high and 4.0cm long in its main section. The ceiling on the microfluidic channel is ITO glass. The device contains one inlet and two reservoirs.

exposure bake. In the original protocol, a post-exposure bake at 65°C for 2 minutes and 95°C for 6 minutes was performed prior to the development of unexposed SU8 through inlet and outlet holes. However, here, this step was eliminated because otherwise, the developing time needed is considerably longer and hence impractical. The developing time when including a post-exposure could be up to a week or even not possible at all. We have found experimentally that even without a post-exposure bake a well-defined microstructure is generated in the exposed regions.

In the next paragraphs, the new protocol is introduced already containing all the already mentioned modifications.

The first step in the microfluidic chip fabrication process is to pattern the array of 64 metallic electrodes on a standard but cut to size microscope slide(W:25.4mm X L:56.0mm X H:1.0mm) using standard photolithography; we deposited Titanium(10nm) adhesion
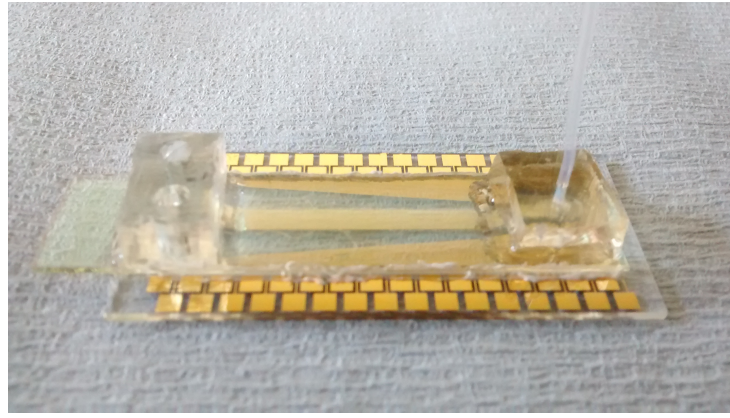
Figure 4.7: Finished microfluidic chip.

layer first and subsequently a Gold(120nm) layer to generate the array of electrodes, see Fig.4.6 a. The electrodes are 20 micrometers wide and are separated by 30 micrometers from one to another.

The second step consists on spinning SU8 3050 on top of the substrate with the metallic electrodes. The speed was set at 4000 rpm for the 30s to give us a thickness of 120μm. After spin coating, the substrate was placed on a hotplate at 95C for 5 minutes. Subsequently, another customised cover slide(W:16.0mm X L:65mm X H:1.0mm) coated with 0.3 micrometre ITO layer and containing three 1mm in diameter predrilled holes(to form inlet and outlet) was carefully placed on top(ITO side facing down) while the substrate is still on the hotplate, see Fig.4.6 b. We leave the device on the hot plate for another 5 to 6 minutes to allow for air bubbles to disappear. This microfluidic device has one inlet and two outlets. The idea behind having two outlets was to be able to easily collect the processed sample and residues at separate points.

In the next step, we expose and develop the photoresist in order to define the dimension and shape of the microfluidic channel. The photoresist is exposed for 160 seconds(200 mJ/m^3) through a mask aligned to the predrilled holes in the tailored ITO glass. No post exposure bake prior to the developing of unexposed SU8. We developed the device through the drilled holes on the top microscope slide using Microposit EC solvent. The development is made by placing the chip in a bath with EC solvent. The container is placed in a properly ventilated fume hood. Every 12 hours the EC solvent is replaced and the microfluidic chip examined under the microscope. The development process is slow but easily observed when the chip is inspected with a microscope. We found experimentally that it takes between three and four days to develop each device. This particularly long time is due to the reduced access of the developer to our exposed microchannel. Even when the developing process is slow it is also uncomplicated; we did not experience any major complications during this step.

During the last step in the fabrication process of our microchannel, we remove any

residues left in the channel structure by placing the chip in a bath with acetone for 5 minutes. Afterwards, we rinse it properly with DI water and air dry with pressurised nitrogen until the water inside the chip is fully removed.

The next step is to fabricate the connector for inlet and the two reservoirs. For this, we prepared a mixture of PDMS prepolymer and curing agent at a weight ratio of 10:1. Stir the mixture carefully and then degas it under a vacuum for 30 minutes; pour the degassed mixture into a flat container and bake it for 4 hours at 65 C. Peel off the solidified PDMS, cut two rectangular blocks(H:0.7mm x W:1.0cm x L:1.5cm) with flat surfaces. Next we clean it in Acetone, Isopropanol for 5 minutes in an ultrasonic bath, followed by rinsing with DI water and blow dry. To make sure no water is left on the surface a dehydration bake at 120c for 5 minutes was performed then we punch a hole for the inlet(using a 1mm biopsy punch) and two more for the reservoirs(3mm biopsy punch). Before bonding the PDMS pieces to the glass we make sure it is properly clean, then treat the two blocks of PDMS and the developed device with oxygen plasma at 3000mTorr and for 30 seconds. After this, we immediately align and bond the two PDMS blocks to the glass surface. To make sure the two blocks are properly bonded, soft bake the device for 5 minutes at 120C; this will strengthen the glass-PDMS bond. A picture of the finished microfluidic device is shown in Fig.4.7.

4.3.2   Apparatus

4.3.2.1   Function generator

In our device we use the AD9850BRSZ as our on-board digitally programmable frequency synthesizer. When referenced to our external clock source(125MHz) it can generate a spectrally pure, frequency/phase-programmable, analogue sine wave. The signal generated by this integrated circuit is the input of an amplification module, see Fig.4.10 and 4.11, which rectifies and amplifies it to generate a good quality sinusoidal signal, which has a more than adequate upper frequency limit(1.5 MHz) and a satisfactory voltage range(0 - 20Vpp) for this particular frequency range. The AD9850BRSZ uses a high speed DDS core which provides a 32-bit frequency tuning word, which results in an output tunning resolution of 0.0291Hz, for our 125MHz external reference clock. The output frequency can be digitally changed at a rate up to 23 million new frequencies per second. It can reach frequencies up to one-half the reference clock frequency(62.5MHz). However, the amplitude of the generated AC signal is limited by the so called *break over frequency*; where the gain of a real operational amplifier(OPAM) drops to about 70.7% of the maximum gain. For the typical operational amplifier this value is around 1MHz, but for our amplification chain, see Fig4.11, the *break over frequency* is around 1.5MHz; which limits our AC signal to a effective to a maximum of about 1.5MHz. This reduction in voltage gain as the frequency increases is caused by a low-pass filter-like characteristics inherent to the inner

circuitry of the used operational amplifiers [76].

The frequency and amplitude of the generated sinusoidal wave is changed by the *electrode actuation program* running in the on-board micro-controller.

4.3.2.2 Signal distributor system

The signal distributor is a digitally controlled device that takes a single data input; in our case a sinusoidal wave, and routes it to one of the several possible outputs, see Fig.4.9. For this application an analog signal distributor was designed and built that it is able to send a single sinusoidal signal to any of the 64 independent electrodes, one at a time. For the design and testing of all the electronic modules in this prototype we used Orcad Capture. Similarly, for the design and routing of our PCB board we used the Orcad PCB designer which allowed us to integrate the different parts of our system is a single double-sided PCB board that is small, practical and robust, see Fig.4.5.

It worth mentioning how important is was to achieve a electronic board that is small, practical, reusable and easy to connect to the microfluidic chip. One of the reasons is because the main PCB board is a electronic system that require a considerable care for the fabrication, assemble and testing. However, once all the components are in place and working, the final product is remarkably robust and reliable for laboratory testing. We paid special attention to the design of the so called microfluidic chip's *footprint* in the PCB board; which is the physical socket for the physical and electrical connection of the microfluidic chip in the main PCB. We made sure the physical dimensions of the footprint in the PCB perfectly match the ones of the microfluidic chip and the dimensions and position of the electric pads allow an easy and robust electrical connection for each one of the 64 electrodes. As a final result we have a device that allows us to connect and disconnect a new microlufluidic chip just by removing the previous one and connecting a new one using a soldering iron; which makes the system truly reusable.

It also worth mentioning we previously experimented using a micro-boding machine for the electrical connection of each one of the 64 electrodes; however, we discovered the connections were not reliable as many of the micro-wires would snap even with the slightest mechanical disturbances. In addition to this, a successful wire bonding requires surfaces that are perfectly clean and free from dust, which just adds extra complications to the fabrication process and could make the device useless in places where there is not access to a laboratory, or clean-room facilities. This is why we decided to increase the size of the electric pads and redesign the microfluidic chip's footprint to substitute the micro-wire bonder for a common soldering iron.

We are satisfied with our method for the connection of electrodes to our main PCB board. The installation of a new microfluidic chip in the PCB is easy and straightforward; re-
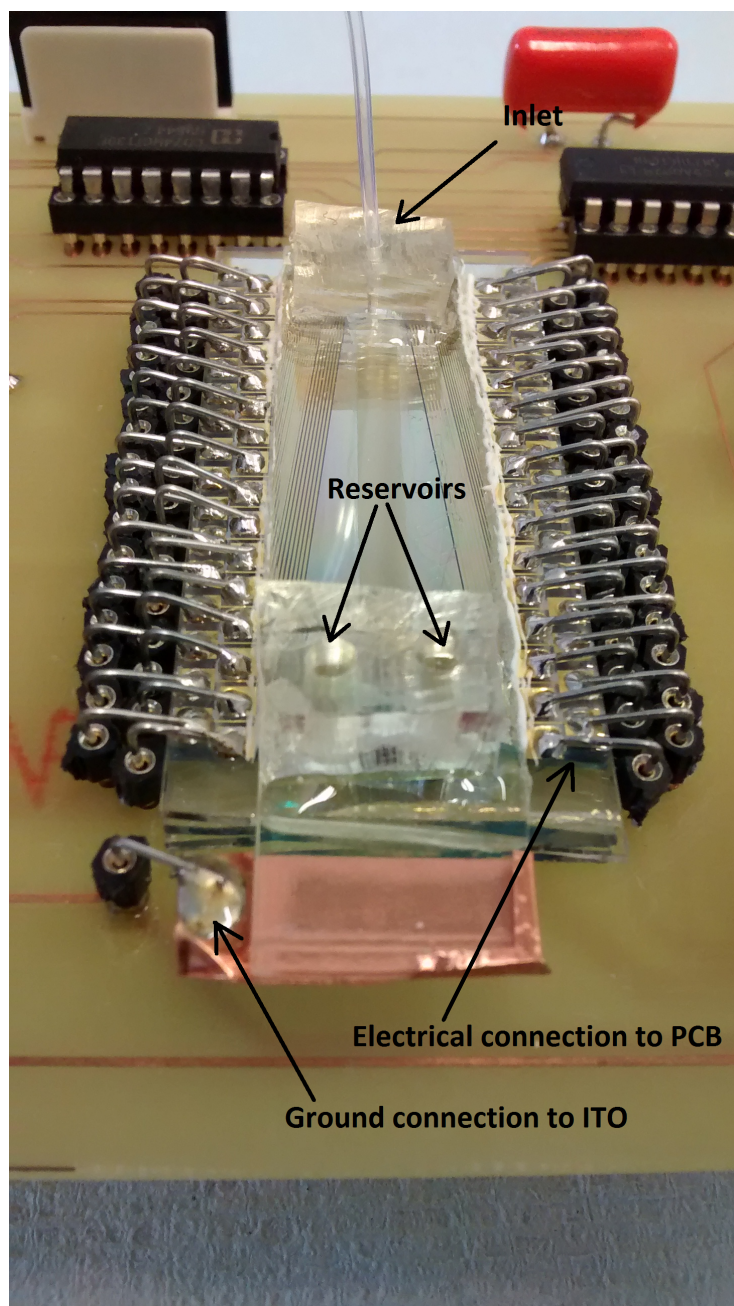
Figure 4.8: The microfluidic device is mounted over the main PCB board through a socket specially designed for that purpose. There is a single inlet and two reservoirs at the end of the microfluidic channel. We have also included a mirror on the base of the socket. This mirror was fabricated by depositing 20nm of Aluminum on a cut to size microscope slide. The function of this mirror is to enhance the image we get when mounting the whole device on a upright microscope as the system is illuminated form the top. Each one of the 64 electrodes and the ground signal are connected to the main circuitry using short wires soldered to the gold pads in the substrate using a common soldering iron. This short wires are also connected to the main board through a female connectors; which makes the PCB board truly reusable. The removal and installation of a new microfluidic device becomes straight forward and in the end we have a system that is remarkably robust and is able to withstand more than its fair amount of mechanical perturbations. Each one of the electrodes is controlled independently by the on-board micro-controller.

quiring less than two hours and without any specialized electronic equipment. This new technique achieves a remarkably strong and robust electrical and physical connection between the microfluidic chip and the main PCB board, see Fig4.8. Actually, the strength and robustness of the electrical connections is so good it can resist more than the fair amount of mechanical vibrations you would normally expect during laboratory testing. However, more packaging would be required before it could be field tested. The design of the microfluidic chip's footprint was also made using Orcad Capture.

The 64 electrical connections in the microfluidic chip are bilateral and equally matched for AC or DC signals. For this purpose we made used of the DG406DJ single 16-channel CMOS analog multiplexer. Its 44V maximum voltage range permits controlling up to 30Vpp signals when operating with ±15V power supplies.

The on-board micro-controller sends a 7 bits signal to the main PCB. The first six bits are for addressing each one of the 64 electrodes, the 7th bit is for enable/disable of the complete system, see Fig.4.9. This is achieved by using a 2-to-4 line decoder with active low output. The 74HCT139 decodes two binary address pins(5,6) to four mutually exclusive outputs($\overline{Y0},\overline{Y1},\overline{Y2},\overline{Y3}$). This is very important because we need to activate only one of the four DG406DJ multiplexers at each given time. The 7th bit goes to an enable input($\overline{E}$) which enables/disables the four multiplexers. Because we are using a decoder with active low output we also need a logic inverter. The 74HC04 inverts the logic of the output signal of the 2-to-4 decoder before they reach the enable pin of each one of the four 16-channel multiplexers.

The task of redirecting the sine waveform to the different electrodes is carried out by the electrode actuation program through the use of the time control tools and the digital I/O capabilities of the Aduino Due.

4.3.2.3 Voltage amplitude control

Our experiment requires a very precise and fast digital control of the amplitude of the generated AC signals. This important step is implemented in two parts: voltage rectification and voltage amplification. In Fig.4.9 we represent these two steps in a single module we call **amp_module**. In the first part, Fig.4.10, we have a the original positive sinusoidal signal with an amplitude of 2.0Vpp and an offset close to 1.0V DC; this signal is the raw output of the AD9850BRSZ.

We need to achieve amplitude control before eliminating the DC component of the signal and implementing the actual amplification process. This is precisely what we have achieved with the circuit shown in Fig.4.10. First we apply a summing amplifier and after that we send the resulting signal through a inverting amplifier. As a result we have a sinusoidal signal with an offset of 3.2V DC. This is important because the lower values of the original sine wave are too close to the origin and attempting to amplify it would
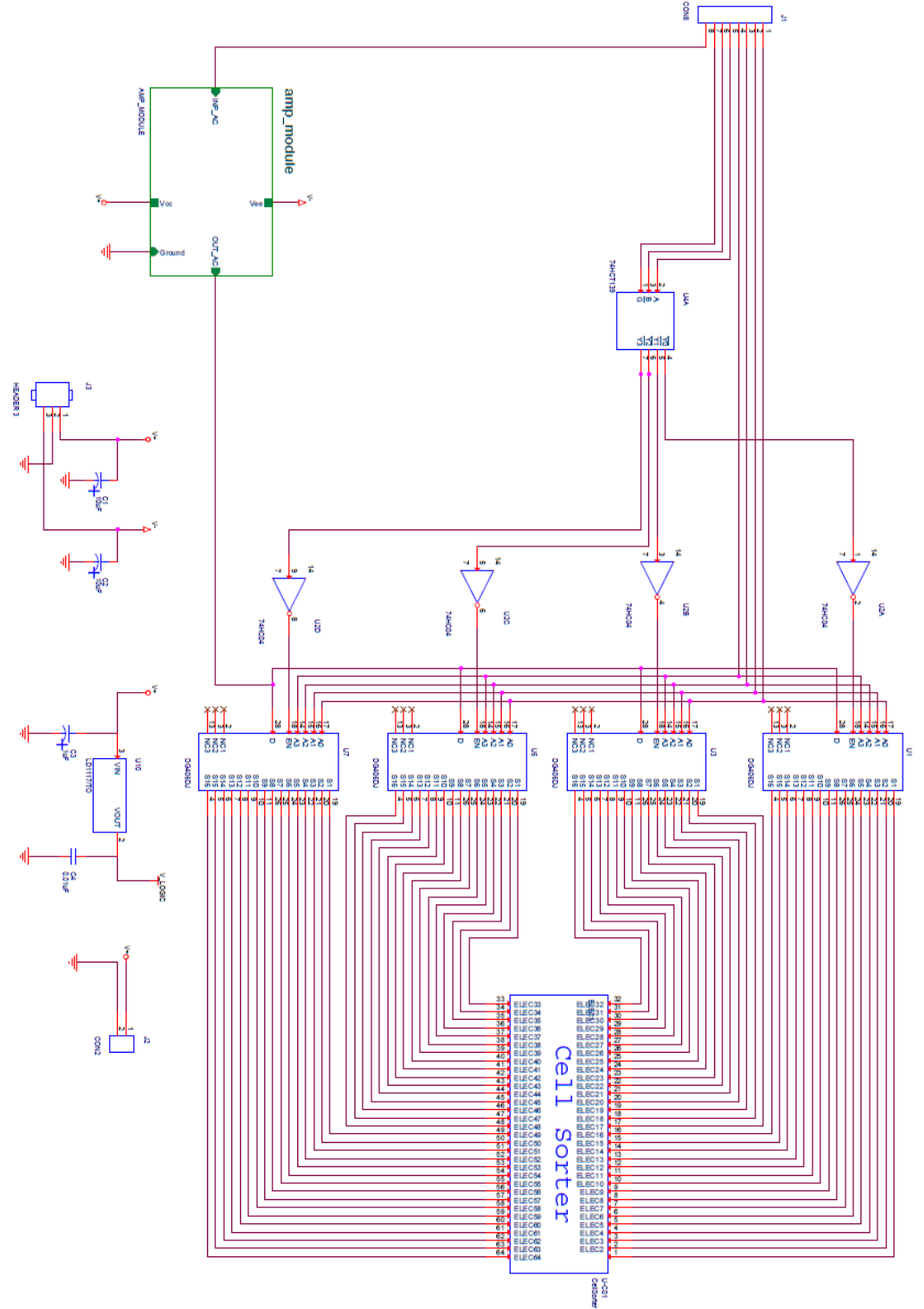
Figure 4.9: Schematics of the demultiplexer system used to control address each one of the 64 metal electrodes in our device.

give us as a result a deformed function for the lower values. It seems the amplification is not uniform for voltage signals that are close to the origin(<1.0V). However, after applying these operations to the original signal it is read for the amplitude modulation step. This is achieved through the use of the MCP4161, which is a single digital potentiometer with non-volatile memory. We connect this digital potentiometer to our on-board Arduino micro-controller through a serial peripheral interface(SPI). This allows us to change the resistance output of the wiper terminal through software, see Fig4.10. The communication is also synchronous, which means the data is transmitted in synchrony witch the clock signal in our micro-controller. The Arduino environment already contain a built-in library and hardware for SPI communication. The particular digital potentiometer we use for this project is the MCP4161-103, which is a 10 kΩ digital potentiometer with 8-bit resolution (257 steps). It can change resistance in a total of 257 steps, from 0 to 257. For our 10 kΩ this means that each step is an increment of approximately (10K/257) 39Ω; this is the characteristic that defines the minimum voltage increments/decrement we use in our experiment: the magnitude of voltage change we will later be defined as δ. After achieving control over our sinusoidal signal's amplitude we proceed to eliminate the DC component and amplify it, see Fig.4.11. To eliminate the DC component we use a high pass filter. After this our signal goes to the amplification chain; which is a group of three inverting amplifiers connected sequentially. In all these rectification and amplification steps we choose to use the dual Op amp TLE2072CP because of its low-noise high-speed characteristics; it yields a typical floor noise of 17nV/Hz, has a bandwidth of 10MHz and a supply voltage range from ±2.25V to ±19V. All this makes this operational amplifier an ideal choice for our application. As a result of this steps we have a clean AC singnal, see Fig.4.12, which can be controlled through pulse duration, frquency and amplitude.

4.3.2.4 Electrode actuation program

Each one of the 64 electrodes can be accessed and controlled independently by a specially designed C program running on the on-board micro-controller(Atmel SAM3X8E). This program has total control over which electrode to activate/deactivate, its frequency, pulse duration and AC voltage amplitude. This unique capability is what allows us to generate the tailored potential energy landscapes by very rapidly activating/deactivating electrodes with different voltage amplitudes. The tailored potential landscapes are created by the micro-controller through a set of instructions we program in our Arduino Due's flash memory. These instructions define the shape of the potential landscapes by activating a series of electrodes in a particular sequence. The very important task of setting the pulse duration of each AC signal relies on precise timing of microsecond intervals. For that we use the **delayMicroseconds(μs)** function of the Arduino environment, which provides accurate delay and timing control. The delay timing is specified in millionths of
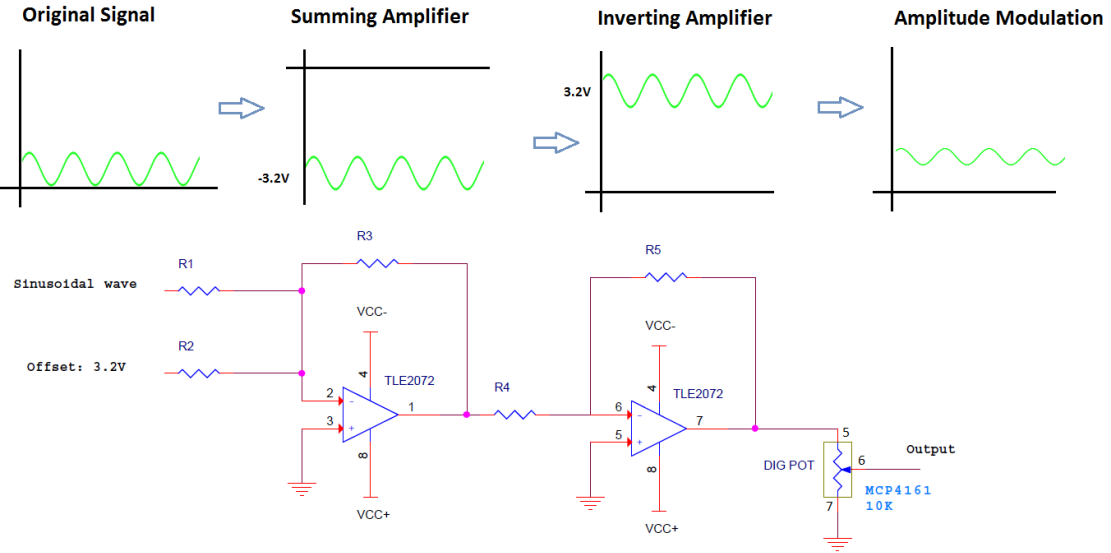
Figure 4.10: Schematics of the modulation and amplification steps used to control the amplitude of the original sinusoidal signal.

a second. The instruction **delayMicroseconds(1000)**, for example, will create a delay of one millisecond or 0.001 seconds. This function works very accurately in the range 3 microseconds and up [77]. There is no assurance this function will perform precisely for smaller time delays. However, the smallest delay we used in our experiments was 300 microseconds.

We program this structures in the C programming language using a two dimensional integer array that only contains three possible options: 0, 1 and -1. Where 0 represents a deactivated electrode, 1 represent a unit increase($+\delta$) in voltage and -1 represent a unit decrease($-\delta$) in voltage. We generate long range potentials of any desired shape by specifying in the arrays how many electrodes will be involved, how many of them will be inactive and the corresponding increases/decreases in AC amplitude, see Fig.4.4.

There is another set of instructions needed to fully define the conditions for an experiment, these are: frequency, δ, V_{init} and pulse duration Δt. However, this instructions are not pre-programmed in the micro-controller memory. This information is sent to our device using Bluetooth wireless communication through an android mobile phone. This feature is more than just a convenient way to set and modify the values for electrode structure, frequency, δ, V_{init} and pulse duration Δt; it is actually a necessity because otherwise we would need to reprogram the micro-controller every time we need to set new conditions. Also, during and experiment the PCB board is mounted on the stage of a upright microscope which does not allow as to easily connect and disconnect the device to a PC or laptop without causing mechanical disturbances and bringing the optical system out of focus.
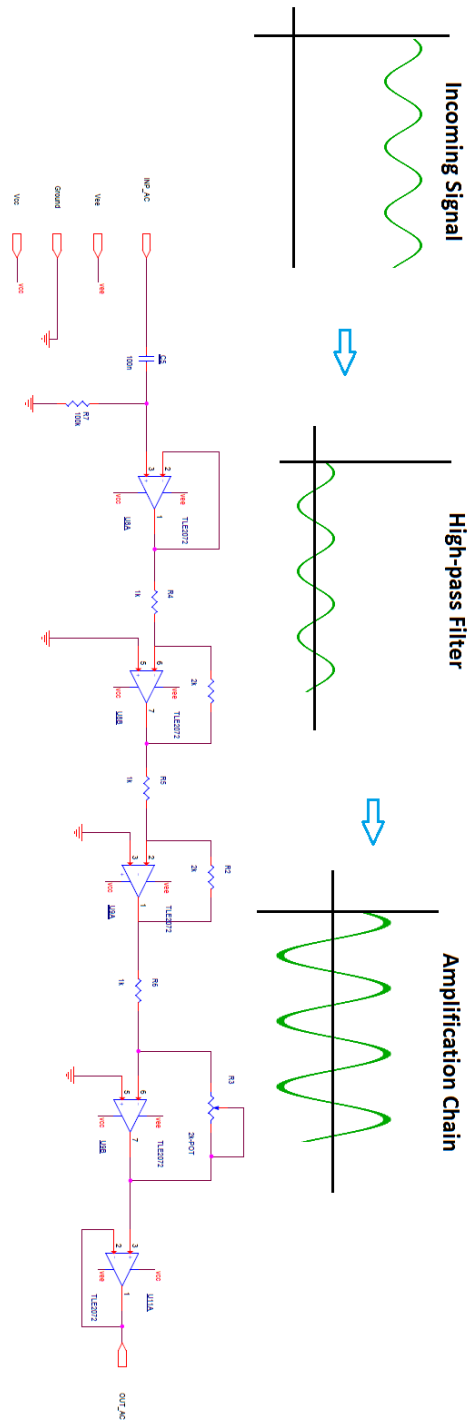
Figure 4.11: Schematics of the modulation and amplification steps used to control the amplitude of the original sinusoidal signal.
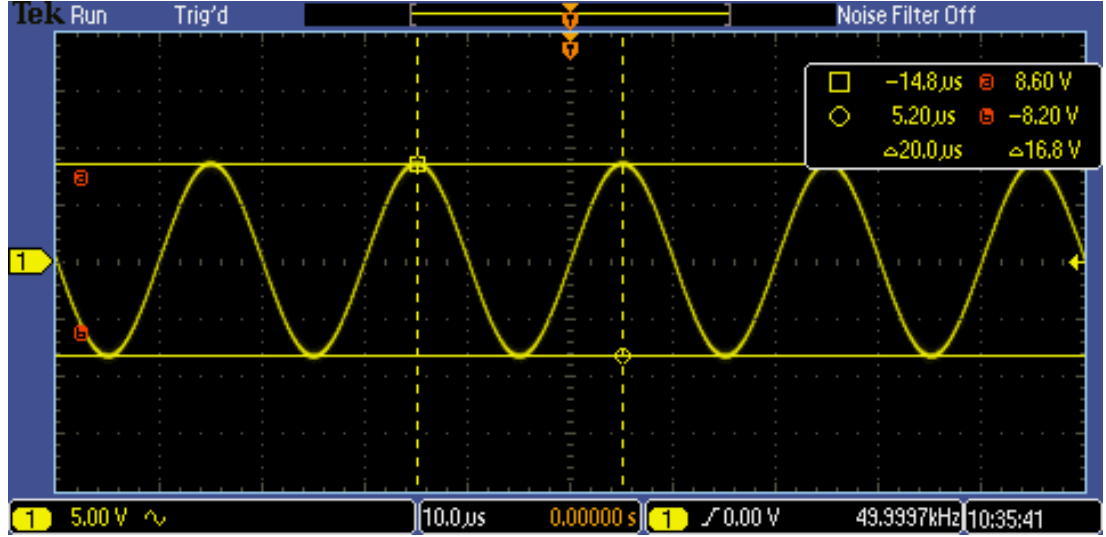
(a) Oscilloscope snapshot of the generated sinusoidal signal.
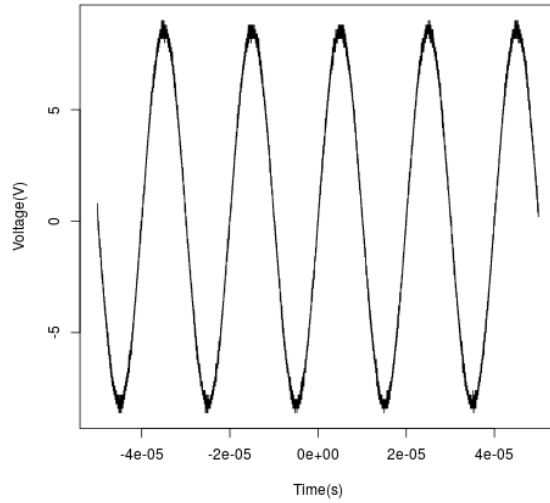
(b) Sinusoidal signal
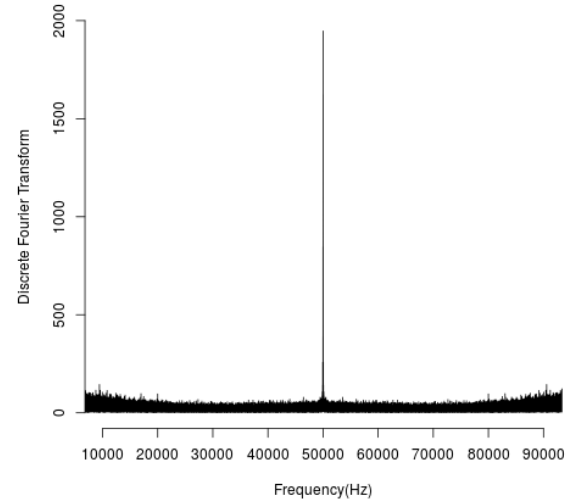
(c) Fourier transform

Figure 4.12: An instance of a digitally generated AC signal: V_{init}=16.8Vpp, frequency = 50kHz. The frequency, pulse duration, and amplitude of the signal can be modified in real time through software. a-b) Raw output of our on-board signal generator as measured with an oscilloscope. c) Discrete Fourier transform applied to the signal.
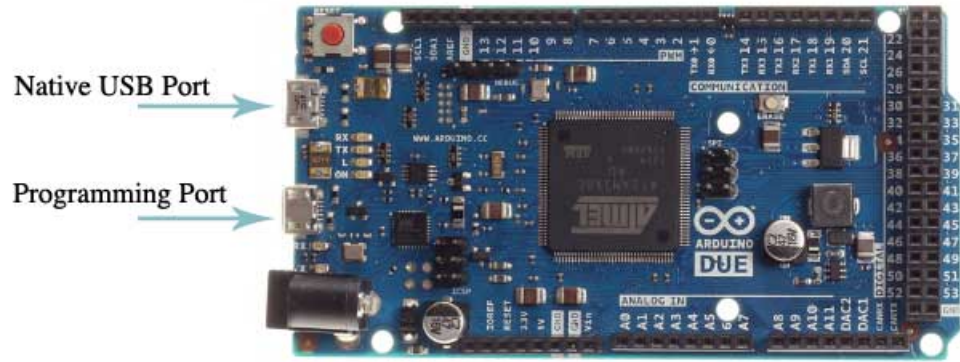
Figure 4.13: Arduino Due board is our micro-controller for our prototype. It contains everything is needed to support the Acmel SAM3X8E ARM Cortex-M3CPU. Source: Arduino [77]

4.3.2.5 On-board microcontroller

This is a micro-controller board(Arduino DUE) based on the Acmel SAM3X8E ARM Cortex-M3CPU; the fastest in the Arduino family as it runs at 84 MHz. The board is based on a 32-bit ARM core microcontroller and it contains everything that is needed to support it. This particular Arduino works at 3.3V and we can power it with an AC-to-DC adapter or battery. The board can operate on an external supply of 6 to 20 volts which makes it ideal for our prototype because we use a bench DC dual power supply (±15V) for all the experiments described in this document. However, the device can also be powered by batteries. Some of the main features of the Arduino Due board are:

- A 32-bit core, that allow operating on 4 byte data within a single CPU clock.

- CPU Clock at 84 MHz

- 96 KBytes of SRAM

- 512 KBytes of Flash memory

4.4 Modeling and results

4.4.1 Particle counting and tracking.

To monitor the movement of polystyrene beads passing through the microfluidic channel we used video analysis software of our own design [78], which was introduced in Chapter 3. The program was written in C++ and is able to identify, track and count multiple particles simultaneously. For this particular application, however, our software is given the task

of tracking and counting the number of polystyrene particles on a frame. This algorithm could be divided into several steps: static background subtraction, apply morphological operations, image segmentation, and multi-particle tracking and counting.

For the experiment shown in Fig.4.14 we used polystyrene beads of 10 micrometres in diameter and four different potential profiles: $\delta 1$, $\delta 2$, $\delta 3$, $\delta 4$. The purpose of this is to illustrate how effective each one of the potential profiles is for trapping/moving beads; it also shows an instance of the trajectory followed by a particle for each condition.

For the first condition: $\delta 1$, where the potential difference between electrodes is 0.078V, see Fig.4.14 a; the particle follows a linear trajectory in the direction of the main flow. The energy potential well is too high for the particle to overcome and the particle is retained on that x position at the same time it moves in the y direction due to the flow. On the second condition: $\delta 2$, where the potential difference between electrodes increased to 0.156V, see Fig.4.14 b; the particle has a velocity component in the x direction as the particle is released from its local potential well and is able to move down the main potential slope. However, small changes in the x velocity are still observed as the particles move through the potential wells.

On the third condition: $\delta 3$, where the potential difference between electrodes is 0.234V, see Fig.4.14 c; the particle follows a similar trajectory as in the previous case. However, this time the movement is smoother and faster as we have increased the slope of the long-range potential and at the same time decreased the depth of the potential wells. On the last case: $\delta 4$, where the potential difference between electrodes is 0.312V, see Fig.4.14 d; a particle's trajectory follows the same trend as in the two previous cases: it travel even faster in the x direction as once again we have increased the slope of the long range potential.

The number of particles on a frame for each one of the four potential profiles was counted using our software; a summary of the results is shown in Fig.4.15. For $\delta 1$ we have all particles moving through the microfluidic channel trapped in the potential wells; which means there would be no movement in the x-direction, this gives us a steady number of particles which is only subject to the natural random fluctuations in the number of particles crossing through the frame. For $\delta 2$, $\delta 3$ and $\delta 4$, on the other hand, we have a steady decrease in the number of particles on the screen over time as they are moved in the positive x direction and off the screen. There is also a decrease in the time it takes to clear the frame from particles. As we can see, there is a clear trend showing and increase in the particle's speed as we increase the long-range potential slope.

4.4.2 Paricle's trajectory and velocity

After obtaining the particle's position over time, Fig.4.14, we proceeded to numerically compute the velocity for the four potential profiles in consideration: $\delta 1$, $\delta 2$, $\delta 3$ and $\delta 4$. In

(a) Trajectory: $\delta 1$.

(b) Trajectory: $\delta 2$

(c) Trajectory: $\delta 3$
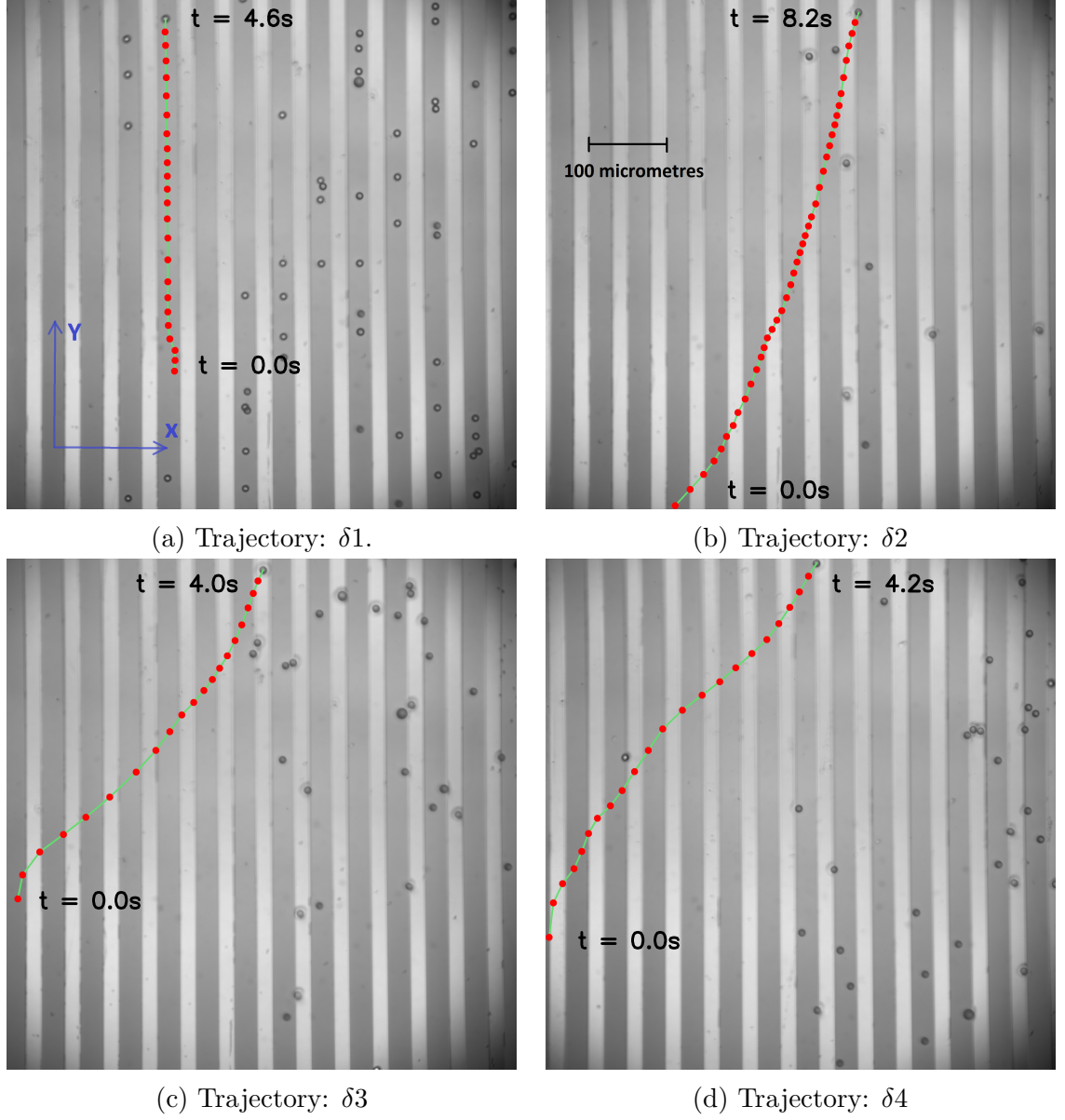
(d) Trajectory: $\delta 4$

Figure 4.14: The trajectory followed by a single particle under four different potential profiles: $\delta 1, \delta 2$, $\delta 3$, $\delta 4$. The volumetric flow rate was set to $1\mu L/min$ with a 15kHz sinusoidal wave for which V_{init}=14Vpp, conductivity of the medium = $77\mu S/cm$, and Δt=300μs
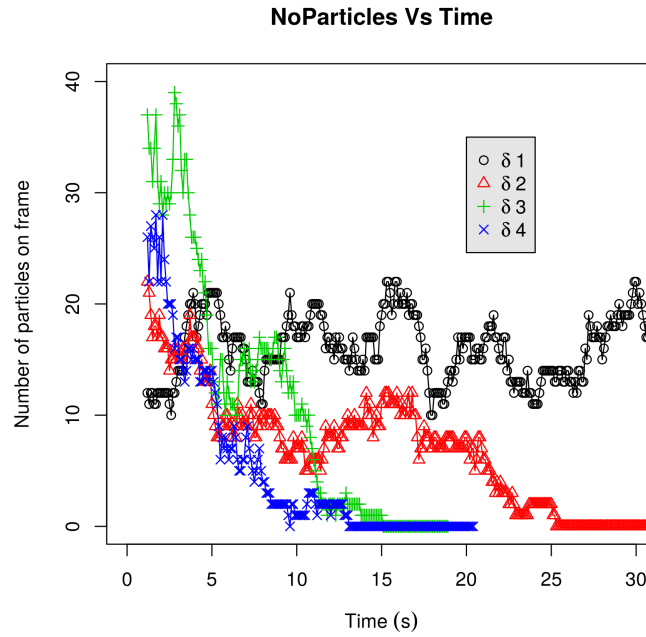
Figure 4.15: Number of particles on frame for four different potential profiles: $\delta1$,$\delta2$, $\delta3$ and $\delta4$. As δ increases the slope of the long range potential it also increases the particle's velocity. Each increase in the long range potential slope reduces the time it takes for particles to leave the field of view. The number of particles in the $\delta1$ profile is half the real value in order to get a better display of the four conditions together. Each δ represent a different experiment and hence a different starting number of particles in frame due to random variations in the initial concentration of polystyrene beads.

(a) X position vs Time

(b) X velocity vs Time
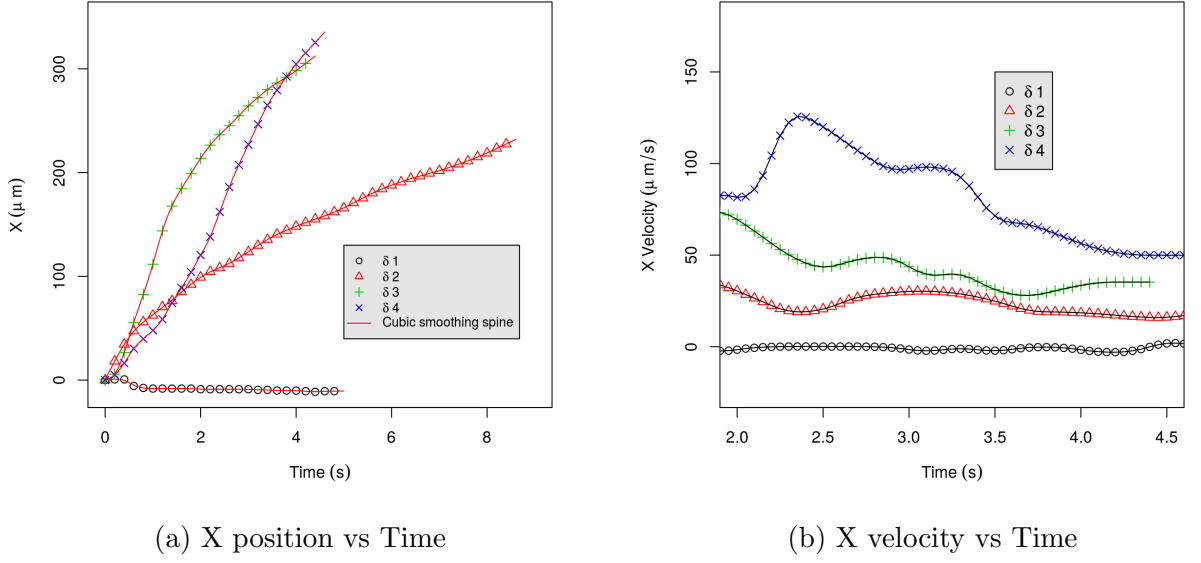
Figure 4.16: (a) Example of X coordinates versus time for a particle experiencing different potentials profiles: $\delta 1$, $\delta 2$, $\delta 3$ and $\delta 4$. As we can see, $\delta 1$ shows no change in the x coordinate as the long range potential fails to move the particles out of the local minimum. On the other hand, increase the particle's velocity steadily. (b) The corresponding X velocity for each one of the four profiles. As we can see there is a steady increase the particle's velocity as we increase δ.

(a) Y position vs Time
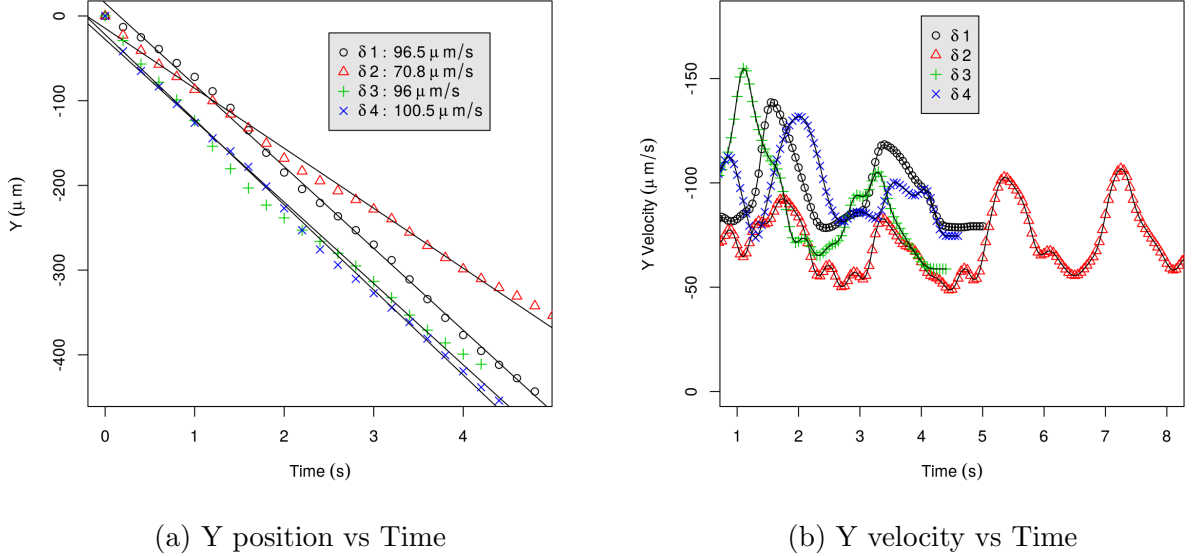
(b) Y velocity vs Time

Figure 4.17: (a) The direction of fluid flow is in the Y direction. Here we have an example of Y coordinates versus time for a particle experiencing different potentials profiles: $\delta 1$, $\delta 2$, $\delta 3$ and $\delta 4$. (b) The corresponding Y velocity for each one of the four profiles. As we can see, the particles move in the Y direction with a velocity that corresponds to the fluid flow. However, there is some fluctuations due to the particles crossing through local minimum and maximums of the long range potential landscapes.

Fig.4.16 a we can see the x-position of each particle. The tracking starts from the moment the electric fields are activated to several seconds later, considering the particle's initial position as the origin. For $\delta 1$, particles just fall into the closest potential well and remain in it indefinitely; the potential wells are located in between electrodes due to negative dielectrophoresis. The x-velocity is zero for the whole trajectory, Fig.4.16 b. For $\delta 2$ we have a situation in which a particle is not constrained to the local potential well anymore, as the particle is released from it and moves down the main potential slope reaching a final x-velocity around 20μm/s. In this situation is also interesting to notice small fluctuations on the position's slope(velocity), see Fig.4.16 4.16a, as the particle moves through smaller potential wells. For $\delta 3$ and $\delta 4$ potential profiles, we have smoother trajectories and faster final velocities in the x direction. The local potential wells get smaller and the long-range potential slope higher; reaching about 40 and 60μm/s on $\delta 3$ and $\delta 4$ respectively, Fig. 4.16 b. In Fig.4.17 we have the effect of different potential profiles in the movement of particles in the Y direction, which corresponds to the direction of the fluid flow. It is interesting to notice that we have what seems to be regular fluctuations in the velocity of particles in the Y direction, see Fig.4.17b. This is probably due to the change in the particles' velocity as they cross through local minimums and maximums of the long-range potential landscapes. Particles seem to be travelling slower when moving close to the local minimums of the potential landscapes.

4.4.3 Particle concentration and particle sorting.

To illustrate how effective this technique is for particle sorting and particle concentration we had extended the $\delta 1$ potential profile many times over to cover the whole dimensions of the microfluidic channel. Because of the freedom and flexibility allowed by the device for shaping the long-range potential and depth of the wells we have limitless possibilities for experimentation. The first case refers to a ∨-shaped potential profile for concentrating a mixture of polystyrene beads of 5, 3 and 1μm in diameter. For this first example, we have programmed a negative slope for a long-range potential covering the whole distance from the left edge of the channel towards the centre; at the same time another long-range potential is created but this time with positive slope and spreading from the center towards the right edge of the channel, see Fig.4.18. This intends to demonstrate the effectiveness of $\delta 1$ profile for concentrating 5, 3 and 1μm-diameter polystyrene beads towards the center of the channel, see Fig.4.18.

On the second example, we have a long range ∧-shaped potential profile, also covering the whole dimensions of the microfluidic channel, see Fig.4.19. However, here we are sorting 10 micrometres particles from a homogeneous mixture of polystyrene beads of 10, 5 and 1 micrometres in diameter. For this case we have made some changes on the potential profile. To begin with, the potential wells are wider; when activating electrodes we are skipping

one electrode each time. Also, this time we are using $\delta 2$ instead of $\delta 1$, as this makes the sorting faster for these particular potential wells. In this situation 10μm-diameter particles are unable to scape the local minimums of the long range potential landscapes, in this way just moving in the direction of fluid flow, see Fig.4.18. On the other hand, 5, 3 and 1μm-diameter particles experience a shallower potential wells due to the decreased negative DEP force which has a cubic dependence with the particle's radius, see Eq.4.3.

In Fig.4.20 we have another $\wedge$-shaped potential profile covering the whole microfluidic channel; however, this time we use a $\delta 3$ profile and a mixture of 5 and 10μm-diameter particles. Also we are skipping two electrodes at a time; we have found that this type of profiles is very effective for particle sorting. If we define the relative concentration of 10μm-particles as $RC_{10} = 100 \times N_{10}/(N_{10} + N_5)$, where N_{10} and N_5 are the number of 10 and 5μm-diameter particles on frame respectively, then we have a initial RC_{10} value of 6% but after 40 second this value increases to 90%. Also, when taking into account the concentration of particles, flow rate, and dimensions of our microfluidic channel we have a sorting rate 225 particles/s for these particular conditions.

As we can see, the possibilities are many. The electronic device is truly programmable in this sense. New conditions and new potential shapes can be implemented by just sending a new instruction through a mobile phone application. Another great advantage of this technique is that it can be extended to millimeters or even several centimeters increasing the throughput many times over; which would make it ideal for bio-particle sorting and enrichment in real medical diagnostic applications.
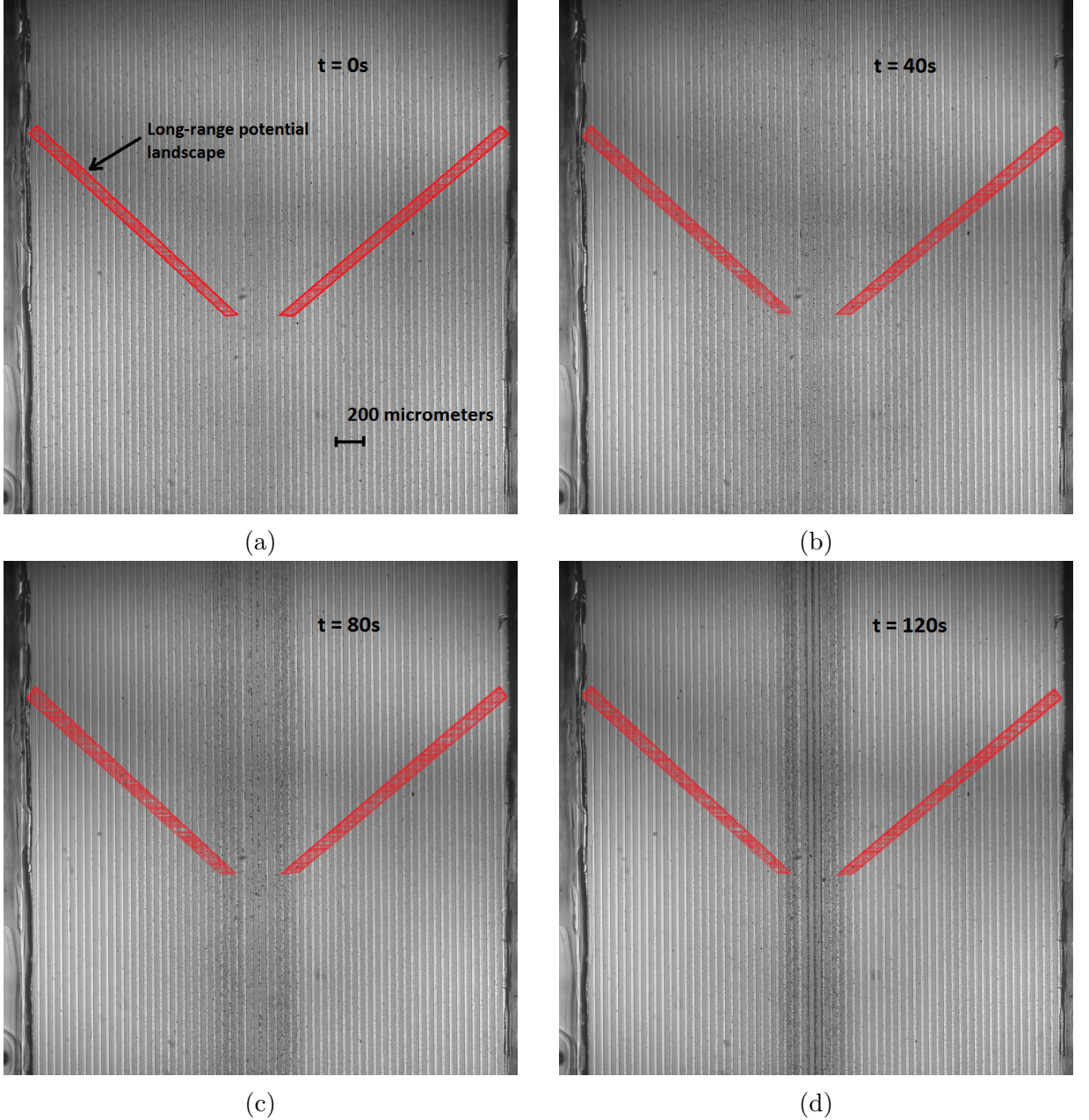
Figure 4.18: ∨-shaped potential profile covering the whole microfluidic channel. In red we have a graphical representation of the tailored long range potential landscapes used to concentrate a mixture of polystyrene particles towards the center of the microfluidic channel. The local minimums of potential are not deep enough to trap the beads. All the beads move up following the fluid flow at the same time they also migrate towards the global minimum of potential, which this time was designed to be at the centre of our microfluidic channel. For this experiment a $\delta 1$ profile and a mixture of 1, 3 and 5 μm diameter particles where used. The volumetric flow rate was set to 1μL/min with a 15kHz sinusoidal wave for which V_{init}=14Vpp, conductivity of the medium = 26μS/cm, and Δt=300μs. Particles travel from the bottom to the top in the image. The purpose of this is to illustrate the effectiveness of $\delta 1$ potential profile for particle concentration.
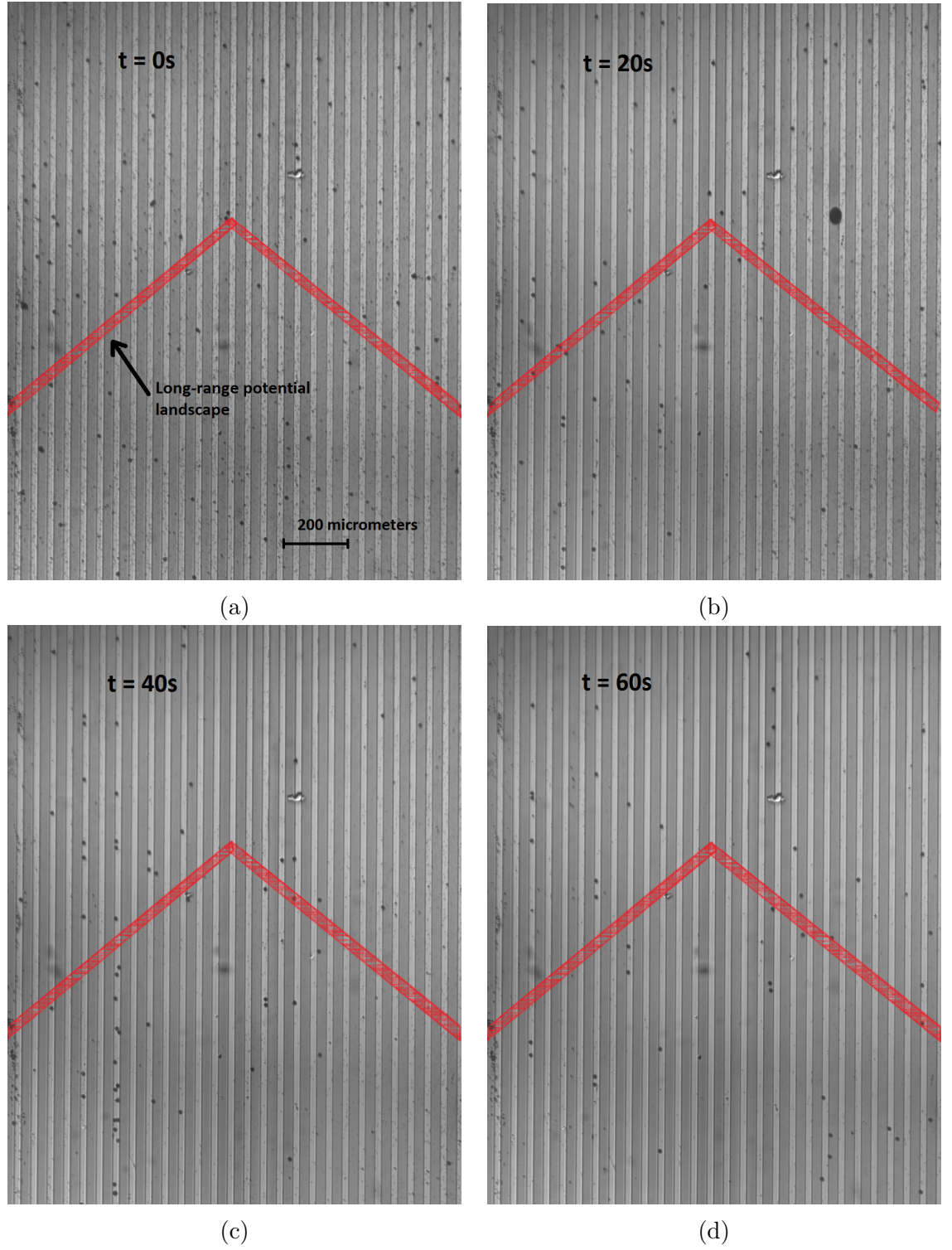
Figure 4.19: ∧-shaped potential profile covering the whole microfluidic channel. In red we have a graphical representation of the tailored long-range potential landscapes used to sort a mixture of 1, 5 and 10 μm diameter beads. We can see from the sequence of images how the 5 and 1 micrometres beads move down the long-range potential slope towards the global minimum, which this time is on the sides of our channel. After a few seconds, only 10 micrometres particles remain; they are being trapped into the local minimums of the tailored potential at the same time they move up following the fluid flow. For this experiment a $\delta 2$ profile and a mixture of 1, 5 and 10 μm diameter particles where used. The volumetric flow rate was set to 1μL/min with a 15kH sinusoidal wave for which V_{init}=14Vpp, conductivity of the medium = 32μS/cm, and Δt=300μs.
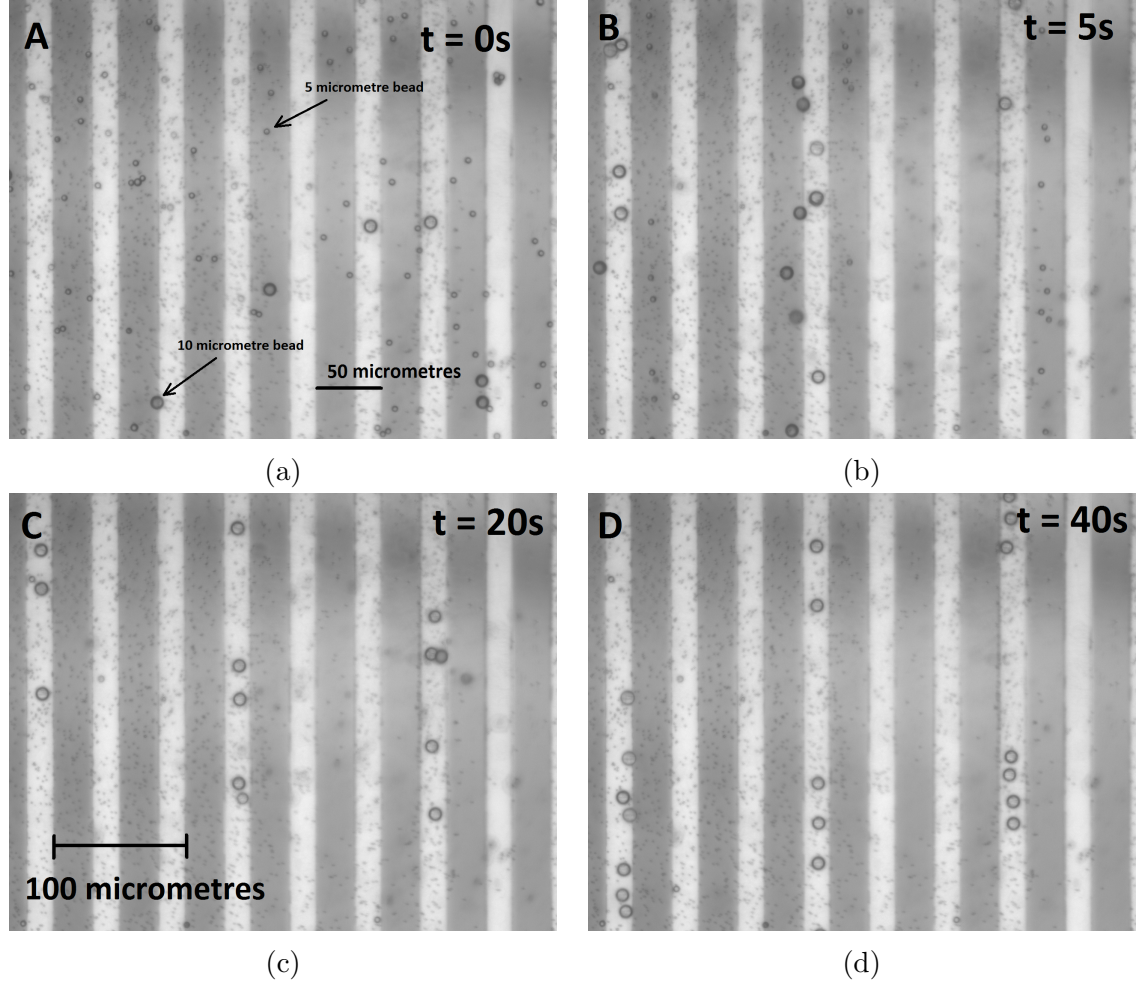
Figure 4.20: Another ∧-shaped potential profile covering the whole microfluidic channel. For this experiment we used a $\delta 3$ profile and a mixture of 5 and 10μm-diameter particles. The volumetric flow rate was set to 1μL/min with a 15kHz sinusoidal wave for which V_{init}=17Vpp, conductivity of the medium =98μS/cm, and Δt=500μs. The particles travel from the bottom to the top in the image. This time we are skipping two electrodes at a time. The purpose of this experiment is to illustrate the degree of freedom we have to generate different long range *potential landscapes*. At the begining we have a mixture of 5 and 10μm particles but after 40 seconds almost every single 5μm particle has moved to the right towards the global minimum of potential and out of frame. Please note there are 1-micron particles and a few 5-micron particles attached to the substrate.

4.4.4 Numerical simulations
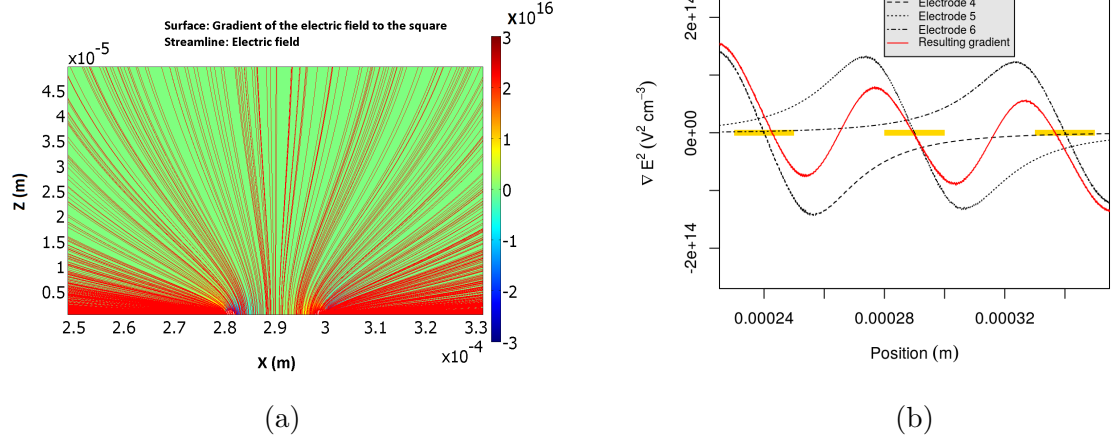
Figure 4.21: Simulation results: a) The resulting gradient of the electric field squared and electric field in the liquid when activating a single electrode, the field lines are shown and the gradient by a surface plot. b) The resulting gradient of the electric field squared at 20 μm high when taking into account a central electrode and the two immediate neighbors.

In order to have a proper understanding of the physics behind this technique we have developed a computational model that allowed us to gain more insight into the mechanisms responsible for the separation and concentration of micro-particles of different size. We made extensive use of 2D numerical simulations (COMSOL multiphysics 3.5a). First we simulate the electric field generated by each individual electrode for each activation sequence on the electrode array. This means we have simulated each individual electrode under the right condition for our system taking into account the changes in voltage for each one of the considered profiles: $\delta1$, $\delta2$, $\delta3$ and $\delta4$. After this we proceed to compute the gradient of the electric field squared ∇E^2 for each electrode, as this quantity is in direct proportion to the DEP force we would expect on a particle. After getting the gradient of the electric field squared for each electrode in each one of the delta conditions, we make an estimation of the DEP force generated by each electrode on a polystyrene particle of a specific size using Eq.4.3. The next step is to compute the average of this DEP force taking into account all electrodes for each one of the delta values. These averaged values are the ones we use for the numerical computation of the potential energy profiles.

In order to illustrate the individual contribution of each electrode to the DEP force field we will consider the gradient of the electric field squared ∇E^2 generated by only three metallic electrodes. In Fig.4.21 a we have the electric field E generated by a single electrode. On the other hand, in Fig.4.21 b we have the ∇E^2 for three neighbor electrodes

and the the resulting gradient a particle would experience as a result of the contribution of the field generated by the three of them.

As mentioned previously, the technique relies on a competition between pulsed DEP forces which can be modulated through voltage, pulse duration, frequency and inter-electrode separation. When a single metal electrode is activated for a short time interval a non-uniform electric field E is generated between the electrode and the grounded ITO glass. When this electric field interacts with a spherical particle made of a material with electrical permittivity ϵ_p and radius r it will experience a DEP force given by Eq.4.3 The resulting gradient of the electric field to the square ∇E^2 was independently simulated for each individual electrode in order to compute the overall effect due to the DEP force contribution of each individual electrode. After calculating the resulting force we proceeded to numerically compute the potential energy profile a polystyrene particle of 10 micrometers in diameter would experience at different heights and under different potential slopes, see Fig.4.22. To generate plots of potential energy $U(r)$ we use as a function of the position r we compute the cumulative integral of F with respect to r using trapezoidal numerical integration. As we can see in Fig.4.22, it is possible to shape the resulting ∇E^2 through the right combination of electric gradients.

$$U(r) = \int_0^r F \cdot r' dr' \tag{4.7}$$

The generated tailored potential allow us to make selective lateral sorting of particles by constraining a particular kind to the local minimums of potential and displacing later-ally(in the x direction) a different kind of particles; this is achieved at the same time all particles move forward in the direction of the fluid flow. The velocity in the x direction can be controlled by adjusting the long range slope of the tailored potential through the delta values δ.
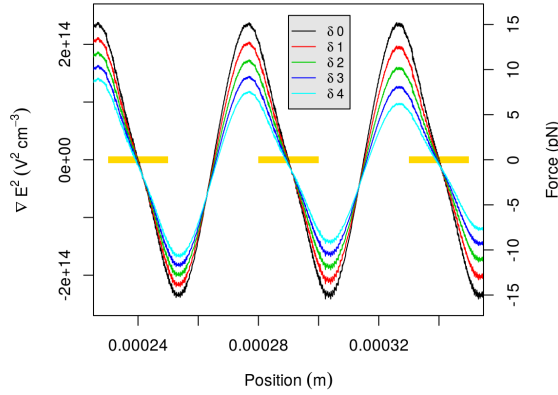
(a) DEP force and ∇E^2 at 15 μm high.
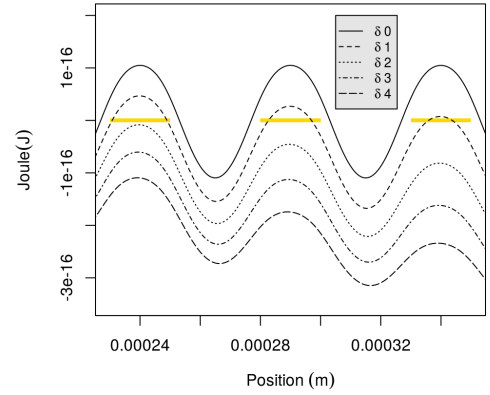
(b) Potential energy profile at 15μm high.
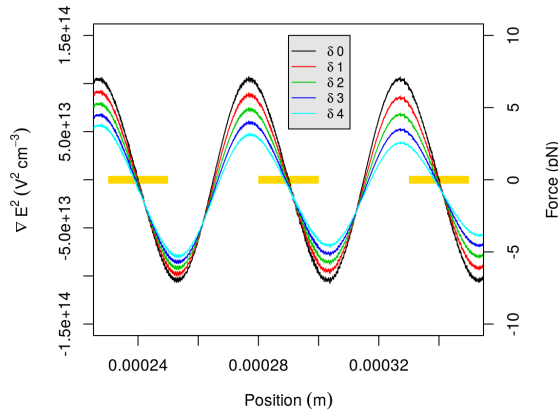
(c) DEP force and ∇E^2 at 20μm high.
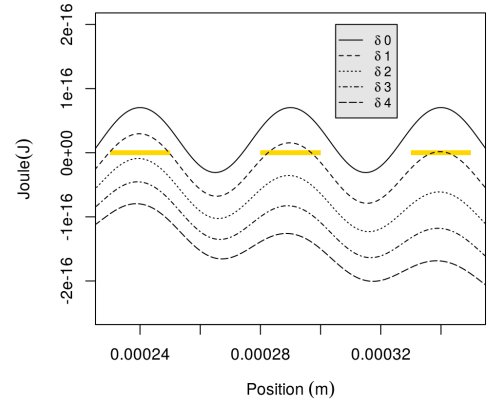
(d) Potential energy profile at 20μm high.
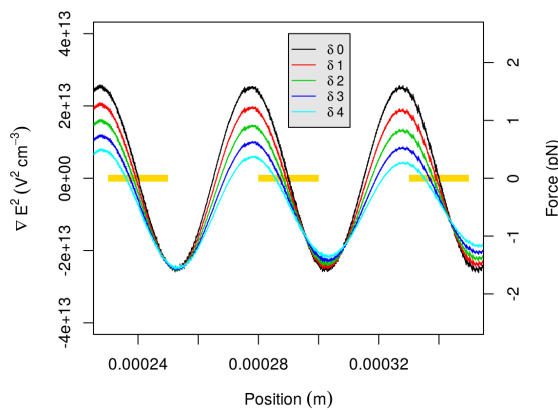
(e) DEP force and ∇E^2 at 30μm high.
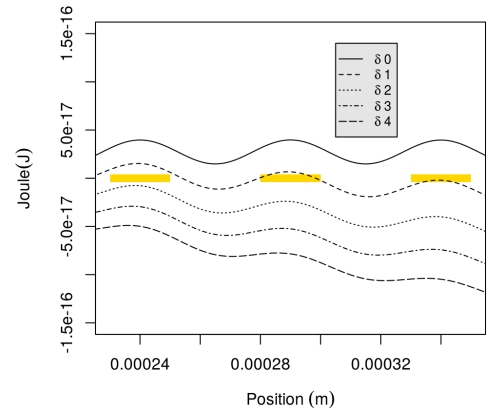
(f) Potential energy profile at 30μm high.

Figure 4.22: Simulation results for 15 μm high: a, b; 20 μm high: c, d; and 30 μm high: e, f. The values for δ, inter-electrode spacing, Δt, and V_{init} give us total freedom in shaping the resulting gradient of the electric field to the square ∇E^2.

4.5 Experiments with diluted human blood
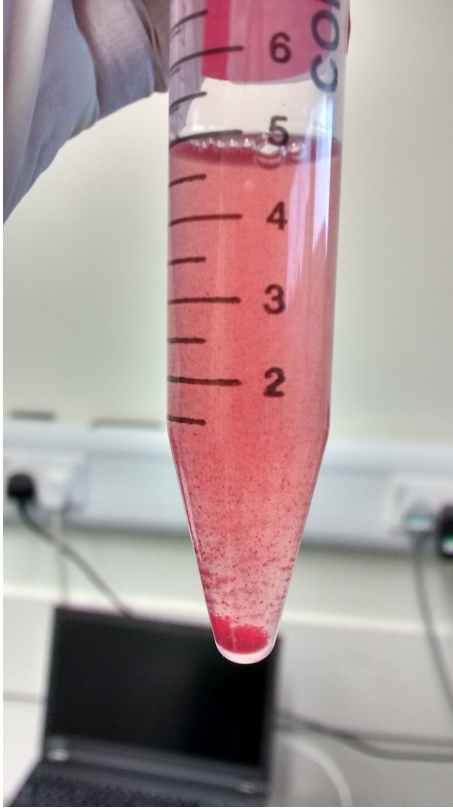
Figure 4.23: Red blood cell agglutination in our prepared DEP buffer.

We have chosen red blood cells for the testing of our sorting device on living cells. As we already mentioned previously, DEP techniques require a low conductivity supporting medium. Typically a medium containing 25% or less ions than we would normally found in physiological conditions [34]. In addition to this, the osmolarity of the suspending medium should also be compensated to physiological levels to avoid cell damage. For all our experiments the DEP supporting medium was prepared containing 9% sucrose and 0.3% dextrose [34].

Before even starting working on our DEP experiments we realized there was a few challenges related to the manipulation and preparation of the blood samples for our DEP experiments. The first of these challenges was cell agglutination. As we can see in Fig.4.23; cell agglutination is a serious problem when trying to suspend the blood sample in our DEP buffer(1.0% v/v). The agglutination of red blood cells happens in a minute or less. Our human blood sample was obtained from a healthy 24 year old male donor[Cambridge Bioscience]. K2-EDTA Anticoagulant was also added.

We tried several things to overcome the problem; however, the solution that best worked for us was to first pipette $50\mu L$ of whole blood into a tube containing 5mL of phosphate buffered saline(PBS), gently mix the fluid and incubate at room temperature for about 10 minutes. After this we centrifuged the mixture at $200\times g$ for 5 minutes at room temperature. We aspirated the supernatant leaving approximately $500\mu L$ to avoid disturbing the pellet. Gently remixed the cells and the remaining fluid, after that we added 4.5ml of our DEP buffer. We gently mixed the fluids and centrifugate again at $200\times g$ for 5 minutes. After doing this, we once again aspirated the supernatant leaving approximately $500\mu L$ and gently re-suspend the cells in our DEP buffer adding approximately $4.5\mu L$ of our prepared buffer. Using this procedure the conductivity of our sample was set to 16.6mS/m without observing agglutination of red blood cells.

The second problem we faced during these experiments was cell attachment to the device substrate. A significant number of cells get attached to the electrodes and glass

even when the electronic device is deactivated. In order to deal with the problem we decided to make use of our image processing system, which was introduced in Chapter 3, to analyze our video sequence. We have applied dynamic background subtraction to obtain an image sequence of only the moving particles, in this way neglecting the ones that get attached to the device substrate, see Fig.4.24a and4.24b. Fig.4.24a and Fig.4.24b corresponds to an unprocessed image and its binary image foreground respectively. For these experiments we have applied a ∨-shaped potential, just like the one represented in Fig.4.18, to concentrate RBCs towards the center of the microfluidic channel. The conductivity of our prepared DEP buffer was set to 16.6mS/m, with a volumetric flow rate of 1μL/min. The applied AC signal was a sinusoidal wave of 50kHz for which V_{init}=16Vpp a pulse duration Δ=300μs. The reason we chose the mentioned value of frequency(50kHz) is that according to Clemens Kremer et al [48] for that particular value of frequency should expect is negative DEP. We should keep in mind that our device relies solely on negative DEP for particle concentration and sorting.

In Fig.4.24b we have the extracted foreground image of the unprocessed frame shown in Fig.4.24a; these two images correspond to a time just 3 seconds after the activation of the ∨-shaped long range potential. As we can see, the extracted foreground image give us valuable information about the distribution of RBCs throughout the whole frame. This will help us better appreciate the effect of the applied tailored potential.

On Fig.4.24b, Fig.4.24c and Fig.4.24d we have the resulting binary image for the extracted foreground at 3, 75 and 100 seconds, respectively. As we can see from these results, first the RBCs fall into the local minima and form lines along the electrodes and then as time progresses they follow the long range potential landscape towards the center of the channel. The concentration of particles towards the center of our microfluidic channel is not as complete as for the case of polystyrene beads. There is a considerable proportion of RBCs that seem to be unresponsive to the generated long-range potential. However, we can also notice there is a sizable fraction of particles that do react to the potential and concentrate towards the center. In Fig.4.25a, Fig.4.25b and Fig.4.25c we have a (side-to-side) profile plot of the pixel values for Fig.4.24b, Fig.4.24c, and Fig.4.24d respectively. The higher the pixel values the more concentration of particles we have.

In Fig.4.24b and Fig.4.25a we have the distribution of particles 5 seconds after the activation of the ∨-shaped long range potential. We can observe an uniform distribution of particles towards the whole frame. After 70 seconds the distribution of particles looks like shown in Fig.4.24c and Fig.4.25b. It is clear that this time we have two maxima for cell concentration; the main one in the center of our channel and another one around pixel 635. We believe this second maximum corresponds to an faulty electrode(inactive one) which generates a deeper local minimum that most particles can not overcome, therefore increasing the concentration at that location. Finally, we have Fig.4.24d and Fig.4.25c.
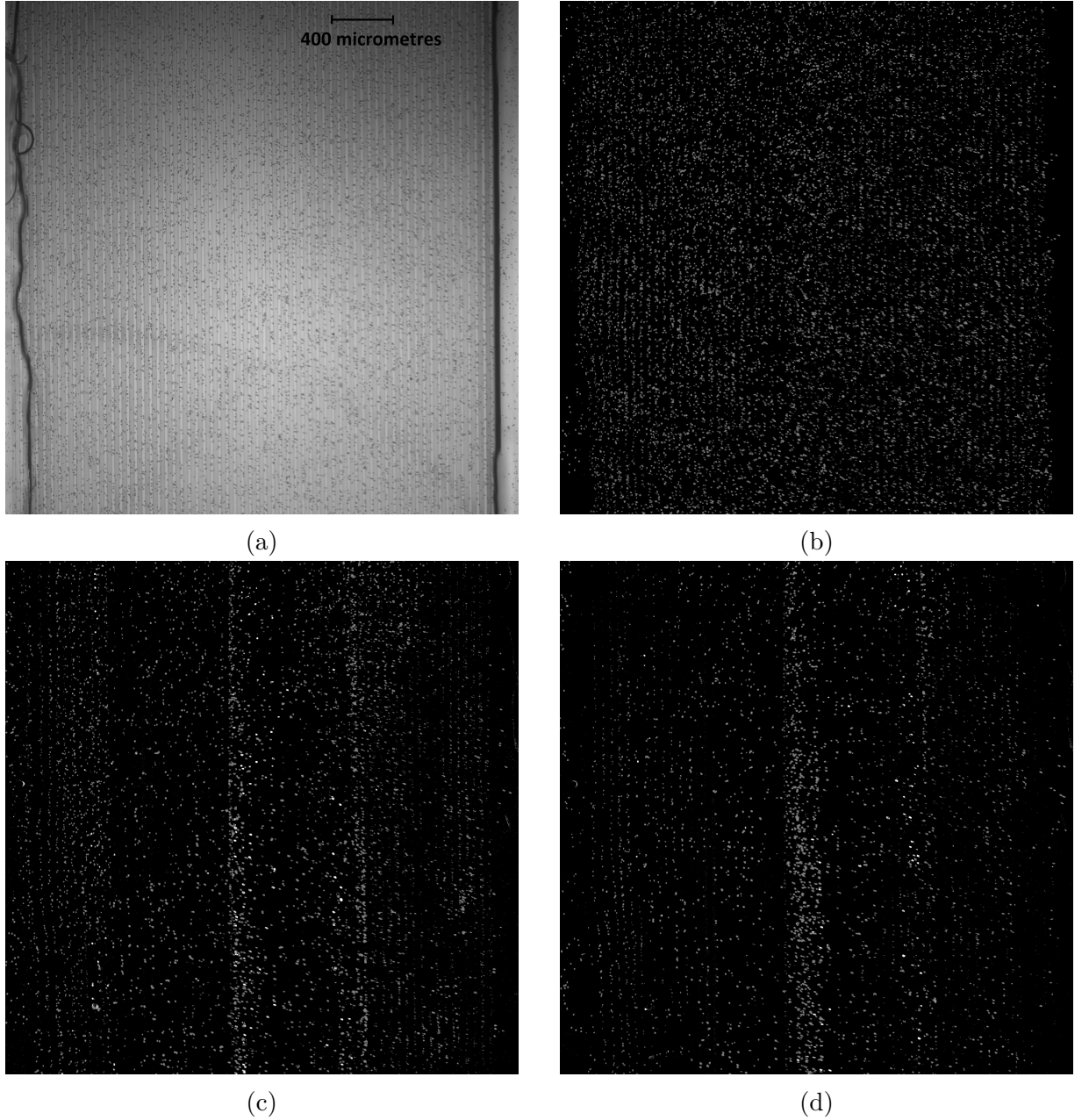
Figure 4.24: A ∨-shaped potential profile covering the whole microfluidic channel is applied to diluted whole blood on DEP buffer with a 16.6mS/m. The volumetric flow rate was set to 1μL/min with a 50kH sinusoidal wave for which V_{max}=16Vpp and Δ=300μs. Particles travel from the bottom to the top in the image on a $\delta 2$ potential profile. a) Unprocessed image of diluted blood flowing in our microfluidic channel at t=3s. b) Foreground binary image at t=3s. c) Foreground binary image at t=75s, d) Foreground binary image at t=100s.

These ones correspond to the distribution of particles 100 seconds after the activation of
the ∨-shaped potential. As we can appreciate on the figure, this time the profile plot
shows a clear increase of the particle concentration towards the center of the channel.
From these results is easy to see that we have indeed achieved some degree of concentra-
tion of cells; however, these results are not as satisfactory as the results we got from our
experiments with polystyrene beads. We believe a higher efficiency could be achieved by
increasing the strength of the generated electric gradients; which could be achieved with
relative ease by modifying the system so that a higher values of V_{init} could be programmed.
As in our device the field is between a bottom electrode and the ITO on top, the field
across a cell is small compared to devices where all the electrodes are on the bottom; we
believe we could use a higher total potential difference. We also believe this technique has
some real potential for cell concentration and sorting of particles and it worth continuing
perfecting/adapting it towards the development of a reliable and useful system.

(a)

(b)

(c)
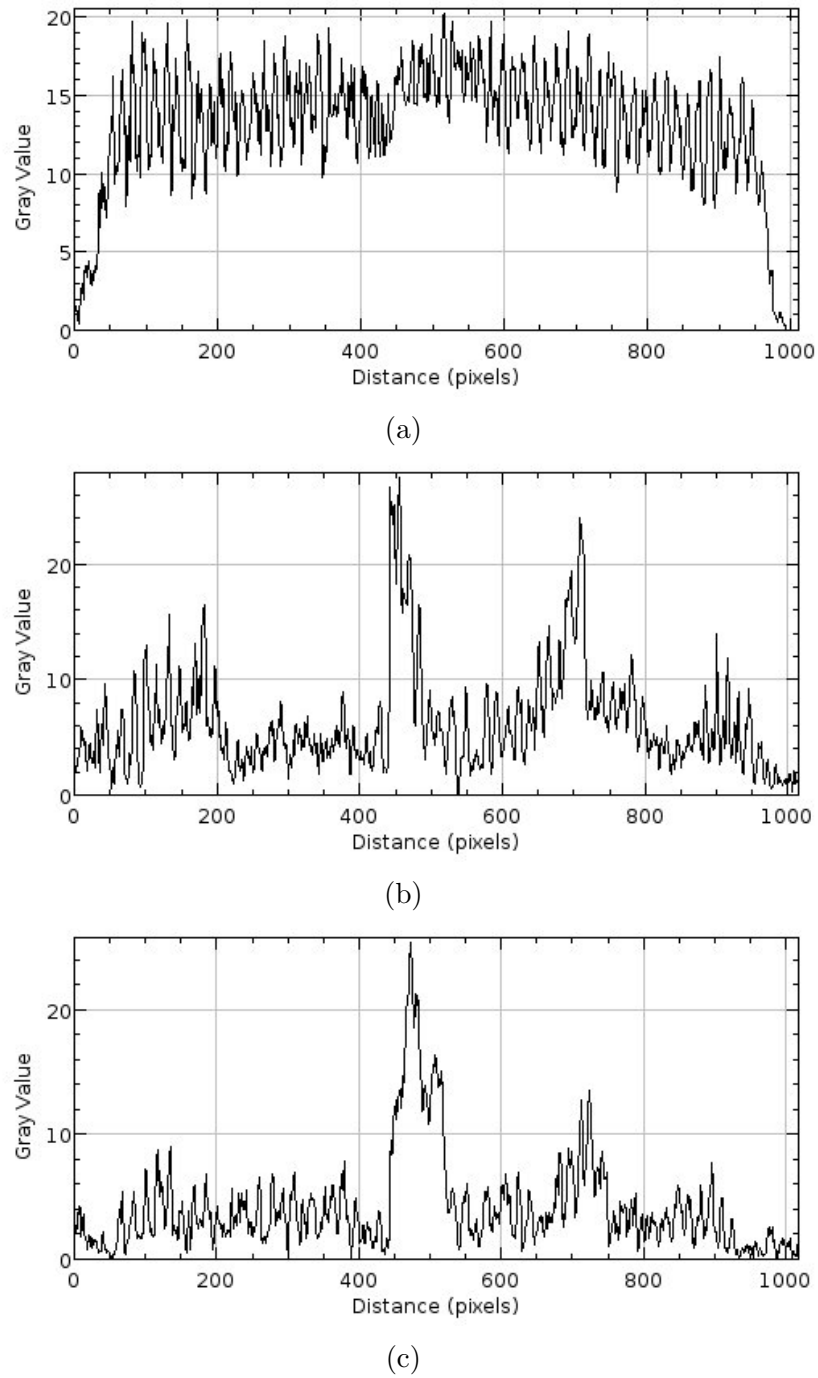
Figure 4.25: Pixel value profile for the obtained foreground binary images at three different times. The size of the frames is 1024×1024 pixes where pixel 0 and pixel 1024 correspond to the left and right edge of our channel respectively. a) 3 seconds after the activation of the ∨-shaped potential, the pixel value profiles shows a uniform spread of cells. b) 75 seconds after shows two maxima corresponding to the regions of maximum cell concentration, and c) 100 second after where we have a single maximum corresponding to a higher concentration of cells at the center of the microchannel.

Chapter 5

Conclusions

The work I have done during my PhD is divided into two main parts. In Chapter 3 we work towards the development of a computer vision system for aiding in the tracking and identification of micro-particles of interest through the use of normal video microscopy. In Chapter 4 we develop an all-in-one continuous flow DEP based micro-particle separator which uses a system of addressable planar metal electrodes to generate tailored potential landscapes.

In this chapter, we present our general conclusions for both parts.

5.1 Computerized Bio-particle Identification

We successfully developed a stand-alone image processing tool that can simultaneously identify, track and count multiple micron-size particles or cell types using normal video microscopy and without any biomarker. First, we investigated the effectiveness of only the particle's colour histogram as a predictors using some real data, see Fig.3.16. Subsequently, we did the same for the particle's size, see Fig.3.18 and Fig.3.19. For colour histogram comparison we used three different metrics: Bhattacharyya, Chi-square and Correlation, see Fig.3.16. From the obtained results we concluded that these two properties of particles are indeed useful predictors in our implementation. Moreover, we have taken this technique one step further. In addition to colour histogram and size, we have carefully selected and implemented a set of thirteen extra continuous predictors of different nature and apply a machine learning algorithm(SVM) to this information. The goal was to develop a system that is robust and efficient in the detection, tracking and identification of cells without any kind of bio-marker and under non-ideal conditions, see Fig.3.20.

As it was already mentioned previously, our algorithm makes use of a Gaussian Mixture Model for background subtraction. The purpose of this was to generate a background model capable of incorporating changes; which also enhances the segmentation of particles even under a fair amount of noise and debris. For multi-particle tracking instead of focus-

ing on special features of each particle, our algorithm tracks the centroid of each particle. Each particle is treated as a whole object with its own identity and characteristics.

The image processing used for feature tracking and identification requires several steps and the fine-tuning of some parameters. In our particular application, the main steps involved during the micro-particle tracking and recognition are: static background subtraction, apply morphological operations, image segmentation, particle tracking, feature extraction, training of the pattern recognition system, classification and image retrieval. Each one of these steps has its own unique challenges to overcome. For example, during multiple-particle tracking, the program has to take into account different possible scenarios, like particles overlapping or the formation of clusters. Also, for the training of our system, we used a diluted blood sample with an increased concentration of WBC. The set of digital images used for training contain 14 white blood cells and 1640 non-white blood cells. The later was a combination of red blood cells, platelets, debris and clusters. These images are our training dataset and each one of these particles is manually labelled using the corresponding identification(ID) number our software assigned to each particle. When testing our system for the identification and counting of white blood cells we found 100% positive classifications that are correct. The total number of frames in our testing dataset was 657. The number of identified white blood cells was 18 from a total of 5953 detected particles including platelets, white cells and clusters. The processing time was 48884.5 seconds in a 64-bit Lenovo(CORE i5) laptop with 4GB RAM memory.

We have developed a C++ application that is well commented, structured and implemented. It performs well even for non-ideal imaging conditions, see Fig.3.15, and has been shown to be effective in the tracking, identification and retrieval of the targeted particles. This software makes the counting of particles and the computation of individual trajectories, velocities and accelerations easy and fast as we have access to the identification number(ID) and position of all successfully tracked particles at all times. If the reader is interested in the full details of any aspect of our application, he/she could refer to the original source code written in C++; which is properly commented at every step.

5.1.1   Central Advantages

1. Capable of the simultaneous tracking and identification of particles as they flow in a microfluidic channel.

2. Our technique only applies standard optical microscopy, without the use of any other technique to enhance cell contrast e.g. selective dyes.

3. Capable to deal with background changes. Even though the technique has its limitations, we have succeeded in generating a useful background model able to incorporate changes in background e.g. cells and debris attachment to our bottom substrate.

4. One of the main strengths of our software is its versatility. It can be used to detect and locate any kind of micro-particles; our group of predictors is able to extract different kinds of valuable information, which is well suited for particle identification under different non-ideal circumstances. However, the performance of this application depends greatly on the training process. In order to avoid having too many false identifications, we need a big and high-quality training set. In most applications of systems of this kind, the training dataset consists of thousands of instances of the target object.

5.1.2 Limitations

1. The preparation of training data is a complex and time-consuming process. For our current case; which involves the detection of white blood cells from a mixture of white blood cells, red blood cells, platelets and debris, the preparation of training data requires the manual labelling of particles in a group of high-resolution images obtained using normal video microscopy. This individual classification of particles is possible due to the capability of our system to give an identification number to each detected particle in a video sequence.

2. It takes about 74.4ms to process every single frame(1024 X 768 pixels) in a video sequence in my 64-bit Lenovo(CORE i5) laptop with 4GB RAM memory. This is due to the many image processing steps required for image analysis. It takes about 49 seconds to complete the image processing of the 657 frames from the experiment shown in Fig.3.20. Even though this processing speed is enough for laboratory conditions and testing we believe that further investigation is needed to optimize the different image processing steps in order to create an application that is fast enough for use outside the laboratory.

We believe that our approach to background subtraction, multi-particle tracking and our selection of predictors have a potential for bioparticle detection and identification in video microscopy and without the use of biomarkers or any other kind of physical aid for image enhancement.

5.1.3 Future work recommendations

- The training of our system requires sufficient amount of labelled data. There is no clear answer to how much training data is needed to achieve good predictive performance. As already mentioned previously, the right amount of training data must be discovered through empirical investigation taking into account how accessible that training data is for each particular case. For our particular application(WBCs detection and counting), the preparation of labelled data is a complex and time-consuming process. It requires the preparation and processing of diluted blood samples with an increased concentration of white blood cells and subsequently the manual labelling of each cell. Even though the results obtained using our trained data set were satisfactory we believe that more investigation is needed to properly capture the relationship between input and output features.

- Our software uses a kernel function for aiding in the classification of classes. In our work, we used the Radial Basis Function(RBF) kernel to map data points into a higher dimensional feature space; however, the choosing of this particular kernel was done following a trial and error methodology. Moreover, we needed to tune the kernel parameters in order to achieve a good performance in our classifier application. We suggest exploring other kernel options and different parameter in order to see if there is any further improvement in performance.

- A better user interface(front end) is needed. Currently, our software runs only on a LINUX operative system which requires the installation of several external libraries(OpenCV). It would be very desirable to have a binary file that is able to run on any computer with a Windows operative system.

5.2   Tailoring the potential across a microfluidic channel for particle separation in a portable device

Even though several technologies have been developed over the years that allow the manipulation and separation of bioparticles in aqueous solutions dielectrophoresis still standout due to its label-free nature to manipulate neutral bioparticles. The magnitude and direction of the DEP force are in direct relation to the particles electric properties, internal morphology, size and shape, see section 1.3. The increasing popularity of lab-on-a-chip(LOC) techniques in recent years have contributed to making DEP widely researched for particle sorting, focusing and patterning. Although several successful dielectrophoretic devices have been developed previously, the instruments required for operation are bulky and complex and the throughput of DEP-based devises in still low compared with standard techniques. Moreover, most of them are labour intensive and require tags to identify target particles. This manual, multi-step techniques require a laboratory dedicated to the task and technicians trained in the technicalities. Fortunately, the development of microfluidic platforms is heading towards the integration, miniaturization and automation of these techniques. The development of an integrated and intelligent DEP micro-device will achieve a greater control and performance in particle concentration and sorting. A single all-in-one device could facilitate practical applications.

In this work, we have developed a portable, continuous flow DEP based electronic micro-particle separator capable of tailoring the energy potential particles experience across the entirety of a micro-channel. The device is able to produce lateral sorting and concentration of a mixture of polystyrene beads as they move through the channel. This is achieved by generating a lateral force field in the entire micro-channel that is able to trap/release particles of specific characteristics in the local minima of the **tailored long-range potential**, see Fig.4.22. We present simulation results to illustrate the physics behind this new technique along with experimental results demonstrating the concentration and separation of polystyrene beads of different size. We have found experimentally that our technique allows us to control the long-range potential energy slope and the depth of its local minima using negative DEP exclusively; all of which is controlled through software. This makes it possible to selectively trap the targeted particles in the local potential wells and at the same time unwanted particles are moved down the long-range energy potential slope, see Fig.4.18 and Fig.4.19.

The programmable nature of our device gives us endless possibilities for the design of the long-range potential landscapes. For example, using a potential profile which skips two electrodes at a time we were able to continually sort a mixture of 5 and 10-micrometre diameter polystyrene particles in suspension. The relative concentration of 10-micrometre

particles was increased from 6% to 90% in 40 seconds, see Fig.4.20. Under these particular conditions, we counted the initial and final concentration of particles in a frame. Subsequently, taking into account the flow rate(1μL/min) and dimensions of our fluidic channel we have achieved a sorting rate of 225 particles/s. However, we must have in mind that there is an important constraint in the size of particle we can reliably detect and count using our microscope setup. Due to the thickness of the top microscope slide in our device(1 mm thick), we can not reliably detect and count particles that are smaller than 5 micrometres in diameter. This is because the thickness of our microfluidic device does not allow a proper focusing of particles using the 40X objective in our microscope. In addition to experiments with polystyrene beads, we also experimented with diluted blood samples for testing our sorting device on living cells. After overcoming the problem with cell agglutination and setting the conductivity of our sample to 16.6mS/m we discovered that a significant number of cells got attached to the electrodes and glass in our substrate. In order to deal with the problem, we applied dynamic background subtraction in order to obtain an image sequence of only the moving particles, in this way neglecting the particles that get attached to the device substrate, see Fig.4.24. We applied a V-shaped potential in order to concentrate all particles towards the centre of our microfluidic channel. As we can see in the sequence of images shown in Fig.4.24, there is a considerable proportion of red blood cells that seem to be unresponsible to our generated long-range potential. However, there is a sizable fraction of particles that do react to the potential and concentrate towards the centre of our microfluidic channel. In Fig.4.25c we start with a uniform distribution of red blood cells at the beginning of our experiment and 70 seconds later we end up with a maximum for cell concentration at the centre of our channel. Even though we have achieved some degree of concentration of cells, the results are not as satisfactory as the ones we got from our experiments with polystyrene beads; however, we believe a better performance could be achieved by increasing the strength of the generated electric field. This could be done with relative ease by modifying the system so that a higher value of V_{init} could be programmed.

We have introduced a new microparticle separation technique. Most continuous and discontinuous DEP microseparators exploit positive DEP force to trap cells in metal electrodes. One of the main disadvantages of this is that cells are frequently damaged by the high gradients formed in the proximities to the electrodes. In addition, cells get attached to the electrodes and it becomes difficult to remove. On the other hand, a controlled low conductivity suspension medium is needed in order to take advantage of the crossover frequency($<$200kHz); a low conductivity medium causes stress and damage to cells. In addition, it becomes impractical to separate cells having less than a 50% difference in their crossover frequencies using negative/positive DEP forces [34]. Our technique is different

in this sense because it does not require the use of positive DEP or a crossover frequency, which must be carefully controlled through the mediums conductivity. We need to re-suspend our cells into a low conductivity buffer but there is a large range of conductivities and frequencies we can work with. Our design takes advantage of differences in the particles size and shape and the magnitude of the Clausius-Mossotti factor, but not its sign. We believe this has great potential for bioparticle concentration and sorting.

5.2.1 Central advantages

1. This novel separation method does not require the use of a cross-over frequency for particle sorting.

2. Our technique does not use positive DEP forces. This represents an important advantage because it is common that cell gets attached to the electrodes and/or damaged by the high electric field gradients generated in the proximities of the electrodes.

3. Our electronic device is truly programmable. It is capable of tailoring the potential energy landscapes through a combination of pulsed electric fields in the entirety of our microfluidic channel.

4. Is an all-in-one portable micro-separator system which includes all the required microfluidic components and electronic elements it needs for particle concentration and sorting in a battery-powered device that is small enough to be portable.

5. Our system does not require the use of buffer flows for particle sorting. Our microfluidic system is very simple in the sense that only requires a single fluid flow which contains the mixture of particles to sort/concentrate.

5.2.2 Limitations

1. We still need to experimentally control the mediums conductivity in order to generate a DEP force that is strong enough to effectively move particles.

2. From our experiments using diluted whole blood, see Fig.4.24, we concluded that the concentration of RBCs towards the centre of our microfluidic channel is not as complete as for the case of polystyrene beads. However, we believe the performance can be improved by increasing the strength of the electric field generated by each individual electrode. We must remember that in our current devices our 64 individual electrodes are powered by a pulsed AC sinusoidal signal that can reach a maximum of 17Vpp. By increasing the AC amplitude we should be able to increase the strength of the negative DEP force generated by the tailored potential.

5.2.3   Future work recommendations

- More experiments with bio-particles are needed. In this work we have shown the sorting and concentration of polystyrene beads as well as the concentration of red blood cell; however, more experiments are needed in order to better understand the strength and limitations of our technique for the concentration and sorting of cells.

- In all our experiments one of the most important problems was the attachment of cells(and polystyrene beads) to the bottom substrate of our microfluidic device. A method for surface modification must be applied to our bottom substrate in order to inhibit cell attachment without compromising cell behaviour and function.

- Increase the maximum amplitude of the pulsed AC signal that is applied to each one of the 64 metal electrodes. Currently, the maximum amplitude of the AC signal is 17Vpp. We believe that by increasing the AC amplitude we could obtain a stronger DEP force which will give us, as a result, a better performance for the sorting and concentration of bio-particles.

Appendices

A Color Representations

```
cv::Mat bgr_image, grey_image; // we declare two cv::Mat data structures
cv::cvtcolor(bgr_image, grey_image, CV_BGR2GRAY); // convert bgr_image to
    grey-scale representation
std::vector<cv::Mat> bgr_images(3); // we declare a vector to store the
    three bgr_image components
cv::split(bgr_image, bgr_images); // split the bgr_image into their componet
     channel images
cv::Mat& blue_image = bgr_images[0]; // store the blue channel in blue_image
```

B Extracting Foreground

```
cv::BackgroundSubstractorMOG2 mog; // The Mixture object used with all the
    default parameters
// extract the foreground object and convert to gray-level image
cv::mog(frame, foreground, 0.01);  // where 0.01 is the learning rate
// in order to differentiate the true moving points from the background we
    apply band thresholding over the gray-level image foreground
cv::threshold(foreground, moving_points, 150, 255, cv::THRESH_BINARY);
cv::threshold(foreground, changing_points, 50, 255, cv::THRESH_BINARY);
// now we subtract the two thresholded frames to get the true foreground
cv::absdiff(moving_points, changing_points, foreground);
```

C Morphological Operations

```
// for our particular application 6X6 structuring element works fine
cv::Mat str_el = getStructuringElement(cv::MORPH_RECT, cv::Size(6,6));
cv::morphologyEx(foreground, foreground, cv::MORPH_CLOSE, str_el);  //
    closing filter with a 6X6 structuring element
cv::morphologyEx(foreground, foreground, cv::MORPH_OPEN, str_el);   //
    opening filter with a 6X6 structuring element
```

D Distance transformation and watershed segmentation

```cpp
    // Eliminate noise and smaller objects
    // Perform the distance transform algorithm for
    // the FIRST segmentation
    cv::Mat dist1;
    cv::distanceTransform(binary, dist1, CV_DIST_L2, 3);

    // Normalize the distance image for range = {0.0, 1.0}
    // so we can visualize and threshold it
    cv::normalize(dist1, dist1, 0, 1., cv::NORM_MINMAX);

    // Threshold to obtain the peaks
    // This will be the markers for the FIRST foreground objects
    cv::Mat first_fg;
    cv::threshold(dist1, first_fg, .5, 255.0, CV_THRESH_BINARY);
    // Create a CV_8U version of the foreground image
    first_fg.convertTo(first_fg, CV_8U);

    // Identify image pixels without objects
    cv::Mat bg;
    cv::dilate(binary, bg, cv::Mat(), cv::Point(-1,-1), 5);
    cv::threshold(bg, bg, 1, 128, cv::THRESH_BINARY_INV);

    // Get the FIRST markers image
    cv::Mat first_markers(binary.size(), CV_8U, cv::Scalar(0));
    first_markers= first_fg+bg;

    // Create watershed segmentation object
    WatershedSegmenter segmenter;

    // Set first markers and process
    segmenter.setMarkers(first_markers);
    segmenter.process(image);

    // Get first segmentation and the region to exclude
    // for the second segmentation

    first_segmentation = segmenter.getSegmentation();
      cv::threshold(first_segmentation, first_segmentation, 150, 255, cv::
    THRESH_BINARY);
```

E   Find Contours

```
// find the contour of ALL the particles
cv::findContours(foreground, // the(input) foreground image
                 contours,   // a vector of contours
                 CV_RETR_EXTERNAL,  // retrieve the external contours
                 CV_CHAIN_APPROX_NONE); // all pixels of each contours

// eliminate too short or too long contours
it_c = contours.begin();
  while (it_c != contours.end()) {
       if (it_c->size() < cmin || it_c->size() > cmax)
       it_c = contours.erase(it_c);
       else
           ++it_c;
  }
```

F   Compute Central Moments

```
// get the moments
std::vector<cv::Moments> mom(contours.size());
for (int i=0; i < contours.size(); i++ )
   { mom[i] = cv::moments(contours[i], false);}

 // get the mass  centers and generate the points from the new frame
 for (int j=0; j < contours.size(); j++)
    {
     commingPoints point;
     point.Xpos = (int)mom[j].m10/mom[j].m00;
     point.Ypos = (int)mom[j].m01/mom[j].m00;
     point.area = mom[j].m00;
     point.status = ``not assigned''; // originally this point is not
    assigned to any previous point
     NewPoints.push_back(point);  // generate a new instance
    }
```

G   Locate Particles

```
// search for each one of the particle's new coordinates
```

```cpp
for(itp = Particles.begin(); itp != Particles.end(); itp++) {
  for (itpNew = NewPoints.begin(); itpNew != NewPoints.end(); itpNew++){
    // only consider the shaped that are directly forward
    if ((itpNew->Xpos < itp->getXpos()) && (-50.0+itp->getYpos() < itpNew
->Ypos) && (itpNew->Ypos < itp->getYpos()+50.0)) {
      searchData point;
      point.dist = std::sqrt(std::pow( itp->getXpos() - itpNew->Xpos,2)
                      + std::pow(itp->getYpos() - itpNew->Ypos,2));
      point.ID = itpNew->ID;
      distPoints.push_back(point);
    }
  }

  // std::cout << "vector size: " << distPoints.size() << std::endl;
    itpDist = distPoints.begin();
    if (distPoints.size()==1){
      itp->setXpos(NewPoints[itpDist->ID].Xpos);    // update x position
      itp->setYpos(NewPoints[itpDist->ID].Ypos);    // update y position
      itp->setArea(NewPoints[itpDist->ID].area);    // update area
      NewPoints[itpDist->ID].status = "assigned";   // this point has been
  tracked(asigned to one of the previous ones)

    }else if(distPoints.size()>1){
      // sort distances in ascending order
      std::sort(distPoints.begin(), distPoints.end(), sortByDistance);
      itpDist = distPoints.begin();
      //std::cout << "min dist: " << itpDist->dist << std::endl;

      itp->setXpos(NewPoints[itpDist->ID].Xpos);        // update x
  position
      itp->setYpos(NewPoints[itpDist->ID].Ypos);        // update y
  position
      itp->setArea(NewPoints[itpDist->ID].area);        // update area
      NewPoints[itpDist->ID].status = "assigned";   // this point has been
  tracked(asigned to one of the previous ones)
      } else{
      itp->notFound();  // the tracked particle has not been found
      if( itp->getNotFound() >= 5 ) {
  itp = Particles.erase(itp);   // the particle is eliminated if it is not
  found in 2 iterations
  itp--;
      }
    }
  distPoints.clear(); // clear all the distances before moving to the next
  search
```

H   Generate New Particles

```
// now for the particles in the new frame that were not assigned
for (itpNew = NewPoints.begin(); itpNew != NewPoints.end(); itpNew++){
// if the particle is not assigned to any point and the particle is inside a
    particular
// region of the frame(the beginning), then I assume is a new particle
    coming into the frame

  if ((itpNew->status == ''not assigned'') && (itpNew->Xpos > 2040)) {
// generate new particle instances
    Particle particle;
    particle.setXpos(itpNew->Xpos);
    particle.setYpos(itpNew->Ypos);
    particle.setArea(itpNew->area);
    particle.setID(IDnumber++);
    Particles.push_back(particle); // create the new particle instance
  }
}
// eliminate all the detected new points in the new frame before going into
    the next iteration/frame
  NewPoints.clear();
```

Bibliography

[1] S. C. Hur, H. T. K. Tse, and D. D. Carlo, "Sheathless inertial cell ordering for extreme throughput flow cytometry," *Lab on a Chip*, vol. 10, no. 3, pp. 257–396, 2010.

[2] X. Xuan, J. Zhu, and C. Church, "Particle focusing in microfluidic devices," *Microfluid Nanofluid*, vol. 9, pp. 1–16, 2010.

[3] J. P.Brody and P. Yager, "Diffusion-based extraction in a microfabricated device," *Sensors and Actuators*, vol. 58, no. 1, pp. 113–18, 1997.

[4] T. Lilliehorn, U. Simu, M. Nilsson, M. Almqvist, T. Stepinski, T. Laurell, J. Nilsson, and S. Johansson, "Trapping of microparticles in the near field of an ultrasonic transducer," *Ultrasonics*, vol. 43, pp. 293–303, 2005.

[5] F. Petersson, L. Aberg, A.-M. Sward-Nilsson, and T. Laurell, "Free flow acoustophoresis: Microfluidic-based mode of particle and cell separation," *Analytical Chemistry*, vol. 79, no. 14, pp. 5117–5123, 2007.

[6] H. Li, J. R. Friend, and L. Y. Yeo, "Surface acoustic wave concentration of particle and bioparticle suspensions," *Biomedical Microdevices*, vol. 9, pp. 647–656, 2007.

[7] Z. R. Gagnon, "Cellular dielectrophoresis: Applications to the characterization, manipulation, separation and patterning of cells," *Electrophoresis*, 2011.

[8] M. Li, W. Li, J. Zhang, G. Alici, and W. Wen, "A review of microfabrication techniques and dielectrophoretic microdevices for particle manipulation and separation," *Journal of Physics D: Applied Physics*, vol. 47, no. 6, pp. 1–29, 2014.

[9] I.-F. Cheng, H.-C. Chang, D. Hou, and H.-C. Chang, "An integrated dielectrophoretic chip for continuous bioparticle filtering, focusing, sorting, trapping, and detecting," *Biomicrofluidics*, vol. 1, 2007.

[10] P. Y. Chiou, A. T.Ohta, and M. C. Wu, "Massively parallel manipulation of single cells and microparticles using optical images," *Nature*, vol. 436, no. 21, pp. 370–372, 2005.

[11] A. Jamshidi, A. T. Ohta, J. K. Valley, H.-Y. Hsu, S. L. Neale, and M. C. Wu, "Optofluidics and optoelectronic tweezers," *Invited pater at the MEMS, MOEMS, and Micromachining III*, 2008.

[12] S. Neale, C. Witte, and J. Cooper, "Portable optoelectronic tweezers (oet), taking optical micromanipulation out of the optic lab," *European Optical Society Annual Meeting*, 26-28th September 2012.

[13] J. K. Valley, S. NingPei, A. Jamshidi, H.-Y. Hsu, and M. C.Wu, "A unified platform for optoelectrowetting and optoelectronic tweezers," *Lab On a Chip*, 2011.

[14] F. Krogmann, H. Qu, W. Moench, and H. Zappe, "Light-actuated push/pull manipulation of liquid droplets," *IEEE*, 2006.

[15] A. Ashkin, "Acceleration and trapping of particles by radiation pressure," *Physics Review Letters*, vol. 24, pp. 156–159, 1970.

[16] M. Noom, B. Broek, , J. van Mameren, and G. Wuite, "Visualizing single dna-bound proteins using dna as a scanning probe," *Nature Methods*, vol. 4, pp. 1031–1036, 2007.

[17] M. P. MacDonald, G. C. Spalding, and K. Dholakia, "Microfluidic sorting in an optical lattice," *Nature*, vol. 426, pp. 421–424, 2003.

[18] A. Fu, C. Spence, A. Scherer, F. Arnold, and S. Quake, "A microfabricated fluorescence-activated cell sorter," *Nat Biotech*, vol. 17, pp. 1109–1111, 1999.

[19] A. Wolff, I. Perch-Nielsen, U. Larsen, P. Friis, G. Goranovic, C. Poulsen, J. Kutter, and P. Telleman, "Integrated advanced functionality in a microfabricated high-throughput fluorescent-activated cell sorter," *Lab on a Chip*, vol. 3, pp. 22–27, 2003.

[20] K. Smistrup, O. Hansen, H. Bruus, and M. Hansen, "Magnetic separation in microfluidic systems using microfabricated electromagnets-experiments and simulations," *Journal of Magnetism and Magnetic Materials*, vol. 293, pp. 597–604, 2005.

[21] D. Inglis, R. Riehn, R. Austin, and J. Sturm, "Continuous microfluidic immunomagnetic cell separation," *Applied Physics Letters*, vol. 85, pp. 5093–5095, 2004.

[22] R. Pethig, "Review article-dielectrophoresis: Status of the theory, technology, and applications," *American Institute of Physics*, vol. 4, no. 5, pp. 1–35, 2010.

[23] G. Batchelor, *An Introduction to Fluid Dynamics*. Cambridge: Cambridge University Press, 1 ed., 1999.

[24] A. A. Kayani, K. Khoshmanesh, S. A. Ward, A. Mitchell, and K. Kalantar-zadeh, "Optofluidics incorporating actively controlled micro- and nano-particles," *BIOMI-CROFLUIDICS*, 2012.

[25] K. Khoshmanesh, C. Zhang, F. J. Tovar-Lopez, S. Nahavandi, S. Baratchi, K. Kalantar-zadeh, and A. Mitchell, "Dielectrophoretic manipulation and separation of microparticles using curved microelectrodes," *Electrophoresis*, vol. 30, pp. 3707–3717, 2009.

[26] L. R. Huang, E. C. Cox, R. H. Austin, and J. C. Sturm, "Continuous particle separation through deterministic lateral displacement," *Science*, vol. 304, pp. 987–990, 2004.

[27] K. SS, B. AA, K. G, and P. I, "Inertial microfluidics for continuous particle separation in spiral microchannels," *Lab on a Chip*, vol. 9, pp. 2973–2980, 2009.

[28] J. Zhang, S. Yang, D. Yan, G. Alici, and N.-T. Nguyen, "Fundamentals and applications of inertial microfluidics: A review," *Lab on a Chip: miniaturisation for chemistry, biology, materials science and bioengineering*, vol. 16, pp. 10–34, 2016.

[29] A. A. S. Bhagat, H. Bow, H. Hou, S. Tan, J. Han, and C. Lim, "Microfluidics for cell separation," *Med. Biol. Eng. Comput*, 2010.

[30] F. Petersson, L. Aberg, A.-M. Sward-Nilsson, and T. Laurell, "Free flow acoustophoresis: Microfluidic-based mode of particle and cell separation," *American Chemical Society*, vol. 79, no. 14, pp. 5117–5123, 2007.

[31] J. T. B., "Electromechanics of particles," *Cambridge University Press*, 1995.

[32] B. Cetin and D. Li, "Review: Dielectrophoresis in microfluidics technology," *Electrophoresis*, 2011.

[33] C. Kremer, C. Witte, S. L. Neale, J. Reboud, M. P. Barrett, and J. M. Cooper, "Shape-dependent optoelectronic cell lysis," *Angewandte Communications*, 2014.

[34] P. R.C and J. V. Vykoukal, "Dielectrophoresis-based sample handling in general-purpose programmable diagnostic instruments," *Proceedings of the IEEE*, vol. 92, no. 1, pp. 22–42, 2004.

[35] M. C. Wu, "Optoelectronic tweezers," *Nature Photonics*, 2011.

[36] R. Martinez-Duarte, "Microfabrication technologies in dielectrophoresis applications - a review," *Electrophoresis*, 2012.

[37] J. R. Moffitt, Y. R. Chemla, S. B. Smith, and C. Bustamante, "Recent advances in optical tweezers," *Annual Reviews Biochemistry*, vol. 77, pp. 205–228, 2008.

[38] L. WM, R. PJ, M. RF, M. NK, and D. K, "Construction and calibration of an optical trap on a fluorescence optical microscope," *Nature Protocols*, vol. 2, pp. 3226–3238, 2007.

[39] K. C. Neuman and A. Nagy, "Single-molecule force spectroscopy: optical tweezers, magnetic tweezers and atomic force microscopy," *Nature Methods*, vol. 5, pp. 491–505, 2008.

[40] C.-P. Jen and H.-H. Chang, "A handheld preconcentrator for the rapid collection of cancerous cells using dielectrophoresis generated by circular microelectrodes in stepping electric fields," *Biomicrofluidics*, vol. 5, no. 3, pp. 34101–3410110, 2011.

[41] E. T. Lagally, S.-H. Lee, and H. T. Soh, "Integrated microsystem for dielectrophoretic cell concentration and genetic detection," *Lab on a Chip*, vol. 5, pp. 1053–1058, 2005.

[42] G.-H. Chen, C.-T. Huang, H.-H. Wu, T. N.Zamay, A. S.Zamay, and C.-P. Jen, "Isolating and concentrating rare cancerous cells in large sample volumes of blood by using dielectrophoresis and stepping electric fields," *BioChip Journal*, vol. 8, no. 2, pp. 67–72, 2014.

[43] H.-H. Cui, J. Voldman, X.-F. He, and K.-M. Lim, "Separation of particles by pulsed dielectrophoresis," *The Royal Society of Chemistry*, vol. 9, no. 9, pp. 2306–2312, 2009.

[44] P. R. Gascoyne, J. Vykoukal, R. Weinstein, A. Gandini, D. Parks, and R. Sawh, "Magnetophoretic-dielectrophoretic fiel-flow fractionation," *Proc. Micro Total Analysis Systems*, pp. 323–325, 2002.

[45] T. Braschler and N. Demierre, "Continuous separation of cells by balanced dielectrophoretic forces at multiple frequencies," *The Royal Society of Chemistry*, vol. 8, no. 8, pp. 280–286, 2008.

[46] H. Morgan and N. G. Green, *AC Electrokinetic: Colloids and Nanoparticles*. London: Research Studies Press, 1 ed., 2003.

[47] P. Gasgoyne, C. Mahidol, M. Ruchirawat, J. Satayavivad, P. Watcharasit, and F. F. Becker, "Microsample preparation by dielectrophoresis: isolation of malaria," *The Royal Society of Chemistry*, vol. 2, no. 2, pp. 70–75, 2002.

[48] A. Menachery, C. Kremer, P. E. Wong, A. Carlsson, S. L.Neale, M. P.Barret, and J. M. Cooper, "Counterflow dielectrophoresis for trypanosome enrichment and detection in blood," *Scientific Reports*, vol. 2, no. 775, 2012.

[49] A. El-Baz, G. M. Beache, G. Gimelfarb, K. Suzuki, K. Okada, A. Elnakib, A. Soliman, and B. Abdollahi, "Computer-aided diagnosis systems for lung cancer: Challenges and methodologies," *International Journal of Biomedical Imaging*, vol. 2013, p. 43, 2013.

[50] B. T. Constantino, "The red cell histogram and the dimorphic red cell population," *Laboratory Medicine*, vol. 42, no. 5, p. 300, 2011.

[51] S. Chandrasiri and P. Samarasinghe, "Automatic anemia identification through morphological image processing," *Information and Automation for Sustainability, 2014 7th International Conference*, 2014.

[52] Y. Faziloglu, R. J. Stanley, R. H. Moss, W. V. Stoecker, and R. P. McLean, "Colour histogram analysis for melanoma discrimination in clinical images," *Skin Research and Technology*, 2003.

[53] S. Bieler, E. Matovu, P. Mitashi, E. Ssewannyana, S. Shamamba, P. R. Bessell, and J. Mathu, "Improved detection of trypanosoma brucei by lysis of red blood cells, concentration and led fluorescence microscopy," *Acta Tropica*, vol. 121, no. 2, pp. 135–140, 2012.

[54] F. Chappuis, L. Loutan, P. Simarro, V. Lejon, and P. Buscher, "Options for field diagnosis of human african trypanosomiasis," *Clinical Microbiology Reviews*, vol. 18, pp. 133–146, 2005.

[55] V. Piuri and F. Scotti, "Morphological classification of blood leucocytes by microscope images," *IEEE International Conference on Computational Intelligence for Measurement Systems and Applications*, 2004.

[56] M. Maitra, R. K. Gupta, and M. Mukherjee, "Detection and counting of red blood cells in blood cell images using hough transform," *International Journal of Computer Applications*, vol. 53, no. 16, pp. 18–22, 2012.

[57] M. Hayashi, A. Hattori, H. Kim, H. Terazono, T. Kaneko, and K. Yasuda, "Fully automated on-chip imaging flow cytometry system with disposable contamination-free plastic re-cultivation chip," *International Journal of Molecular Sciences*, vol. 12, no. 6, pp. 3618–3634, 2011.

[58] Intel, "Opencv (open source computer vision)."

[59] N. Christianini and J. Shawe-Taylor, *An Introduction to Support Vector Machines and other kernel-based learning methods.* Cambridge University Press, 2000.

[60] C.Stauffer and W.Grimson, "Adaptive background mixture models for real-time tracking," *Proceedings of the IEEE*, vol. 92, pp. 246–252, 1999.

[61] L. Najman and H. Talbot, *Mathematical Morphology: From Theory to Applications.* Hoboken, NJ, USA: John Wiley and Sons, Inc, 2013.

[62] K. Dawson-Howe, *A practical introduction to computer vision with opencv.* Trinity College Dublin, Ireland: Wiley, 2014.

[63] N. SL, M. M, W. JI, D. K, and K. TF, "The resolution of optical traps created by light induced dielectrophoresis (lidep).," *Optics Express*, 2007.

[64] G. Milne, *Thesis for the degree of Doctor of Philosopy: Optical Sorting and Manipulation of Microscopic Particles.* University of St Andrews, St Andrews, Fife, Scotland.: Optical Trapping Group, 2007.

[65] C. Stauffer and W. Grimson, "Adaptive background mixture models for real-time tracking," *Computer Vision and Pattern Recognition; IEEE, Computer Society Conference*, 1999.

[66] R. J. Radke, S. Andra, O. Al-Kofahi, and B. Roysam, "Image change detection algorithms: A systematic survey," *IEEE Transactions on Image Processing*, vol. 14, 2005.

[67] J. Flusser, B. Zitova, and T. Suk, *Moments and Moment Invariants in Patter Recognition.* Wiley, 2009.

[68] M. Hu, "Visual pattern recognition by moment invariants," *IRE Transactions*, 1962.

[69] C. Cortes and V. Vapnik, "Support-vector networks," *Machine Learning*, vol. 20, pp. 273–297, 1995.

[70] V. V. and L. A., "A pattern recognition using generalized portrait," *Automation and Remote Control*, vol. 24, pp. 774–780, 1963.

[71] B. Boser, I. Guyon, and V. Vapnik, "A training algorithm for optimal margin classifiers," *Proceedings of the fifth annual workshop on Computational learning theory - COLT 1992*, p. 144, 1992.

[72] R. Resnick, D. Halliday, and K. S. Krane, *Physics.* Chichester: John Wiley and Sons, 4 ed., 2002.

[73] Y. Huang, X.-B. Wang, F. F. Becker, and P. Gascoyne, "Introducing dielectrophoresis as a new force field for field-flow fractionation," *Biophysical Journal*, vol. 73, no. 73, pp. 1118–1129, 1997.

[74] K.-H. Han and A. B. Frazier, "Lateral-driven continuous dielectrophoretic microseparators for blood cells suspended in a highly conductive medium," *The Royal Society of Chemistry*, vol. 8, no. 8, pp. 1079–1086, 2008.

[75] C. Witte, R. Wilson, J. M. Cooper, and S. L. Neale, "Oet meets acoustic tweezing," *Proc. SPIE 8458, Optical Trapping and Optical Micromanipulation*, vol. 845821, 2012.

[76] P. Scherz and S. Monk, *Practical Electronics for Inventors. - Third edition.* McGraw-Hill, 2013.

[77] Arduino, "Arduino (open source hardware and software)."

[78] J. R. Luna, J. Cooper, and S. Neale, "Automated particle identification through regression analysis of size, shape and colour," *SPIE Proceedings*, vol. 9711, 2016.